Developments and Advances in Nonlinear Terahertz Spectroscopy

by

Nathaniel Curran Brandt

B.S. Chemistry, B.A. Mathematics, University of Saint Thomas (2008)

Submitted to the Department of Chemistry
in Partial Fulfillment of the Requirements of the Degree of

Doctor of Philosophy

at the

MASSACHUSETTS INSTITUTE OF TECHNOLOGY

June 2014

Signature redacted

Signature of Author.....
Department of Chemistry
May 16, 2014

Signature redacted

Certified by.....
Keith A. Nelson
Professor of Chemistry
Thesis Supervisor

Signature redacted

Accepted by.....
Robert W. Field
Chairman, Department Committee on Graduate Students

This doctoral thesis has been examined by a committee of the Department of Chemistry as follows:

Signature redacted

Professor Robert W. Field.....
Chairperson

Signature redacted

Professor Keith A. Nelson.....
Thesis Supervisor

Signature redacted

Professor Adam P. Willard.....

Advances and Developments in Nonlinear Terahertz Spectroscopy

by

Nathaniel Curran Brandt

Submitted to the Department of Chemistry
on May 16, 2014, in partial fulfillment of the
requirements for the degree of
Doctor of Philosophy

Abstract

Nonlinear terahertz (THz) spectroscopy is a rapidly developing field, which is concerned with driving and observing nonlinear material responses in the THz range of the electromagnetic spectrum. In this thesis, I present several advances in nonlinear THz spectroscopy that expand the range of systems in which responses may be driven, the types of responses that may be initiated, and the way in which these responses may be observed.

Sufficiently strong THz pulses are generated using the tilted-pulse-front technique, and are collected, focused, and detected using a THz spectrometer specifically designed for maximum peak THz electric field strength and maximum flexibility, allowing for a wide range of experimental geometries to be implemented. Further enhancement in the peak THz electric field strength is obtained through the use of metamaterial structures, which concentrate free-space THz fields in their antenna gaps.

Impact ionization was observed in high-resistivity silicon, a material in which no nonlinear THz response had been previously seen, using metamaterial structures to enhance free space THz electric fields. Using three-dimensional metamaterial structures, the THz magnetic field is shown to also be capable of driving ionization processes both in high-resistivity silicon as well as air. Using metamaterial structures with open gaps, the THz electric field is shown to induce breakdown in air at both high and low pressures due to field ionization processes involving the gold metamaterial antennas. Furthermore, THz-driven electromigration of the gold metamaterial antennas is observed. Probing of THz-driven structural changes in both vanadium dioxide and perovskite ferroelectrics is demonstrated using femtosecond X-ray pulses from the LCLS facility at the SLAC National Accelerator Laboratory. Finally, ongoing results involving energetic materials, stimulated Raman measurements, and Stark effect measurements are discussed. This work, coupled with the ongoing expansion of nonlinear THz techniques and potential applications demonstrates the continued development of nonlinear THz spectroscopy into a robust and valuable method for investigating fundamental processes in a multitude of systems.

Thesis supervisor: Keith A. Nelson

Title: Professor of Chemistry

Acknowledgements

This thesis was made possible through the support and inspiration of many, many people, to whom I owe a great deal of thanks.

Even though I was fascinated by the periodic table when I was a child, I didn't always want to study chemistry. However, I was talked into registering for AP Chemistry as a senior in high school by Ms. Natalie Rasmussen, and I soon realized how much I enjoyed the subject, even though I swore up and down I still wanted to be an engineer. Thanks to the intercession of Dr. David Boyd at the University of Saint Thomas, I made the switch to chemistry for good, and I am thankful for his persuasion and support.

I was fortunate enough to perform research in the lab of Dr. Joe Brom at the University of Saint Thomas for three years. His patient guidance and methodical, rigorous, yet practical approach to problem solving taught me many lessons that would be of great use in my work at MIT. It was my experiences in his lab that led to my desire to attain a PhD in physical chemistry.

My ability to attend the University of Saint Thomas in the first place was made possible through the generosity of Ryan Companies through the Ryan Construction Company Scholarship. Their financial support of my undergraduate education allowed me the freedom to pursue my undergraduate research work and my goal of post-graduate studies in chemistry.

My time at MIT has been greatly enhanced though the help and support of many people. I have been truly fortunate to have had Prof. Keith Nelson as an advisor for six years. His relentless energy, enthusiasm and optimism, even in the face of seemingly impossible deadlines and long experimental odds, have been inspiring throughout my time in his group. Keith's guidance and support of my work and my ideas, no matter how far-fetched, has been unwavering, and for that I am truly grateful.

I have had the extremely good fortune to spend the entirety of my time in the Nelson group working closely with Dr. Harold Hwang. Harold is a truly talented teacher, and his prowess at both running experiments and understanding scientific concepts has been a constant source of inspiration and motivation to me. His contribution to my development as a scientist cannot be understated, and neither can the value of his friendship. Our six years of performing nonlinear THz measurements together have resulted in many experiences which I will not soon forget, including spending late nights fighting with liquid helium equipment, exploring the streets of Kyoto at the crack of dawn, sleeping in a car in the parking lot of the LCLS, frantically trying to purchase a space heater at Target in the middle of the night, repeatedly driving into the Palo Alto Transit Center by mistake, and lighting a campfire with cask strength bourbon and a plastic bag. While I look forward to my future as a postdoctoral associate at the University of Minnesota, I will truly miss working with Harold.

I was lucky enough to have joined "Team THz", as we like to call ourselves, when it consisted of Harold, Dr. Ka-Lo Yeh, and Dr. Matthias Hoffmann, and nonlinear THz measurements were just starting to work properly. This gave me the opportunity to learn the experimental basics of nonlinear THz spectroscopy

from the very people who had helped develop it into a field in the first place. Matthias was instrumental in teaching me the basics of THz spectroscopy during my first year, and his expertise and undying pursuit of experimental excellence made a strong impression on me. I count myself lucky to have learned from him, and I have enjoyed getting to work with him further at the LCLS in later years.

During my time in the Nelson group, Team THz has also included Dr. Brad Perkins, Dr. Sharly Fleischer, Dr. Xibin Zhou, Zhao Chen, Jian Lu, Yaqing Zhang, Leora Cooper, Xian Li, and Dr. Brandt Pein, in addition to our waveguided counterparts, Dr. Kit Werley, Dr. Steph Teo, Ben Ofori-Okai, and Prasahnt Sivarajah, and I am glad to have worked with each of them. I have had the good fortune to work closely with Ben and Steph in particular, and I am very grateful for their continual help, support, friendship, and encouragement. I won't soon forget late-night liquid helium plumbing with Ben while wearing suits, and I have been glad to have Steph as my companion in thesis-writing purgatory. I am thankful for Brad's guidance, especially in all things electrical and mechanical, and our hastily-arranged last-minute trip to the Advanced Photon Source was quite the learning experience. I am glad to have learned from Sharly's experimental prowess and no-nonsense approach to even the most complicated experiments, and he always provided a sounding board for ideas and scientific discussion, as did Xibin and Zhao. Kit's passion for total excellence in all things optical provided a source of many late-night discussions, and many improvements to my experimental designs. I have worked closely with Jian during the last few years as he prepares to take over the lab, and I am confident that his prodigious experimental skill and liberal use of lucky cat statues will take nonlinear THz spectroscopy to new heights. Prasahnt, Leora, Yaqing, Xian, and Brandt are newer additions, and I am excited to see where they take the project in the future. I am especially thankful for Prasahnt's help with SEM imaging and Leora's assistance growing RDX crystals.

The Nelson group as a whole has proven to be a supportive and pleasant place to work, and I thank my colleagues for making life enjoyable both inside and outside of lab. In particular, Kara Manke has proven to be a good friend and a source of advice and guidance. I am also thankful for the assistance and guidance of many others, including Dylan Arias, Patrick Wen, Johanna Wolfson, Jeremy Johnson, David Veysset, Felix Hofmann, Alex Maznev, Jeff Eliason, Colby Steiner, Yongbao Sun, and Sam Teitelbaum.

Our collaborators at the Boston University Photonics Center in the research groups of Richard Averitt and Xin Zhang are indispensable to the majority of the research presented here through their efforts in designing and fabricating THz metamaterial samples. In particular, Dr. Kebin Fan has been the source of many fantastic sets samples and the necessary simulations to understand their behavior. For his help and support I am very thankful. I have also had the good fortune to work with Dr. Mengkun Liu, Elsa Abreu, and Aaron Sternbach on the vanadium dioxide measurements at the LCLS.

I am extremely grateful to our collaborators at the LCLS, Stanford University, and Argonne National Lab, in particular Prof. Aaron Lindenberg, Dan Daranciang, Dr. Haidan Wen, Dr. Matt Highland, Frank Chen, Dr. Alex Gray, Dr. Diling Zhu, and Dr. Mike Glownia, for leading and supporting the four LCLS beamtimes in which I have been privileged enough to take part. My time at the LCLS has been an incredible experience, and I thank them and the rest of our teams (see Chapter 6) for making it possible.

Many other people at MIT have contributed directly or indirectly to the success of the research presented in the preceding pages. In particular, Marc Belanger at the Edgerton Machine Shop, Tim McClure at the CMSE, and Li Li at the DCIF have been extremely helpful, as have the wonderful staff of the Chemistry Education Office. Fr. Richard Clancy and Tech Catholic Community have also been a source of guidance and support during my time here.

My good friends and long-time roommates Andrew Horning and Shane Yost have been constants in my life during my graduate work. Throughout our time as PhD students, we've experienced ups and downs together, jumped out of planes together, vented at one another about whatever was currently broken in lab, and worn a lot of argyle, among many other shared experiences. I greatly value their support and encouragement both inside and outside of lab.

My parents, Mark and Jennie, have been approving of my desire to be a scientist since I was young, even when I burned their sidewalk, filled their basement with HCl, and set my pants on fire. For their love, support, and encouragement throughout my life, along with that of my sister Hannah, I am very thankful.

Finally, I owe a special thanks to my wonderful fiancée, Lanita Gaworski. My favorite memories of graduate school are the times I've spent with you, including exploring Boston by foot, bicycle, and train, visiting Acadia, Providence, and Manchester-by-the-Sea, grilling in my asphalt backyard, and adopting our cat in the middle of nowhere in the midst of a rainstorm, amongst many others. Your love and support during graduate school has made all the difference, and you've always been there for me when I've needed it the most. We may have spent most of my graduate career 1,124 air miles apart, but I've always known that you were right beside me the whole time. I look forward to spending the rest of my life with you.

In primis Deo gratias.

Nathaniel Brandt

May 29th, 2014

For Lanita

Contents

Chapter 1

Introduction

The infrared region of the electromagnetic spectrum, which extends from frequencies just below those of visible light to roughly 10^{13} Hz, has been studied ever since its existence was discovered in 1800 by William Herschel[1]. Likewise, the radio and microwave regions of the electromagnetic spectrum, which extend from single Hz frequencies to approximately 10^{11} Hz, have been well-explored beginning with their demonstration in 1887 by Heinrich Hertz[2]. Until recently, however, the frequency range between these two regimes, from approximately 10^{11} to 10^{13} Hz, has been relatively unexplored. This range is referred to as the terahertz (THz) region of the electromagnetic spectrum, after its central frequency of 10^{12} Hz, or 1 THz, and has been referred to as the "THz gap" due to its unexplored nature.

The reason for the lack of investigation into the THz region is easily understood by considering the methods used to generate electromagnetic radiation in each region bordering it. The infrared region may be accessed using optical methods; however, such methods are typically incapable of generating sufficiently low frequencies to access the THz range. Conversely, the microwave region of the spectrum is accessed by electronic means, but state-of-the-art electronics are still not sufficiently fast to reach into the THz range. As a result, the THz region is difficult to access.

The beginnings of filling the THz gap appeared in the 1970's, and involved two separate ultrafast laser-driven phenomena, both of which were to varying degrees investigated by David Auston. First, it was observed that THz-frequency pulses could be generated and detected through optical rectification

processes[3–5] that are discussed in detail in subsequent chapters of this thesis. Secondly, Auston demonstrated the use of photoconductive switches as both sources and detectors of THz radiation[6–9]. In these devices, an ultrafast optical pulse irradiates a biased semiconductor and the resulting sudden acceleration of newly created free carriers produces a burst of current that radiates in the THz frequency range; or conversely, an optical pulse irradiates an unbiased semiconductor and an incident THz field provides a transient bias that accelerates the carriers, producing current that is measured electrically to reveal the field polarity and strength. Through the mid-1980's, many of the techniques that would form the backbone of modern THz science were developed, including (as discussed in further chapters) electro-optic sampling[10], the observation of THz Cherenkov radiation in $LiTaO_3$[11,12], THz spectroscopy of lattice vibrations in $LiTaO_3$[13,14], time-domain THz spectroscopy[15], and even optical-pump/THz-probe spectroscopy of carriers in GaAs[16].

In 1988, it was demonstrated that THz generation and detection by photoconductive switches could be done in free space[17], with similar demonstrations of free-space THz radiation from optical rectification sources following[18,19], culminating with the first demonstration of the now-ubiquitous source of free-space THz from optical rectification in ZnTe in 1994[20]. Free-space THz detection based upon electro-optic sampling was also developed around the same time[21,22]. At this point, all of the necessary components were in place to develop modern free-space THz spectroscopy, which has proved useful for observing spectral features in a multitude of systems, ranging from explosives to biological systems to semiconductors.

High-powered THz sources, however, have lagged significantly behind their lower-powered counterparts. Such sources are desirable for the investigation of a broad range of high-field ultrafast material responses, including carrier transport in semiconductors, domain switching in ferroelectric materials, and coupled interactions in molecular crystals. Until very recently, the only high-powered sources of THz radiation included gas lasers[23] and free electron laser-based systems[24], both of which are

poorly suited for laboratory-based nonlinear THz spectroscopy as a result of their narrow bandwidths and long pulse durations (and impracticality, in the case of the latter type of source). The advent of tilted-pulse-front THz generation in $LiNbO_3$, however, has allowed for tabletop, broadband, high-power ultrafast sources of THz radiation in the ~ 0.2-2 THz range which are suitable for generating very strong transient electric fields and driving nonlinear material interactions[25–27]. This has given rise to the field of nonlinear THz spectroscopy, which has been demonstrated in a variety of systems, including semiconductors[28–30], liquids[31], molecular crystals[32], quantum paraelectric crystals[33], graphene[34], superconductors[35,36], and gases[37,38]. Further advances into nonlinear THz spectroscopy have been made possible through the use of metamaterial structures as enhancing structures for free-space THz fields[39,40]. In parallel developments, high fields extending to 10 THz and well into the IR spectral range have been generated using other nonlinear crystalline materials as well using ionized gas-phase plasmas [refs]. As a result, nonlinear spectroscopy spanning the THz range is now possible on tabletop systems.

This thesis presents recent advances in nonlinear THz spectroscopy, beginning with a thorough background of the techniques necessary to generate, detect, and analyze high-power THz pulses, including a discussion of the use of metamaterial enhancement structures. Nonlinear THz spectrometer design is also covered. Following this, several recent measurements are presented, including metamaterial-enhanced nonlinear THz responses in high-resistivity silicon, metamaterial-coupled THz-driven breakdown phenomena, and femtosecond X-ray probing of THz-driven structural responses. Finally, ongoing results and experimental developments concerning THz-driven responses in energetic materials and quantum dots are presented. The measurements presented here show that nonlinear THz spectroscopy is rapidly developing into a broadly applicable technique with a wide variety of implementations for study of many material classes and phenomena.

References

1. Herschel, W. Experiments on the refrangibility of the invisible rays of the sun. **90,** 284 (1800).

2. Hertz, H. Ueber die einwirkung einer geradlinigen electrische schwingung auf eine benachbarte strombahn. *Ann. Phys.* **270,** 155 (1888).

3. Auston, D. H., Glass, A. M. & Ballman, A. A. Optical rectification by impurities in polar crystals. *Phys. Rev. Lett.* **28,** 897 (1971).

4. Auston, D. H. & Glass, A. M. Optical generation of intense picosecond electrical pulses. *Appl. Phys. Lett.* **20,** 398 (1972).

5. Shen, Y. R. Far-infrared generation by optical mixing. *Prog. Quantum. Elec.* **4,** 207 (1976).

6. Auston, D. H. Picosecond optoelectronic switching and gating in silicon. *Appl. Phys. Lett.* **26,** 101 (1975).

7. Auston, D. H., Johnson, A. M., Smith, P. R. & Bean, J. C. Picosecond optoelectronic detection, sampling, and correlation measurements in amorphous semiconductors. *Appl. Phys. Lett.* **37,** 371 (1980).

8. Smith, P. R., Auston, D. H., Johnson, A. M. & Augustyniak, W. M. Picosecond photoconductivity in radiation-damaged silicon-on-sapphire films. *Appl. Phys. Lett.* **38,** 47 (1981).

9. Auston, D. H. Subpicosecond electro-optic shock waves. *Appl. Phys. Lett.* **43,** 713 (1983).

10. Valdmanis, J. A., Morou, G. & Gabel, C. W. Picosecond electro-optic sampling system. *Appl. Phys. Lett.* **41,** 211 (1982).

11. Auston, D. H., Cheung, K. P., Valdmanis, J. A. & Klienman, D. A. Cherenkov radiation from femtosecond optical pulses in electro-optic media. *Phys. Rev. Lett.* **53,** 1555 (1984).

12. Kleinman, D. A. & Auston, D. H. Theory of electrooptic shock radiation in nonlinear optical media. *IEEE J. Quantum Electron.* **20,** 964 (1984).

13. Cheung, K. P. & Auston, D. H. A novel technique for measuring far-infrared absorption and dispersion. *Infrared Phys.* **26,** 23 (1986).

14. Cheung, K. P. & Auston, D. H. Excitation of coherent phonon polaritons with femtosecond optical pulses. *Phys. Rev. Lett.* **55,** 2152 (1985).

15. Auston, D. H. & Cheung, K. P. Coherent time-domain far-infrared spectroscopy. *J. Opt. Soc. Am. B* **2,** 606 (1985).

16. Nuss, M. C., Auston, D. H. & Capasso, F. Direct subpicosecond measurment of carrier mobility of photoexcited electrons in gallium arsenide. *Phys. Rev. Lett.* **58,** 2355 (1987).

17. Smith, P. R., Auston, D. H. & Nuss, M. C. Subpicosecond photoconducting dipole antennas. *IEEE J. Quantum Electron.* **24,** 255 (1988).

18. Hu, B. B., Zhang, X.-C., Auston, D. H. & Smith, P. R. Free-space radiation from electro-optic crystals. *Appl. Phys. Lett.* **56,** 506 (1990).

19. Xu, L., Zhang, X.-C. & Auston, D. H. Terahertz beam generation by femtosecond optical pulses in electro-optic materials. *Appl. Phys. Lett.* **61,** 1784 (1992).

20. Rice, A. *et al.* Terahertz optical rectification from <110> zinc-blende crystals. *Appl. Phys. Lett.* **64,** 1324 (1994).

21. Wu, Q. & Zhang, X.-C. Free-space electro-optic sampling of terahertz beams. *Appl. Phys. Lett.* **67,** 3523 (1995).

22. Jepsen, P. *et al.* Detection of THz pulses by phase retardation in lithium tantalate. *Phys. Rev. E. Stat. Phys. Plasmas. Fluids. Relat. Interdiscip. Topics* **53,** R3052 (1996).

23. *Nonlinear infrared generation*. (Springer-Verlag Berlin Heidelberg, 1977).

24. Williams, G. P. Filling the THz gap—high power sources and applications. *Reports Prog. Phys.* **69,** 301 (2006).

25. Hebling, J., Almasi, G., Kozma, I. & Kuhl, J. Velocity matching by pulse front tilting for large area THz-pulse generation. *Opt. Express* **10,** 1161 (2002).

26. Yeh, K.-L., Hoffmann, M. C., Hebling, J. & Nelson, K. A. Generation of 10 μJ ultrashort terahertz pulses by optical rectification. *Appl. Phys. Lett.* **90,** 171121 (2007).

27. Yeh, K.-L., Hebling, J., Hoffmann, M. C. & Nelson, K. A. Generation of high average power 1 kHz shaped THz pulses via optical rectification. *Opt. Commun.* **281,** 3567 (2008).

28. Hoffmann, M. C., Hebling, J., Hwang, H. Y., Yeh, K. & Nelson, K. A. THz-pump/THz-probe spectroscopy of semiconductors at high field strengths [Invited]. *J. Opt. Soc. Am. B* **26,** A29 (2009).

29. Hoffmann, M., Hebling, J., Hwang, H., Yeh, K.-L. & Nelson, K. Impact ionization in InSb probed by terahertz pump—terahertz probe spectroscopy. *Phys. Rev. B* **79,** 161201 (2009).

30. Hebling, J., Hoffmann, M. C., Hwang, H. Y., Yeh, K.-L. & Nelson, K. A. Observation of nonequilibrium carrier distribution in Ge, Si, and GaAs by terahertz pump–terahertz probe measurements. *Phys. Rev. B* **81,** 035201 (2010).

31. Hoffmann, M. C., Brandt, N. C., Hwang, H. Y., Yeh, K.-L. & Nelson, K. A. Terahertz Kerr effect. *Appl. Phys. Lett.* **95,** 231105 (2009).

32. Jewariya, M., Nagai, M. & Tanaka, K. Ladder climbing on the anharmonic intermolecular potential in an amino acid microcrystal via an intense monocycle terahertz pulse. *Phys. Rev. Lett.* **105,** 203003 (2010).

33. Katayama, I. *et al.* Ferroelectric soft mode in a $SrTiO_3$ thin film impulsively driven to the anharmonic regime using intense picosecond terahertz pulses. *Phys. Rev. Lett.* **108,** 097401 (2012).

34. Hwang, H. Y. *et al.* Nonlinear THz conductivity dynamics in P-type CVD-grown graphene. *J. Phys. Chem. B* **117,** 15819 (2013).

35. Matsunaga, R. & Shimano, R. Nonequilibrium BCS state dynamics induced by intense terahertz pulses in a superconducting NbN film. *Phys. Rev. Lett.* **109,** 187002 (2012).

36. Grady, N. K. *et al.* Nonlinear high-temperature superconducting terahertz metamaterials. *New J. Phys.* **15,** 105016 (2013).

37. Fleischer, S., Zhou, Y., Field, R. W. & Nelson, K. A. Molecular orientation and alignment by intense single-cycle THz pulses. *Phys. Rev. Lett.* **107,** 163603 (2011).

38. Fleischer, S., Field, R. W. & Nelson, K. A. Commensurate two-quantum coherences induced by time-delayed THz fields. *Phys. Rev. Lett.* **109,** 123603 (2012).

39. Liu, M. *et al.* Terahertz-field-induced insulator-to-metal transition in vanadium dioxide metamaterial. *Nature* **487,** 345 (2012).

40. Fan, K. *et al.* Nonlinear terahertz metamaterials via field-enhanced carrier dynamics in GaAs. *Phys. Rev. Lett.* **110,** 217404 (2013).

Chapter 2

Generation, Enhancement, Detection, and Analysis of High-Field Terahertz Pulses

Moving beyond low-power THz sources to sources capable of driving nonlinear responses requires moving to THz generation techniques that contain significant advances when compared to their commonly used low-power counterparts. This chapter describes in detail the tilted-pulse-front optical rectification technique, which is capable of generating THz pulses with microjoule energies and was used for all work presented in this thesis. In many materials, however, the free-space THz electric fields that result from tightly focusing the high-energy THz pulses generated by the tilted-pulse-front technique are still insufficient to drive nonlinear responses. In this case, field enhancement is obtained through the use of metamaterial split ring resonator (SRR) structures. Detection of free-space THz pulses through electro-optic sampling is also presented, as well as an overview of the techniques necessary for analysis of the raw data generated from a typical free-space THz spectrometer.

2.1

Tilted-Pulse-Front THz Generation

2.1.1

Optical Rectification for Low-Power THz Generation

Generation of free-space ultrafast THz pulses typically relies upon the interaction of an ultrafast optical pulse with a nonlinear material, in which the electric field E of the optical pulse generates a nonlinear polarization P, given by

$$P = \varepsilon_0\left(\chi^{(1)}E + \chi^{(2)}E^2 + \chi^{(3)}E^3 + \cdots\right) \tag{2.1}$$

where ε_0 is the vacuum permittivity and the term $\chi^{(x)}$ represents the xth order susceptibility[1]. Most THz sources rely specifically upon the process of optical rectification for THz pulse generation. Physically, optical rectification may be thought of as a special case of difference frequency generation (DFG), in which an optical pulse at a frequency ω undergoes DFG with itself, generating a DC current at zero frequency, i.e. the AC electric field at ω is rectified. For an ultrafast pulse with a finite bandwidth $\Delta\omega$, this frequency will not be zero and instead a range of frequencies $\Delta\Omega$ up to approximately $\Delta\omega$ may be generated. For typical commercial femtosecond laser systems, the bandwidth $\Delta\omega$, and hence the frequency span of the generated electric field $\Delta\Omega$, are on the order of 10 THz.

Optical rectification is described in general terms mathematically as a second-order process with a nonlinear polarization $P^{(2)}$ given by

$$P^{(2)} = 2\varepsilon_0\chi^{(2)}(E_1E_1^* + E_2E_2^*) \tag{2.2}$$

where E_1 and E_2 represent the electric field components of incident optical pulses and the second-order nonlinear susceptibility is given by $\chi^{(2)}$, which is a material-specific parameter[1]. Note that for a single ultrafast optical pulse, Eq. 2.2 implies that the nonlinear polarization, and hence the generated THz radiation, will be linearly proportional to the intensity of the ultrafast optical pulse.

For an arbitrary polarization direction k, the nonlinear susceptibility may be related to the material-specific electro-optic tensor through

$$P_k^{(2)} = -\left(\frac{\varepsilon_0}{16\pi}\right) n_0^4 \sum_{ij} r_{(ij)k} E_i E_j^* \tag{2.3}$$

where $r_{(ij)k}$ represent elements of the electro-optic tensor **r** and n_0 is the (assumed isotropic) optical index[2]. Taken together, Eq. 2.2 and 2.3 show that the THz field generated by optical rectification is expected to depend linearly on the intensity of the optical pulse undergoing optical rectification as well as the relevant electro-optic tensor component of the nonlinear crystal used for the optical rectification medium.

Note that the above analysis of optical rectification ignores the effects of dispersion in the nonlinear crystal, both at THz and optical frequencies. When dispersion is present, the optical pulse and the THz field that it generates may not propagate at the same velocity, and are said to be no longer phase-matched. In this scenario, the efficiency of THz generation will be greatly diminished. This reality is quantified by the coherence length l_c of the optical rectification process, i.e. the length of propagation in the nonlinear crystal over which phase-matched optical rectification can be expected, given by

$$l_c = \frac{\pi c}{\omega_{THz}\left|n_{opt} - \lambda_{opt}\left(\frac{dn_{opt}}{d\lambda}\right)_{\lambda_{opt}} - n_{THz}\right|} \tag{2.4}$$

where ω_{THz} is the THz frequency, n_{opt} and n_{THz} are the indices at optical and THz frequencies, respectively, and λ_{opt} is the optical wavelength[3]. Note that this formalism takes into account the dispersion $dn_{opt}/d\lambda$ at optical frequencies in the nonlinear material.

As can be seen by examination of Eq. 2.4, the coherence length for THz generation is directly dependent on the difference between the indices of refraction at optical and THz frequencies, the so-called "index mismatch". For ZnTe, a commonly used optical rectification material for low-power THz generation, this mismatch is very small (approximately 0.14)[4], giving coherence lengths of several mm for frequencies between 0 and 2 THz[3]. As a result, ZnTe and related zincblende materials, such as GaP and GaSe, are perhaps the most widely used sources for low-power THz pulses with pulse energies on the order of 0.1 nJ being routinely generated using 800 nm femtosecond pulses from commonly available titanium:sapphire laser systems[5]. Optical rectification from GaSe crystals has been demonstrated to give much higher energies, but the frequency of the generated THz pulses is typically above 10 THz[6].

The suitability of a given THz source for use in nonlinear measurements is dependent on the peak THz electric field strength E, which is a function of the temporal duration and area of the THz pulse, and is given by

$$E = \sqrt{\frac{U}{2\pi r^2 cn\varepsilon_0 t}} \tag{2.5}$$

where r is the cross-sectional radius of the THz beam, t is the temporal pulse duration, n is the refractive index of the medium through which the pulse is propagating, c is the speed of light, and U is the pulse energy. Typical literature reports of zincblende-based optical rectification sources give maximum field strengths which range from 0.1 to 10 kV/cm[5]. Such field strengths are inadequate for driving many

important material responses in the nonlinear regime, such as semiconductor impact ionization and ferroelectric switching, which demand field strengths in the range of 100 kV/cm to 10 MV/cm[7,8]. Field strengths up to about 1 MV/cm have been reached using GaSe, but, as mentioned previously, most of the pulse energy is in the long-wavelength IR spectral range, at frequencies exceeding 10 THz[9]. Different approaches are needed for high-power THz generation in the .01-10 THz range, which will be explained in the next section.

2.1.2

Optical Rectification for Higher Power THz Sources

Examination of Eq. 2.5 shows that larger THz fields may be obtained through increasing the THz pulse energy, which is a function of the second-order nonlinear polarization. This implies that THz field strengths may be increased either through selecting a material for optical rectification which possesses a high conversion efficiency (i.e. a large electro-optic tensor element r_{ijk}), or through increasing the amount of optical pump intensity being delivered to the optical rectification material. When applied to the zincblende materials discussed in the previous section, the latter approach immediately fails due to their relatively low damage thresholds[10], necessitating the selection of an alternative optical rectification material for THz sources capable of producing the necessary field strengths for nonlinear THz spectroscopy. It should be noted that μJ level pulse energies may be obtained from ZnTe through the use of a large area crystal[11]; however, the expense and difficulty of obtaining a sufficiently large crystal and the large optical pulse energy needed (and relatively low conversion efficiency) precludes its consideration here.

Efforts to obtain better optical rectification sources for the production of high-energy (and therefore high-field) THz pulses have resulted in two established solutions. The first is the use of exotic

organic crystals, which exhibit extremely high nonlinear coefficients and have been demonstrated to give conversion efficiencies of up to 2%, with resulting field strengths in excess of 1 MV/cm when focused[12]. However, such crystals are difficult to grow and polish and as a result are expensive to obtain, especially in the case of crystals with surface areas large enough for work with amplified 800 nm laser beams, which typically have diameters of approximately 1 cm.

The second solution is to use a material with a high damage threshold, which will allow for the application of much greater optical pumping power. For these purposes, $LiNbO_3$ is an ideal choice, as it exhibits a high nonlinear coefficient (31 pm/V as compared to 4 pm/V for ZnTe[4]), has a high damage threshold, and is readily available commercially. However, a serious technical obstacle to optical rectification in $LiNbO_3$ exists in the form of its high index mismatch between THz and optical frequencies, for which Δn is approximately 3, resulting in an extremely short coherence length[4]. The next section details the solution to this issue, which involves the use of tilted optical intensity fronts for the optical rectification pump pulse.

2.1.3

Optical Rectification in $LiNbO_3$ with Tilted Pulse Fronts

The high degree of index mismatch in $LiNbO_3$ between optical and THz frequencies results in the generation of THz radiation in a Cherenkov cone when optical rectification occurs in $LiNbO_3$. The Cherenkov cone is described by an angle θ_C given by

$$\theta_C = \cos^{-1}\left(\frac{v_{THz}{}^{ph}}{v_{opt}{}^{gr}}\right) \tag{2.6}$$

where v_{THz}^{ph} is the phase velocity of the generated THz radiation and v_{opt}^{gr} is the group velocity of the optical generation pulse[13,14]. This effect can be visualized of through the consideration of wavefronts (the Huygens principle). If the optical pump pulse is considered as a point source, then the THz radiation that it generates will radiate spherically outward from it. If the index mismatch between the optical pump pulse and the generated THz is low, as in the case of the zincblende materials considered earlier, then the phase matching criterion given by Eq. 2.6 is automatically obtained at the leading edge of the generation pulse, i.e. the generated THz is continually amplified as it co-propagates with the optical pulse that is generating it, giving a high conversion efficiency and planar THz pulses. If the index mismatch is large, as in the case of $LiNbO_3$, then the generation pulse immediately "outruns" the radially expanding THz radiation as a result of its lower index, leading to the generation of a series of expanding radial THz patterns, which accumulate into the observed Cherenkov cone (Fig. 2.1 (a)).

The velocity mismatch that is responsible for the appearance of the Cherenkov cone can be corrected through tilting the intensity front of the optical generation pulse (Fig 2.1 (b)), giving the phase-matching condition

$$\cos(\gamma)\, v_{opt}^{gr} = v_{THz}^{ph} \tag{2.7}$$

where the angle γ is the tilt angle specified in Fig. 2.1 (b)[14]. In this scenario, the optical intensity front propagates exactly with the THz radiation that it generates, yielding conversion efficiencies that approach 1×10^{-3} for 800 nm pumping frequencies[15,16]. Phasematching through pulse front tilting forms the underlying basis for the so-called tilted-pulse-front generation technique, which was employed as the THz generation technique for the entirety of the work presented in this thesis. The tilted pulse front corrects for velocity mismatch between the THz radiation and the optical pulse generating it in the direction of the tilt (typically the horizontal direction in the lab and in the $LiNbO_3$ crystal). Mismatch in

the other (vertical) dimension is corrected through the use of a vertical "line" source of optical light that reaches the $LiNbO_3$ crystal at any instant. With the tilted pulse front, the location of this line moves laterally across the $LiNbO_3$ crystal in the horizontal direction as time progresses. The rate of lateral movement matches the Cherenkov angle so that incoming light continues to drive optical rectification at the phase front of the THz field.

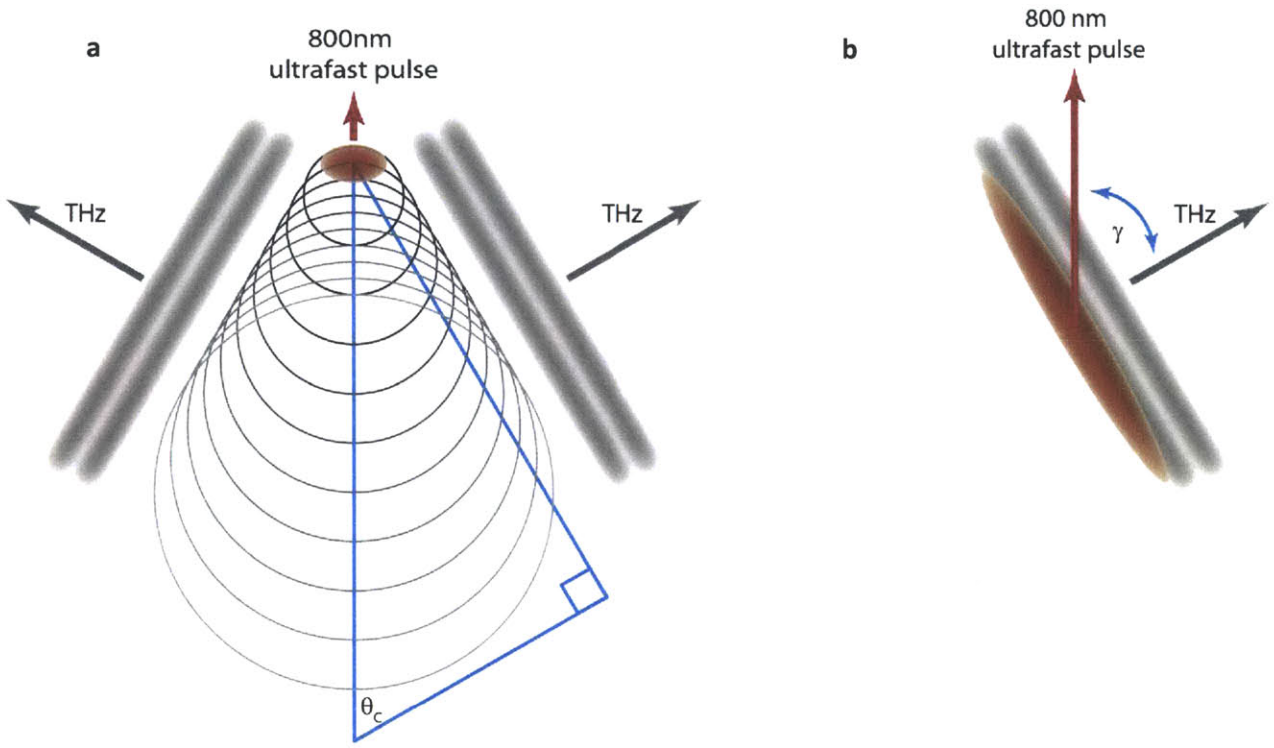

Figure 2.1 (a) Generation of THz in a Cherenkov cone by an ultrafast laser pulse in two dimensions, in which successive radially diverging THz wavefronts combine at angle θ_C. **(b)** Tilting of the optical pulse by the angle γ yields phasematched THz generation, as given by Eq. 2.7.

In practice, tilting of the optical pulse front is accomplished through the use of a diffraction grating, which yields a continuous tilt as a function of the optical wavelength and the grove spacing of the grating employed. Imaging the grating surface (i.e. the tilted pulse) into a $LiNbO_3$ prism, which has been specially cut to match the pulse front tilt angle, yields a compact source of high energy THz pulses. In the experiments presented here, 6.5 mJ, 100 fs duration pulses at 800 nm central wavelength and 1

kHz repetition rate were used as the generation pulses. The tilted-pulse-front setup that was used for all measurements employed a 2000 lines/mm grating, which was imaged in a 2:1 demagnification ratio with a single 8 cm focal length achromatic lens into the $LiNbO_3$ generation prism. The prism was cut to match the tilt angle of 63 degrees (Fig. 2.2). Typical pulse energy conversion efficiencies were 1×10^{-3}, yielding THz pulses with energies of roughly 6.5 μJ. When focused, peak THz electric fields in excess of 730 kV/cm were obtained, with usable frequency components extending to roughly 2.5 THz. Fig. 2.3 shows a typical tilted-pulse-front generated THz pulse, which has been detected by electro-optic sampling (Section 2.3).

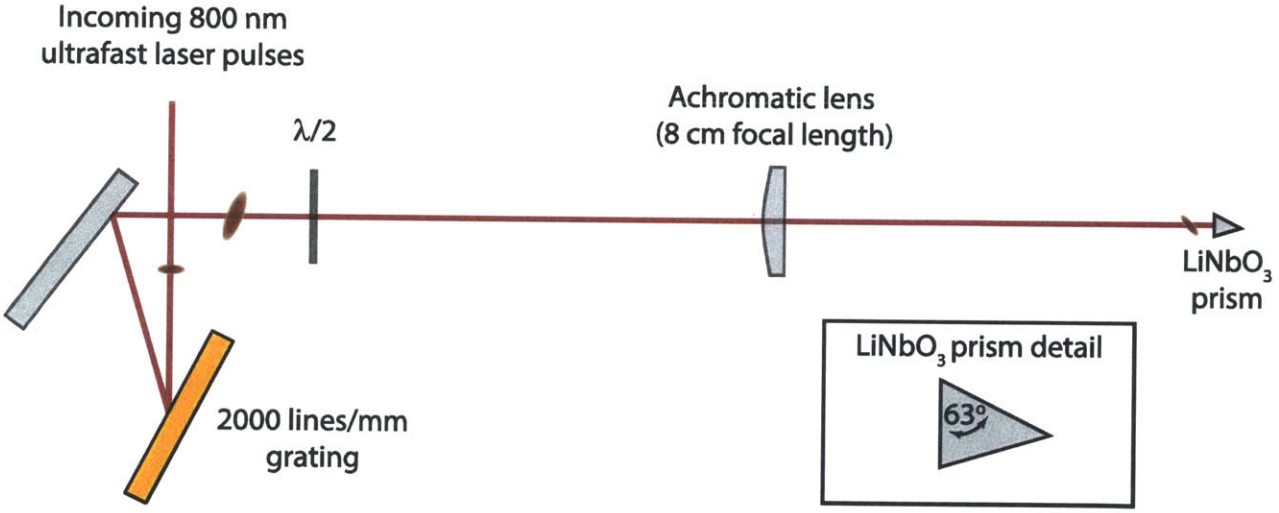

Figure 2.2. Schematic drawing of the tilted-pulse-front source used for generation of high-energy THz pulses. Incoming 800 nm ultrafast pulses are diffracted by a 2000 lines/mm grating. The tilted pulse front is then imaged using a 2:1 demagnification ratio with an achromatic lens (8 cm focal length) into a specially cut $LiNbO_3$ prism, shown in the inset, for which the cut angle is equal to the tilt angle of the 800nm optical pulse once it is imaged into the prism, which in this case is 63°. A half-wave plate is used to flip the polarization of the 800 nm pulse to be parallel to the optic axis in the $LiNbO_3$ prism, which results in vertically polarized THz pulses.

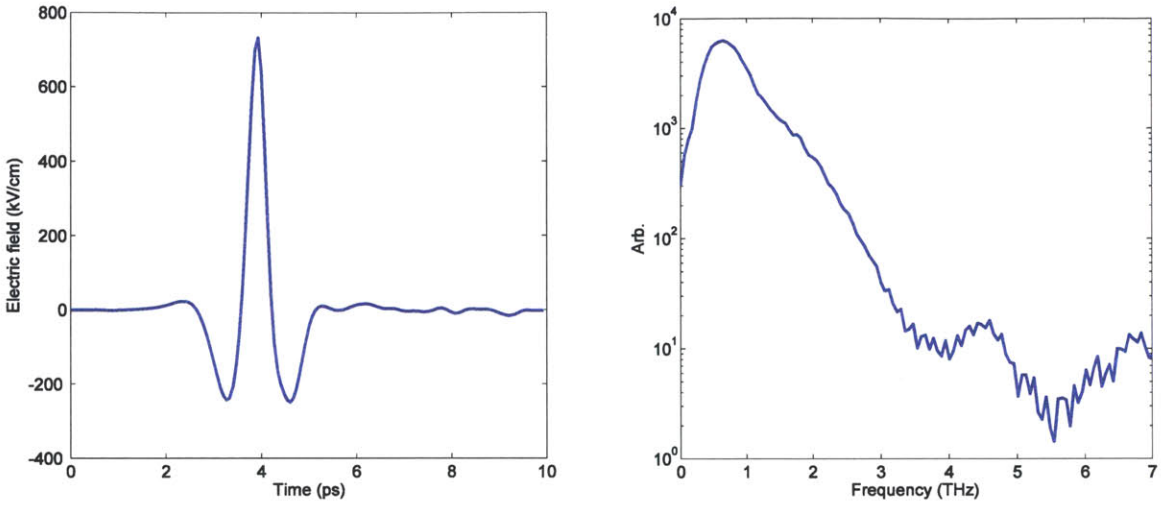

Figure 2.3. THz pulse generated using the tilted-pulse-front setup shown in Fig. 2.2, showing a peak field strength in excess of 700 kV/cm in the time domain (left) and components extending to 2.5 THz in the frequency domain (right).

2.2

Free-Space THz Field Enhancement with Metamaterial Structures

The tilted-pulse-front THz generation technique outlined in the previous section yields THz field strengths on the order of 1 MV/cm, which is sufficiently high for many nonlinear spectroscopy applications. However, field strengths may be increased even more through the use of metamaterial structures, which were used for experiments on silicon impact ionization, air breakdown, and THz-pump/X-ray-probe measurements presented in chapters 4, 5, and 6 of this thesis, respectively.

Metamaterials are patterned structures engineered to mimic bulk material responses when irradiated with a given frequency of electromagnetic radiation. This is accomplished through the use of structures that have geometric features that are far smaller than the wavelength of the applied electromagnetic field yet exhibit coupling to the electric or magnetic fields being applied, yielding an artificially constructed bulk-like electromagnetic response. For frequencies between 0.1 and 10 THz,

which corresponds to wavelengths between 30 μm and 3 mm, sufficiently small structures can be patterned via standard photolithographic techniques[17]. As a result, much progress has been made in recent years toward the use of tailored THz metamaterials in applications including THz sensing, filtering, switching, and modulation[17–23].

One particular class of metamaterials, known as split ring resonators (SRRs), is of interest here due to their ability to provide both localized enhancement of free-space THz fields as well as extremely sensitive localized probing of THz-driven material responses. THz-active SRRs with fourfold symmetries were initially developed to suppress coupling to the applied THz magnetic field, yielding an "all-electric" unit cell, which could then be tailored for specific applications[24]. The SRR pattern used in the work presented here is shown in Fig. 2.4, and consists of a gold structure with four capacitive gaps, each part of which forms an inductive-capacitive (LC) circuit with a characteristic resonance frequency ω_0 approximated by

$$\omega_0 \approx \sqrt{\frac{1}{LC}} \tag{2.8}$$

where L is the inductance and C the capacitance of the circuit, in addition to higher-frequency resonances as a result of the ability of each side of the structure to act as a classical dipole antenna[25]. Significant THz field enhancement, calculated to be up to 10^4 for this type of metamaterial structure, is expected in sufficiently narrow capacitive gaps[24].

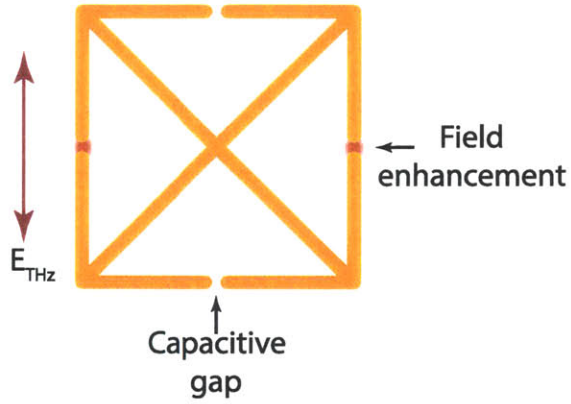

Figure 2.4. Schematic illustration of SRR metamaterial structure used for free-space field enhancement, showing four capacitive gaps, two of which show THz field enhancement for an applied free-space THz field polarized in the vertical direction.

SRR structures therefore present two very useful characteristics for nonlinear THz spectroscopy. First, the ability to enhance free-space THz fields allows for field strengths well above 1 MV/cm to be reached, which allows responses to be driven that were previously inaccessible with benchtop sources. The ability for THz fields to drive nonlinear responses through SRR coupling and field enhancement has been recently demonstrated through THz-driven phase changes in vanadium dioxide and THz-driven impact ionization in gallium arsenide[26,27]. In both cases, SRR coupling resulted in enhancement of the incident free-space THz field to significantly higher levels, which even resulted in THz-induced dielectric breakdown in the case of vanadium dioxide.

Both measurements also made use of the second useful characteristic of SRR metamaterials, which is the high sensitivity of the THz absorption at the LC and dipole resonances to the conductivity of the material within the capacitive gaps of the SRR structure. Previously, this had been demonstrated in sensing applications[21,22] as well as for transient substrate conductivity changes driven by ultrafast laser pumping[17,28]. In the case of the nonlinear THz measurements, THz probing of the SRR LC resonance revealed conductivity changes induced by the strong THz pump fields, either by examination of the transmitted THz pump pulse or through the use of a time-delayed THz probe pulse. As such, even

though the nonlinear response only occurs within the micron-scale capacitive gaps, which represent a small percentage of the sample area illuminated by the THz probe pulse, the signal measured by the probe field is extremely sensitive to the changes in conductivity within the gaps because of the resulting SRR resonance frequency shifts.

For the measurements presented in this thesis, all metamaterial structures utilized were designed, fabricated, and simulated by Kebin Fan, Xiaoguang Zhao, and others in the research groups of Richard Averitt and Xin Zhang at the Boston University Photonics Center.

2.3

Electro-Optic Detection of Free-Space THz Radiation

As a result of the very low photon energies of THz-frequency electromagnetic waves, detection of free-space THz pulses is accomplished through methods that bear little resemblance to the methods typically used for detection of higher-frequency light sources. While area detectors, which are based on pyroelectric or bolometer sensors, are commercially available, no frequency-dependent detection has yet been developed which is sufficient for spectroscopic purposes. Instead, time-domain detection is typically used, which employs pulses from the ultrafast laser that is also used for THz generation.

For the work presented in this thesis, time-domain electro-optic sampling (EOS) detection was used. EOS is based on the Pockels effect, which is a second order nonlinear optical effect in which an electric field is applied to a non-centrosymmetric material that exhibits a $\chi^{(2)}$ susceptibility[1]. The application of the electric field generates a change Δn in the index of refraction of the material along a specific direction, which is determined by the material symmetry and the polarization direction of the applied field, thereby resulting in a field-induced birefringence.

EOS for time-domain THz detection makes use of an ultrafast optical probe pulse that may be time-delayed relative to the THz pulse and is much shorter in duration than the THz pulse. This allows for the electric field of the THz pulse to be treated as quasi-DC field when gated by the ultrafast optical probe pulse. When the THz field is overlapped with the probe pulse in an electro-optic crystal (typically GaP or ZnTe, as were used for all work in this thesis), the transient birefringence induced by the electric field of the THz pulse in the electro-optic crystal as a result of the Pockels effect modifies the polarization of the probe pulse. The extent of the modification of the probe pulse polarization is directly related to the magnitude of the applied electric field. Scanning the relative delay between the THz and optical pulses sweeps the ultrafast probe pulse over the much longer THz pulse. Therefore, detection of the degree of birefringence induced by the THz pulse, though detection of the degree of polarization modification present in the probe pulse as a result of the THz-induced birefringence, allows the time-domain electric field profile of the THz pulse to be mapped out (shown schematically in Fig 2.5 (a)). The THz field profile in Fig. 2.3 was detected using EOS.

When a linearly polarized probe pulse is used, the degree of depolarization induced by the THz-driven Pockels effect can be measured using the polarization-sensitive optical setup shown in Fig. 2.5 (b), in which the vertical and horizontal polarization components of the probe pulse are balanced by a quarter-wave plate, separated by a Wollaston prism, and detected by a pair of photodiodes. The difference in intensity between the two photodiodes is related to the magnitude of the applied THz field through

$$E_{THz} = \sin^{-1}\left(\frac{\Delta I}{I}\right)\left(\frac{\lambda}{2\pi n^3 r_{41} l}\right) \tag{2.9}$$

where λ is the wavelength of the probe pulse, n is the refractive index of the electro-optic crystal at the probe pulse frequency, l is the length of the electro-optic crystal through which the probe and THz

pulses propagate (i.e. the crystal thickness at normal incidence), r_{41} is the electro-optic tensor component, and

$$\frac{\Delta I}{I} = \frac{A-B}{A+B} \tag{2.10}$$

gives the degree of probe depolarization where *A* and *B* are the intensities at the two photodiodes in Fig 2.5 (b). Note that in most cases the inverse sine in Eq. 2.9 may be neglected, as the degree of probe depolarization is typically quite small. Furthermore, Eq. 2.9 assumes linear probe and THz polarizations, with either 0° or 90° relative orientation[29].

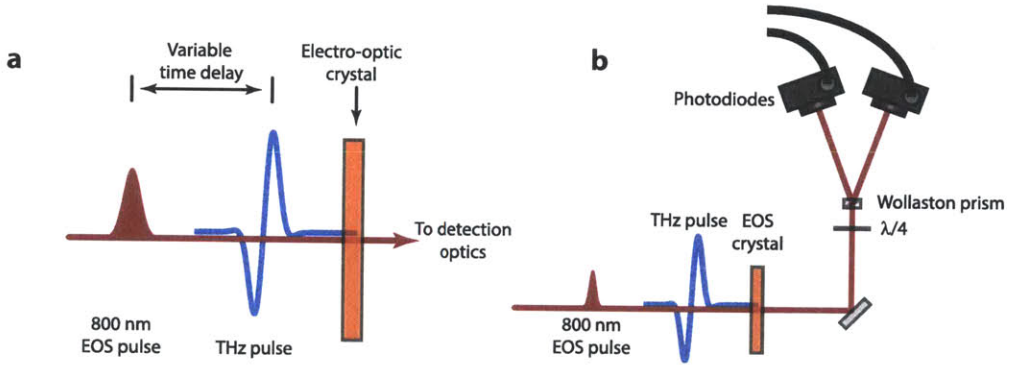

Figure 2.5. (a) Schematic representation of EOS, in which a short optical probe pulse is overlapped with the THz pulse in an electro-optic crystal. The probe pulse is swept over the THz pulse in time using an optical delay stage, and a readout of the THz-induced transient birefringence in the electro-optic crystal records the time-domain profile of the THz electric field. **(b)** Balanced polarization-sensitive detection scheme for EOS.

2.4

Data Analysis for THz Transmission Spectroscopy

THz spectroscopy, as presented in the preceding sections, is detected in the time domain, as evidenced by Fig. 2.3 (a). Material responses, however, are typically manifested as frequency-specific

absorptions, necessitating frequency-dependent data analysis (though exceptions, such as broadband conductivity responses in semiconductors[30], do exist).

The experiments presented in this thesis rely heavily upon enhancement of free-space THz fields by metamaterial structures. Extraction of material parameters such as the frequency-dependent index of refraction and absorption coefficient carries little physical meaning, as these parameters are heavily dependent on the electromagnetic response of the metamaterial structures themselves. As a result, it is sufficient to examine the frequency-dependent THz transmission and optical density. This is done by collecting two THz pulses, one that is passed through the sample of interest and one that is passed through a reference, which is typically air or, in the cases of samples mounted on a substrate, a piece of the substrate being used. A ratio of the Fourier transforms of the sample and reference THz pulses gives the frequency-dependent transmission as

$$T(\upsilon) = \frac{\left|\int_{-\infty}^{\infty} E_{sam} e^{-i2\pi\upsilon t}\right|^2}{\left|\int_{-\infty}^{\infty} E_{ref} e^{-i2\pi\upsilon t}\right|^2} \tag{2.11}$$

where E_{sam} and E_{ref} represent the time-domain THz pulses that were passed through the sample and reference, respectively. The frequency-dependent THz absorption of the sample is then obtained as the negative common logarithm of Eq. 2.11:

$$A(\upsilon) = -\log\left(\frac{\left|\int_{-\infty}^{\infty} E_{sam} e^{-i2\pi\upsilon t}\right|^2}{\left|\int_{-\infty}^{\infty} E_{ref} e^{-i2\pi\upsilon t}\right|^2}\right) \tag{2.12}$$

2.5

Conclusions

Nonlinear THz spectroscopy is made possible primarily through adaptations of existing THz spectroscopy techniques. THz pulses with sufficiently high electric fields to induce nonlinear material responses are generated through optical rectification in $LiNbO_3$ via the tilted-pulse-front technique, in which the intensity front of an ultrafast 800 nm pulse is tilted in space by a grating so that phasematching may be achieved, resulting in a high conversion efficiency. Enhancement of the resulting free-space THz pulses may be obtained through the use of metamaterial structures, which can also be designed to function as sensitive probes of THz-driven nonlinearities. THz detection through EOS and data analysis in the frequency domain complete the set of techniques that will be used to drive and analyze nonlinear THz responses throughout the rest of the work presented in this thesis.

References

1. Boyd, R. W. *Nonlinear Optics*. (Academic Press, 2008).

2. Kleinman, D. A. & Auston, D. H. Theory of electrooptic shock radiation in nonlinear optical media. *IEEE J. Quantum Electron.* **20,** 964 (1984).

3. Nahata, A., Weling, A. S. & Heinz, T. F. A wideband coherent terahertz spectroscopy system using optical rectification and electro-optic sampling. *Appl. Phys. Lett.* **69,** 2321 (1996).

4. Hebling, J., Stepanov, A. G., Almasi, G., Bartal, B. & Kuhl, J. Tunable THz pulse generation by optical rectification of ultrashort laser pulses with tilted pulse fronts. *Appl. Phys. B Lasers Opt.* **78,** 593 (2004).

5. Löffler, T. *et al.* Comparative performance of terahertz emitters in amplifier-laser-based systems. *Semicond. Sci. Technol.* **20,** S134 (2005).

6. Huber, R., Brodschelm, A., Tauser, F. & Leitenstorfer, A. Generation and field-resolved detection of femtosecond electromagnetic pulses tunable up to 41 THz. *Appl. Phys. Lett.* **76,** 3191 (2000).

7. Kunikiyo, T. *et al.* A Monte Carlo simulation of anisotropic electron transport in silicon including full band structure and anisotropic impact-ionization model. *J. Appl. Phys.* **75,** 297 (1994).

8. Qi, T., Shin, Y.-H., Yeh, K.-L., Nelson, K. & Rappe, A. Collective coherent control: synchronization of polarization in ferroelectric $PbTiO_3$ by shaped THz fields. *Phys. Rev. Lett.* **102,** 247603 (2009).

9. Junginger, F. *et al.* Single-cycle multiterahertz transients with peak fields above 10 MV/cm. *Opt. Lett.* **35,** 2645 (2010).

10. Liu, J., Schmutz, H. & Merkt, F. Generation of widely tunable Fourier-transform-limited terahertz pulses using narrowband near-infrared laser radiation. *J. Mol. Spectrosc.* **256,** 111 (2009).

11. Blanchard, F. *et al.* Generation of 1.5 μJ single-cycle terahertz pulses by optical rectification from a large aperture ZnTe crystal. *Opt. Express* **15,** 13212 (2007).

12. Vicario, C., Ruchert, C. & Hauri, C. P. High field broadband THz generation in organic materials. *J. Mod. Opt.* (2013). doi:10.1080/09500340.2013.800242

13. Auston, D. H., Cheung, K. P., Valdmanis, J. A. & Klienman, D. A. Cherenkov radiation from femtosecond optical pulses in electro-optic media. *Phys. Rev. Lett.* **53,** 1555 (1984).

14. Hebling, J., Almasi, G., Kozma, I. & Kuhl, J. Velocity matching by pulse front tilting for large area THz-pulse generation. *Opt. Express* **10,** 1161 (2002).

15. Yeh, K.-L., Hoffmann, M. C., Hebling, J. & Nelson, K. A. Generation of 10 μJ ultrashort terahertz pulses by optical rectification. *Appl. Phys. Lett.* **90,** 171121 (2007).

16. Yeh, K.-L., Hebling, J., Hoffmann, M. C. & Nelson, K. A. Generation of high average power 1 kHz shaped THz pulses via optical rectification. *Opt. Commun.* **281,** 3567 (2008).

17. Padilla, W. J., Taylor, A. J. & Averitt, R. D. Dynamical electric and magnetic metamaterial response at terahertz frequencies. *Phys. Rev. Lett.* **96,** 107401 (2006).

18. Chen, H.-T. *et al.* Complementary planar terahertz metamaterials. *Opt. Express* **15,** 1084 (2007).

19. Tao, H. *et al.* Reconfigurable terahertz metamaterials. *Phys. Rev. Lett.* **103,** 147401 (2009).

20. Tao, H. *et al.* A dual band terahertz metamaterial absorber. *J. Phys. D. Appl. Phys.* **43,** 225102 (2010).

21. Tao, H. *et al.* Performance enhancement of terahertz metamaterials on ultrathin substrates for sensing applications. *Appl. Phys. Lett.* **97,** 261909 (2010).

22. Tao, H. *et al.* Metamaterials on paper as a sensing platform. *Adv. Mater.* **23,** 3197 (2011).

23. Fan, K. *et al.* Optically tunable terahertz metamaterials on highly flexible substrates. *IEEE Trans. Terahertz Sci. Technol.* **3,** 702 (2013).

24. Padilla, W. *et al.* Electrically resonant terahertz metamaterials: Theoretical and experimental investigations. *Phys. Rev. B* **75,** 041102 (2007).

25. Tao, H., Padilla, W. J., Zhang, X. & Averitt, R. D. Recent progress in electromagnetic metamaterial devices for terahertz applications. *IEEE J. Sel. Top. Quantum Electron.* **17,** 92–101 (2011).

26. Liu, M. *et al.* Terahertz-field-induced insulator-to-metal transition in vanadium dioxide metamaterial. *Nature* **487,** 345 (2012).

27. Fan, K. *et al.* Nonlinear terahertz metamaterials via field-enhanced carrier dynamics in GaAs. *Phys. Rev. Lett.* **110,** 217404 (2013).

28. Fan, K., Strikwerda, A., Zhang, X. & Averitt, R. Three-dimensional broadband tunable terahertz metamaterials. *Phys. Rev. B* **87,** 161104 (2013).

29. Planken, P. C. M., Nienhuys, H.-K., Bakker, H. J. & Wenckebach, T. Measurement and calculation of the orientation dependence of terahertz pulse detection in ZnTe. *J. Opt. Soc. Am. B* **18,** 313 (2001).

30. Hebling, J., Hoffmann, M. C., Hwang, H. Y., Yeh, K.-L. & Nelson, K. A. Observation of nonequilibrium carrier distribution in Ge, Si, and GaAs by terahertz pump–terahertz probe measurements. *Phys. Rev. B* **81,** 035201 (2010).

Chapter 3

Terahertz Spectrometer Design, Development, and Enhancement

Central to the continued development of nonlinear THz spectroscopy is the design and construction of spectroscopic instruments that efficiently incorporate THz sources in ways that allow for the desired measurement to be optimally performed yet flexible enough to be used for multiple nonlinear spectroscopy techniques. Such instrument design is not trivial, as THz sources and optics are typically large and inflexible, and THz spectroscopies exhibit markedly different features than their optical counterparts. The aim of this chapter is therefore to illustrate the considerations which must be made when designing a nonlinear THz spectrometer for use in a typical ultrafast laser lab, including spectrometers incorporating both optical and/or THz probing. Furthermore, recent progress towards higher THz field strengths made by way of upgrades to the THz collection and focusing optics will be discussed. Design of THz spectrometers incorporating ultrafast X-ray diffraction probing will be discussed in Chapter 6 due to their unique requirements as a result of being located at a beamline facility.

3.1

Basic THz Collection, Focusing, and Use

The majority of commonly used free-space ultrafast THz spectrometer configurations consist of three THz components: a source of THz pulses, optics to collect and focus the THz radiation, and some form of THz detection, with an ultrafast laser source being used to both generate and detect THz fields. The multiple-octave bandwidths characteristic of most ultrafast THz sources demand the use of reflective THz optics, and as a result, off-axis parabolic reflectors (OAPs) are frequently chosen for THz collection and focusing due to their wide-ranging commercial availability. In a spectrometer designed for THz transmission spectroscopy with an initially diverging THz source (a commonly encountered linear THz spectrometer layout in the literature[1–3], and the scenario used throughout this thesis as depicted in Fig. 1), four OAPs are typically used, so that the generated THz radiation is collected, focused through a sample, re-collected, and focused into the THz detection crystal.

As discussed in the previous chapter, the THz detection method chosen in all cases for the work presented in this thesis is electro-optic (EO) sampling, which is implemented by overlapping a time-delayed 800 nm pulse with the THz beam and focusing both into an EO crystal. With respect to instrument design, EO detection adds the additional stipulation that an 800 nm beam be overlapped with the THz radiation somewhere in between the point of generation and the EO detection crystal. Furthermore, the OAPs used for THz focusing and collection are typically produced via a machining process which leaves their surfaces too rough to be used as the focusing optic for the 800 nm EO sampling beam (though using THz OAPs as 800 nm focusing optics is still possible, as will be seen in subsequent sections). As a result, it is usually preferable to employ a separate 800nm focusing optic. Therefore, the overlap between the 800 nm and THz beams is typically best accomplished after the last OAP and prior to the EO crystal. In most cases, this is done either via inserting a thin pellicle

beamsplitter into the focusing THz beam (as was done for most of the work in this thesis) or by simply drilling a hole into the last OAP. The basic configuration outlined thus far, consisting of four OAPs for THz handling and time-delayed EOS detection, is shown in Fig. 3.1.

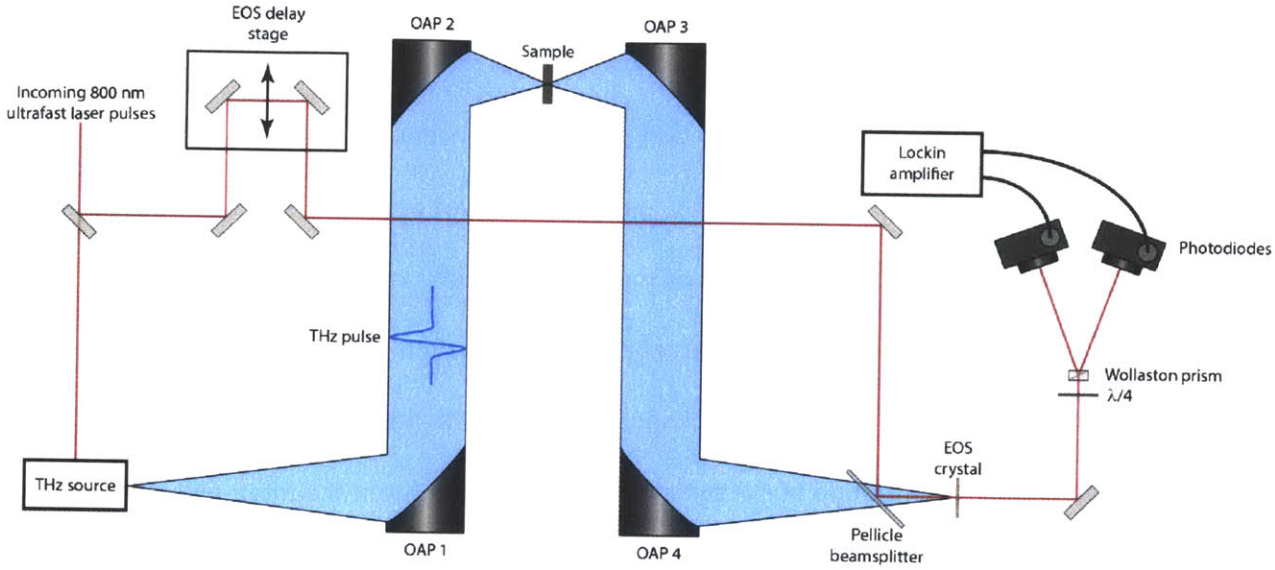

Figure 3.1. Schematic illustration of ultrafast 800 nm laser-driven THz spectrometer configuration with four OAPs for THz handling, EOS for THz detection, and an arbitrary THz souce. THz and 800 nm overlap for EOS is accomplished with a pellicle beamsplitter.

It is at this point that the design of a nonlinear THz spectrometer diverges from its lower-powered linear counterpart through the selection of the THz source. The combination of the THz collection and detection described above with a low-energy THz source, such as the commonly used ZnTe optical rectification technique described in the previous chapter, yields a spectrometer capable of collecting linear THz absorption spectra[3,4]. The most basic iteration of a nonlinear THz spectrometer is accomplished by simply substituting the ZnTe THz source with the tilted-pulse-front source described in the previous chapter. The following sections will expand upon this basic design and describe the development of a tilted-pulse-front-based nonlinear THz spectrometer suitable for a wide range of applications, beginning with specific considerations that must be taken into account for high-power THz sources.

3.2

Collection Optics for Tilted-Pulse-Front Sources

The phase matching associated with the tilted-pulse-front THz source makes the proper collection and handling of the produced THz a nontrivial issue, as the level of divergence associated with the THz radiation as it exits the $LiNbO_3$ generation prism is dependent on the bandwidth and central frequency of the ultrafast laser pulse used for THz generation as well as the method and optics used to image the tilted optical pulse into the $LiNbO_3$ prism[5]. Recent reports of very high THz field strengths have hinged upon the manipulation of this divergence in combination with collection optic choice in order to yield optimal focusing efficiency and hence maximum THz field strengths[6]. Such techniques have relied upon precise optimization of the optical imaging components in the tilted-pulse-front setup while observing the resulting THz divergence using a THz microbolometer array camera. The reported field strengths of 1.2 MV/cm are produced when the divergence of the THz beam is minimized, i.e. the THz beam is treated as a collimated source. Such a source may then be focused relatively tightly by a small OAP, generating a small divergent spot, which may then be handled using the standard set of four OAPs described in the previous section.

The work described here, however, takes an approach that relies instead on a simpler one-lens imaging technique. This yields a THz source that exhibits a similar degree of divergence in both the horizontal and vertical directions, as opposed to the anisotropic THz divergence associated with two-lens optical focusing[5,6]. As a result, it may be treated not as a collimated beam but rather as a point source, which may then be imaged and detected using four OAPs without the need for a first small OAP for focusing. Because the one-lens technique gives relatively little control over the divergence of the generated THz pulses, the efficiency of the tilted-pulse-front generation may be optimized with a single-element pyroelectric detector, eliminating the need for a costly THz area detector. Optimization under

this method may be accomplished fairly quickly, allowing for the nonlinear THz spectrometer to be re-used for many spectroscopic techniques in a short period of time, which is an important consideration if spectrometer versatility is desired (as is the case here).

Treating the THz source as a divergent point source implies that the collection efficiency of the optics chosen to handle the THz radiation depends directly on the numerical aperture (NA) of the first collection optic, while the attainable THz field strength is dependent on the demagnification ratio of the collection and focusing optics chosen, i.e. the first and second OAPs. These parameters are set through the choice of the OAPs to be used, as the NA of the first optic is determined by its diameter and effective focal length (EFL), and the demagnification M of the THz spot is given by

$$M = \frac{EFL_1}{EFL_2} \tag{3.1}$$

where EFL_1 and EFL_2 are the EFLs of the first and second OAPs, respectively. In practice, these parameters are carefully balanced based on a variety of considerations mostly related to the physical size of the OAPs being considered, namely the optimization of THz collection and imaging ratio while still allowing sufficient space for samples, THz optics, and EO detection to be placed in their intended locations without mechanical interference from the OAPs.

At this point, it is important to note a significant difference between THz and optical spectroscopy regarding the applicability of ray optics to spectrometer design. Both optical and THz coherent sources may be accurately described as Gaussian beams, for which the divergence angle θ_0 at long distances from a beam waist is given by

$$\theta_0 = \frac{\lambda}{\pi W_0} \tag{3.2}$$

where λ is the wavelength of the beam and W_0 is its initial waist[7]. Assuming that collimation is achieved at a divergence of 1 mrad, which is typical of commercial laser sources, solving Eq. 3.3 for W_0 yields the approximate collimation criterion given in Eq. 3.3, which is taken here as the criterion for which ray optics becomes applicable:

$$W_0 \geq 318.3\lambda \tag{3.3}$$

For a wavelength of 800nm, Eq. 3.3 shows that collimation is achieved for waists above roughly 500 μm in diameter, while at 1 THz (300 μm wavelength), collimation is not achieved until a minimum initial diameter of approximately 19 cm, which is far greater than the diameter of commercially available OAP reflectors (typically ranging from 2.5 to 10 cm). As a result, the ray optics limit is not applicable to most THz spectrometer designs, and therefore THz sources must be treated as Gaussian throughout the entirety of their propagation. This implies that the OAPs chosen to handle THz must be positioned to exactly image the generated THz spot to the sample and then to the THz detection, which adds additional constraints to spectrometer design.

3.3

Constructed Nonlinear THz Spectrometer

The majority of the work presented in this thesis was performed on an instrument designed to adhere to the collection optics guidelines outlined in Section 3.2, while being able to operate in several experimental configurations, which will be detailed in the following section. A minority of the measurements in the following chapters were performed on the original iteration of this instrument, in which it was equipped with OAPs having EFLs of 7.5, 3, 4, and 7.5 inches (190.5, 76.2, 101.6, and 190.5

mm, respectively) with 2 inch (50.4 mm) diameters. This mirror configuration was originally specified in order to accommodate a liquid helium cryostat between the second and third OAP for low-temperature measurements. However, the work described in this thesis did not require low-temperature measurements, allowing for this constraint to be removed. Therefore, in an attempt to increase field strengths, four OAPs with EFLs of 5 and 2 inches (127 and 50.8 mm, respectively) and diameters of 3 inches (76.2 mm) were substituted, resulting in higher collection efficiency while preserving the original demagnification ratio of 2.5. This configuration, which was used for the majority of the work presented in the following chapters, is shown in all subsequent illustrations.

A THz intensity measurement at the focus of the second OAP was made using a microbolometer array camera (NEC model IRV-T0831), which showed an approximately round THz spot (Fig. 3.2 (a)). Gaussian fits to cross sections in the horizontal and vertical dimension (Fig. 3.2 (b)) reveal full width half maximum values of 365 and 350 μm, respectively, which is on the order of previously reported results using the three-mirror handling described in the previous section[6], indicating that optimal THz focusing is indeed possible with a divergent THz source (i.e. a tilted-pulse front source using one 800 nm lens, rather than two lenses). EO sampling traces taken at the focus of the fourth OAP reveal peak THz electric fields in excess of 730 kV/cm at the focus of the second OAP, which is calculated by applying the demagnification ratio of 2.5 to the calculated electric field at the fourth OAP focus (this data appears in Fig. 2.3 in the previous chapter).

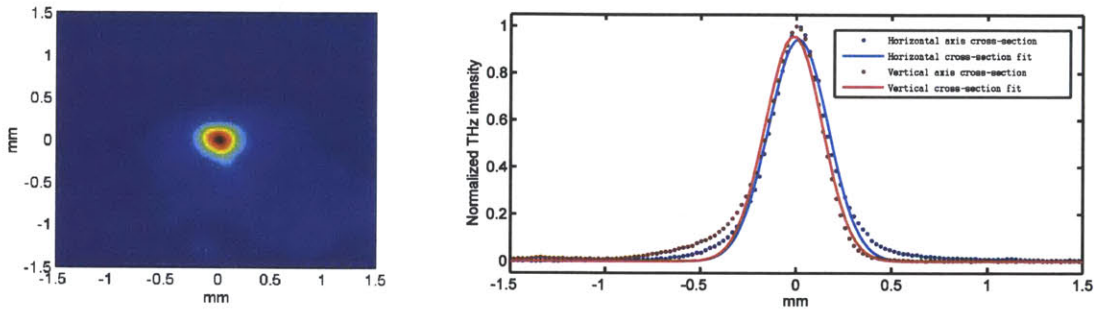

Figure 3.2. (a) Image of focused THz spot taken with a microbolometer array camera positioned after the second OAP reflector. **(b)** Gaussian fits to cross sections in the vertical and horizontal directions.

3.4

Experimental Geometries for Various Types of Nonlinear THz Measurements

3.4.1

Nonlinear Transmission Measurements

By many metrics, including spectrometer design, the simplest possible nonlinear THz measurement is a series of transmission scans at varying THz field strengths. Such a series of measurements, referred to collectively as a nonlinear transmission measurement, may be used to reveal both electronic and vibrational nonlinearities in a broad variety of systems[8–10]. Furthermore, enhancement of the incident THz fields with metamaterial SRR structures greatly expands the sensitivity and utility of this technique due to the extreme sensitivity of the LC resonance to the in-gap conductivity[11,12], as explained in the previous chapter. Such a measurement is therefore a fairly common starting point in many nonlinear THz investigations and is present in some capacity in the experiments described in Chapters 4 and 5 of this thesis.

Design and construction of a spectrometer for this type of measurement requires only a single modification to the generic tilted-pulse-front THz spectrometer described in the previous sections, namely the insertion of a pair of wiregrid polarizers, which are effective across the entire bandwidth generated by the tilted-pulse-front source, as is illustrated in Fig. 3.3. The electric field transmitted through the pair of polarizers is given by

$$E = E_0 \cos^2 \theta \tag{3.4}$$

where E_0 is the incident field and θ is the relative angle between the two polarizers. Thus, keeping the second polarizer fixed while rotating the first gives a field that varies according to Eq. 3.4 but maintains a constant polarization.

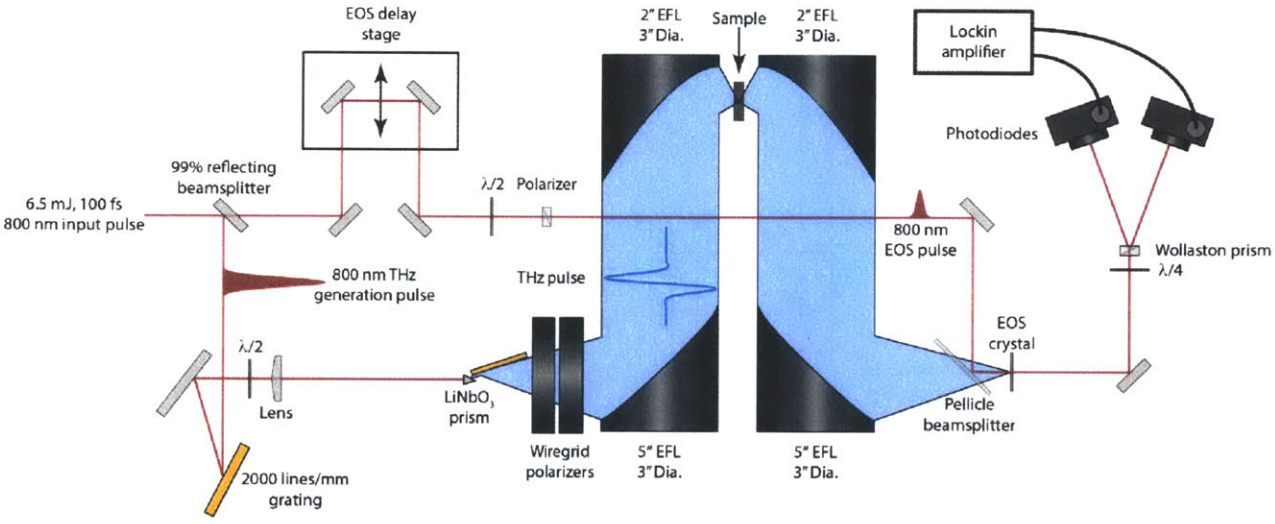

Figure 3.3. THz spectrometer in nonlinear transmission geometry. 99% of the incoming 800nm beam is used for THz generation, while 1% is time-delayed and attenuated with a waveplate/polarizer combination for use as the EOS probe pulse. The pair of wiregrid polarizers after the $LiNbO_3$ generation prism allows for variability of the THz electric field.

3.4.2

THz-Pump/Optical-Probe Measurements

The nonlinear transmission measurements described in the previous section are capable of observing a THz-driven nonlinearity, provided that it occurs on the time scale of the THz pulse duration, but yield no information beyond that regarding the dynamics associated with the growth or decay of the nonlinear response. Obtaining dynamical information therefore requires a time-delayed probe pulse. For many measurements involving both electronic[10,13,14] and nuclear motion[15,16], including the THz Stark effect measurements described in Chapter 7 of this thesis, a probe pulse in the visible region of the electromagnetic spectrum is necessary, and also offers greater time resolution than the time-delayed THz probe described in the next section due to the shorter pulse durations available at optical frequencies. In this case, the basic tilted-pulse-front THz spectrometer is typically modified to include only two OAPs, as the time-delayed optical beam used for THz EO detection is typically also used as the optical probe pulse, as shown in Fig. 3.4.

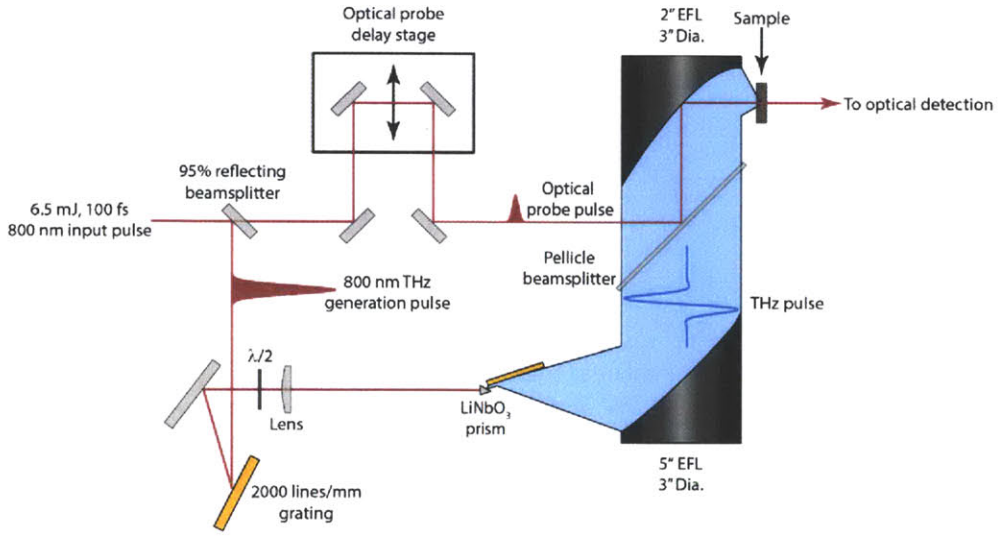

Figure 3.4. THz spectrometer in THz-pump/optical-probe geometry. Note that this is a generic setup, in which the type of optical detection is not specified, and that the second pair of OAPs is omitted for simplicity.

3.4.3

THz-Pump/THz-Probe Measurements

Nonlinear THz spectroscopy, by definition, relies on THz-active degrees of freedom. As a result, a time-delayed probe in the THz spectral region is extremely desirable as a monitor of THz-driven nonlinear behavior, but is technically challenging due to the size of the optics necessary for THz generation and detection as well as the difficulty associated with aligning independent THz sources to a common focus. THz-pump/THz-probe measurements presented in this thesis (Chapters 4 and 5) utilize a collinear arrangement, in which the THz source, handling optics, and detection are not directly modified. Instead, the optical beam used for THz generation is split in a 95%/5% ratio prior to the tilted-pulse-front source and recombined on the grating used for pulse front tilting, with one path time-delayed using a mechanical delay line (Fig. 3.5). This results in two THz pulses with a variable relative time delay without the need for complicated OAP arrangements and the potential risk of lower THz field strengths as a result of associated sacrifices in focusing efficiency. The approach has been demonstrated in a variety of systems[10,11,17–19]. In the collinear arrangement, typical pump and probe foci offsets at the sample focus are on the order of 100 μm, or well within the roughly 400 μm diameter of the THz focus (see Section 3.3). It should also be noted that, owing to the reliance on a common $LiNbO_3$ generation prism for both the pump and probe pulses, the temporal region immediately around the overlap of the pump and probe pulses is obscured due to interactions of the optical pulses used for THz generation in the $LiNbO_3$ prism, which are necessarily temporally overlapped as well during this time window. This window of inaccessibility is typically around 5 ps in total, spanning from -2.5 to +2.5 ps around the position of the pump/probe overlap. For all of the work presented in this thesis, the timescales of the observed THz dynamics were significantly longer than this window.

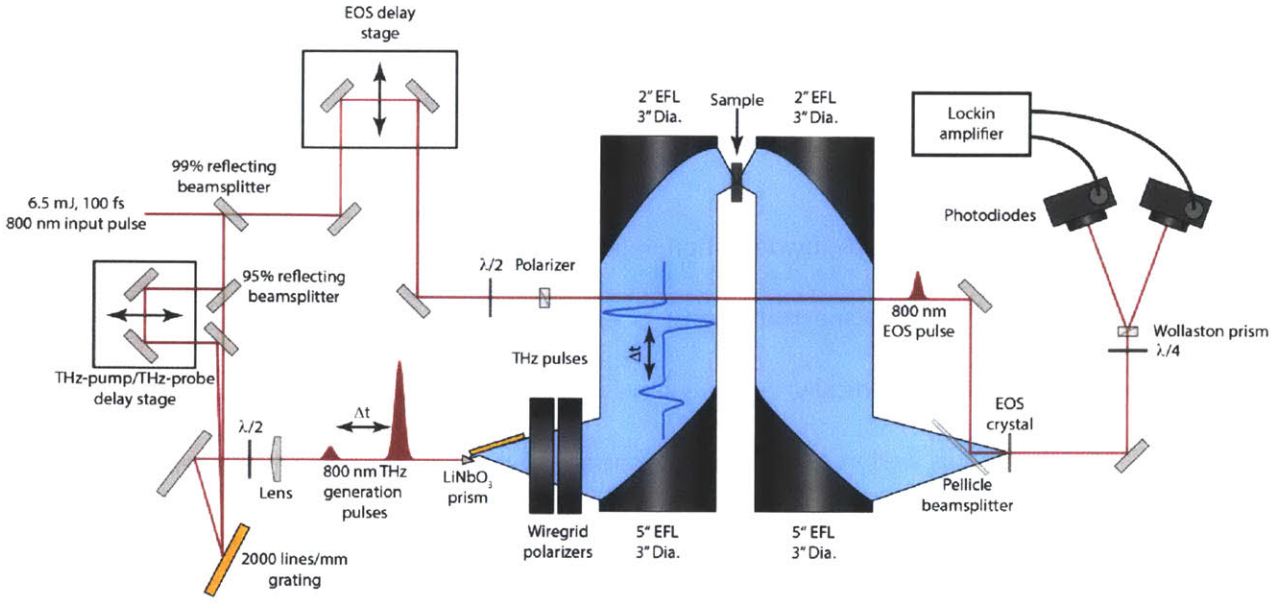

Figure 3.5. THz spectrometer in THz-pump/THz-probe geometry. 1% of the incoming 800 nm beam is reserved for EOS, while the remaining 99% is split in a 95%/5% ratio to produce a pair of time-delayed optical pulses. Recombination on the tilted-pulse-front grating produces a pair of time-delayed THz pulses.

3.4.4

THz-Pump/ISRS-Probe Measurements

THz probing following THz pumping, while giving valuable insight into THz-frequency material responses, is limited in its application due to the constraints it imposes on the classes of samples to which it may be applied. Specifically, it demands that the sample absorb enough of the THz pump pulse to drive the desired nonlinear response, yet transmit enough of the THz probe pulse such that quantitative absorption measurements may still be made (though THz probing in reflection mode is possible, it is cumbersome and has further design-related difficulties that are not discussed here). Furthermore, solid samples must maintain a minimum thickness of approximately 0.7 mm/n, where n is the refractive index at THz frequencies, to avoid unwanted effects of closely-spaced THz etalon reflections. For many samples, these constraints are difficult to meet.

Probing Raman-active modes, which can be done using wavelengths in the visible region of the spectrum, forms a convenient work-around to this problem, as samples which would ordinarily be disqualified for any of the above reasons may present no impediment to the transmission of, for example, an 800 nm ultrafast pulse. On the femtosecond timescale, impulsive stimulated Raman scattering (ISRS), which will be described in detail in Chapter 7, is a convenient form of coherent Raman probing for low-frequency vibrational modes that are driven or perturbed by the THz excitation pulse. In its simplest form, ISRS requires the overlap of an 800 nm pump pulse with a time-delayed 800 nm probe pulse whose transmission is detected through a narrowband filter[20]. Implementation into a THz spectrometer results in a layout very similar to the THz-pump/optical probe layout in Section 3.4.2 but with an additional time-delayed 800 nm arm. Overlapping of the 800 nm pulses with each other and the THz pump pulse is achieved by using the second THz OAP as a common focusing optic, with vertical offsetting of the 800 nm beams for spatial separation, as shown in Fig. 3.6.

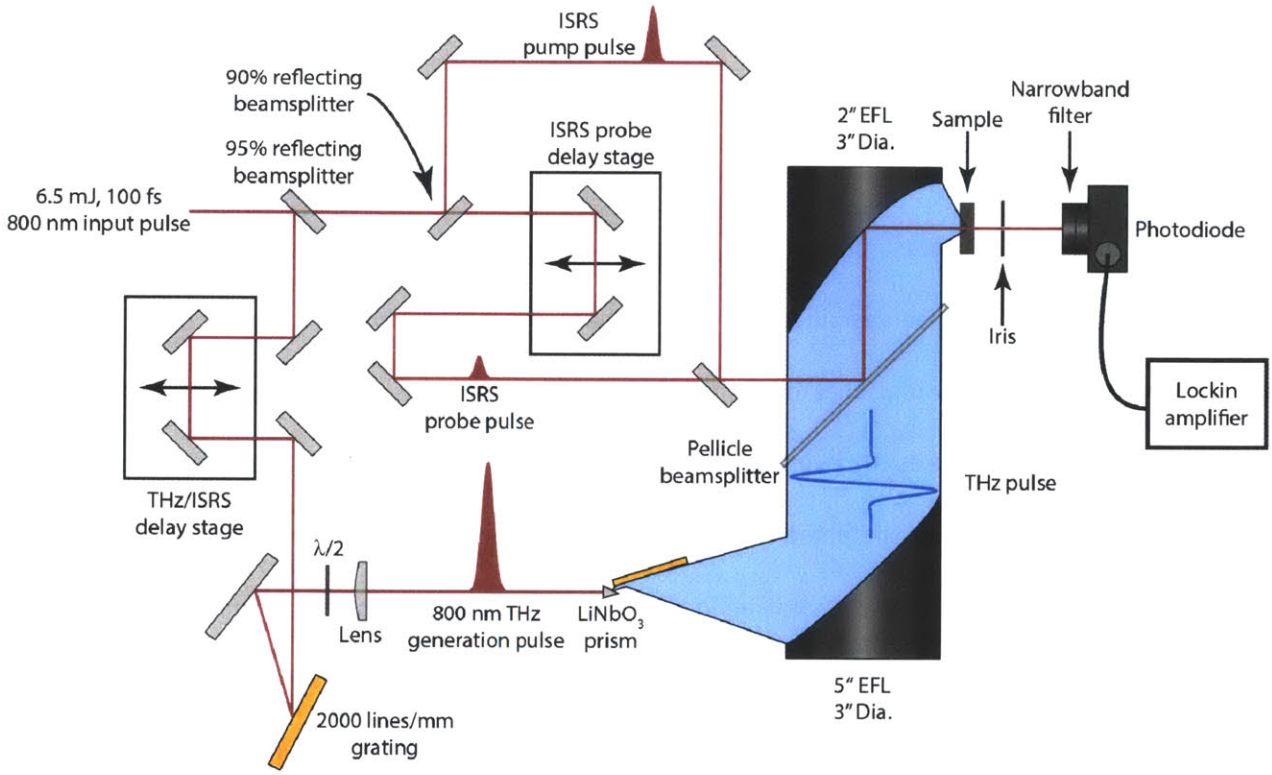

Figure 3.6. THz spectrometer in THz-pump/ISRS-probe geometry. Incoming 800 nm pulses are split 95%/5% as in the THz-pump/optical-probe setup in Section 3.4.2. In this case the 5% is split again in a 90%/10% ratio, producing a pair of 800 nm pulses which are delayed relative to each other as well as relative to the THz pump pulse. The ISRS pump and probe beams are offset vertically prior to the pellicle beamsplitter, with the iris after the sample used to block the transmitted ISRS pump.

3.5

Conclusions

THz spectroscopy, whether using a low- or high-power source, requires spectrometer design which differs from its optical counterpart due to the long wavelength of THz radiation and the size and limited selection of suitable commercially available THz optics. In particular, tilted-pulse-front sources require handling optics to be tailored to the optical focusing elements employed in the generation setup itself, with THz sources that behave as either collimated or divergent possible depending on the number of lenses used in the tilted-pulse-front imaging scheme. Taking all of these considerations into account,

a unified nonlinear THz spectrometer has been constructed that is capable of performing a diverse array of measurements at very high THz field strengths. The approach described in this chapter was used for the majority of the measurements presented in subsequent chapters.

References

1. Nuss, M. C. & Orenstein, J. in *Millim. Submillim. Wave Spectrosc. Solids* (Gruner, G.) **74,** 7 (Springer-Verlag Berlin Heidelberg, 1998).

2. Walther, M., Fischer, B., Schall, M., Helm, H. & Jepsen, P. U. Far-infrared vibrational spectra of all-trans , 9- cis and 13- cis retinal measured by THz time-domain spectroscopy. *Chem. Phys. Lett.* **332,** 389 (2000).

3. Hakey, P. M., Allis, D. G., Ouellette, W. & Korter, T. M. Cryogenic terahertz spectrum of (+)-methamphetamine hydrochloride and assignment using solid-state density functional theory. *J. Phys. Chem. A* **113,** 5119 (2009).

4. Nahata, A., Weling, A. S. & Heinz, T. F. A wideband coherent terahertz spectroscopy system using optical rectification and electro-optic sampling. *Appl. Phys. Lett.* **69,** 2321 (1996).

5. Kunitski, M. *et al.* Optimization of single-cycle terahertz generation in $LiNbO_3$ for sub-50 femtosecond pump pulses. *Opt. Express* **21,** 6826 (2013).

6. Hirori, H., Doi, A., Blanchard, F. & Tanaka, K. Single-cycle terahertz pulses with amplitudes exceeding 1 MV/cm generated by optical rectification in $LiNbO_3$. *Appl. Phys. Lett.* **98,** 091106 (2011).

7. Saleh, B. E. A. & Teich, M. C. *Fundamentals of Photonics*. (John Wiley & Sons, Inc., 2007).

8. Jewariya, M., Nagai, M. & Tanaka, K. Ladder climbing on the anharmonic intermolecular potential in an amino acid microcrystal via an intense monocycle terahertz pulse. *Phys. Rev. Lett.* **105,** 203003 (2010).

9. Katayama, I. *et al.* Ferroelectric soft mode in a $SrTiO_3$ thin film impulsively driven to the anharmonic regime using intense picosecond terahertz pulses. *Phys. Rev. Lett.* **108,** 097401 (2012).

10. Hwang, H. Y. *et al.* Nonlinear THz conductivity dynamics in P-type CVD-grown graphene. *J. Phys. Chem. B* **117,** 15819 (2013).

11. Liu, M. *et al.* Terahertz-field-induced insulator-to-metal transition in vanadium dioxide metamaterial. *Nature* **487,** 345 (2012).

12. Fan, K. *et al.* Nonlinear terahertz metamaterials via field-enhanced carrier dynamics in GaAs. *Phys. Rev. Lett.* **110,** 217404 (2013).

13. Negre, C. F. A. *et al.* Efficiency of interfacial electron transfer from Zn-porphyrin dyes into TiO_2 correlated to the linker single molecule conductance. *J. Phys. Chem. C* **117,** 24462 (2013).

14. Zalkovskij, M. *et al.* Terahertz-induced Kerr effect in amorphous chalcogenide glasses. *Appl. Phys. Lett.* **103,** 221102 (2013).

15. Hoffmann, M. C., Brandt, N. C., Hwang, H. Y., Yeh, K.-L. & Nelson, K. A. Terahertz Kerr effect. *Appl. Phys. Lett.* **95,** 231105 (2009).

16. Miyamoto, T., Yada, H., Yamakawa, H. & Okamoto, H. Ultrafast modulation of polarization amplitude by terahertz fields in electronic-type organic ferroelectrics. *Nat. Commun.* **4,** 2586 (2013).

17. Hoffmann, M., Hebling, J., Hwang, H., Yeh, K.-L. & Nelson, K. Impact ionization in InSb probed by terahertz pump—terahertz probe spectroscopy. *Phys. Rev. B* **79,** 161201 (2009).

18. Hoffmann, M. C., Hebling, J., Hwang, H. Y., Yeh, K. & Nelson, K. A. THz-pump/THz-probe spectroscopy of semiconductors at high field strengths [Invited]. *J. Opt. Soc. Am. B* **26,** A29 (2009).

19. Grady, N. K. *et al.* Nonlinear high-temperature superconducting terahertz metamaterials. *New J. Phys.* **15,** 105016 (2013).

20. Ruhman, S., Joly, A. G. & Nelson, K. A. Coherent molecular vibrational motion observed in the time domain through impulsive stimulated Raman scattering. *IEEE J. Quantum Electron.* **24,** 460 (1988).

Chapter 4

Nonlinear Terahertz Responses of Two-and Three-Dimensional Metamaterials on Silicon

Initial forays into nonlinear THz spectroscopy have typically been made by exploring materials that show the greatest promise for large nonlinear responses under high-field THz excitation, including graphene[1], semiconductors with free electrons[2–4], and inorganic perovskites[5]. Responses in more commonplace materials have been more limited; however, nonlinear THz spectroscopy has been performed on such commonplace systems as simple molecular liquids[6]. In addition to the application of nonlinear THz spectroscopy to a broader range of systems, advances made in free-space THz field enhancement through the use of tailored metamaterial SRR structures, as detailed in Chapter 2, have allowed for higher-order nonlinear material responses to be observed, including THz-driven phase changes in vanadium dioxide and even THz-induced damage in the same material[7]. The ability for SRR enhancement to make possible the observation of new types of nonlinear responses has uses in the ongoing application of nonlinear THz spectroscopy to more commonplace systems, as it can also be used to drive nonlinear responses in materials previously lacking them, as was shown through the observation of impact ionization in semi-insulating gallium arsenide (SI-GaAs)[8].

This chapter describes the application of SRR-enabled field enhancement to high-resistivity (high-res) silicon, which has not previously been shown to give nonlinear responses at THz frequencies even under very strong THz excitation fields. Field enhancement through two-dimensional (2D) SRR arrays similar to those outlined in Chapter 2 is shown to result in THz-driven impact ionization, which is probed through both intensity-dependent THz pump transmission and time-resolved THz-pump/THz-probe spectroscopy. Moving to three-dimensional (3D) structures reveals that the THz magnetic field is also capable of driving nonlinear electronic responses in metamaterial structures. Furthermore, the nonlinear response of the 3D structures exhibits a position dependence, which may be attributed to selective capacitive gap ionization.

This work was performed in collaboration with Kebin Fan, Xiaoguang Zhao, and others in the research groups of Richard Averitt and Xin Zhang at the Boston University Photonics Center, where the simulation and sample fabrication work was performed.

4.1

Background

4.1.1

Nonlinear THz Spectroscopy Driven and Observed Using Metamaterials

The development of THz-frequency metamaterials over the past decade has resulted in the availability of SRR structures that may be tailored to material-specific uses[9]. As detailed in Chapter 2, SRR materials of this type are useful for nonlinear THz spectroscopy for two reasons, namely their ability to enhance incident THz fields (with enhancements calculated to be up to a factor of 10^4 in some cases[9]) and the ability of their LC resonance, which is extremely sensitive to conductivity changes within the

capacitive SRR gaps, to act as a delocalized probe for nonlinearities induced in the gap by the enhanced free space THz fields. This usefulness was first demonstrated experimentally on thin films of vanadium dioxide[7]. In that experiment, incident THz fields were enhanced by SRR structures, which had been deposited directly on the vanadium dioxide surface. The resulting enhanced THz excitation fields, which reached peak levels of well above 1 MV/cm, drove the initially insulating vanadium dioxide through its well-known insulator-to-metal phase transition. The resulting changes in conductivity in the micron-size gaps resulted in changes in the LC resonance absorption that were measured by time-delayed THz probe pulses. Thus the probe pulses could be used to monitor the phase transition even though very little of the THz probe light fell on the small regions in which the phase transition occurred. Later, this technique was extended to GaAS, in which impact ionization was seen in both doped and semi-insulating samples as a result of SRR-enhanced THz fields[10]. The SRR-enabled, SRR-observed impact ionization dynamics in Si-GaAs, a material in which no nonlinear THz response had been previously seen without SRR enhancement, forms the prototype for the experiments presented here involving 2D SRR arrays on high-resistivity silicon.

4.1.2

Three-Dimensional Metamaterial Structures

Four-sided planar SRR metamaterials were initially developed in an effort to simplify the coupling between metamaterial structures and free-space THz fields, as highly symmetric four-sided SRRs show no coupling to the magnetic field of an incident linearly-polarized THz pulse[9]. Continued use of metamaterials has seen the development of more complex structures, including those designed for precisely the opposite purpose, i.e. coupling to the magnetic field of the THz pulse without coupling to its electric field, which can be accomplished through the use of a 3D double split ring resonator (3D

DSRR) structure (Fig. 4.1). 3D DSRR arrays have been shown experimentally to have LC resonances which are nearly free of electric field coupling as a result of their inversion symmetry when the incident THz pulse is oriented such that its magnetic field is perpendicular to the plane of the structure[11], which is illustrated in Fig. 4.1 (b).

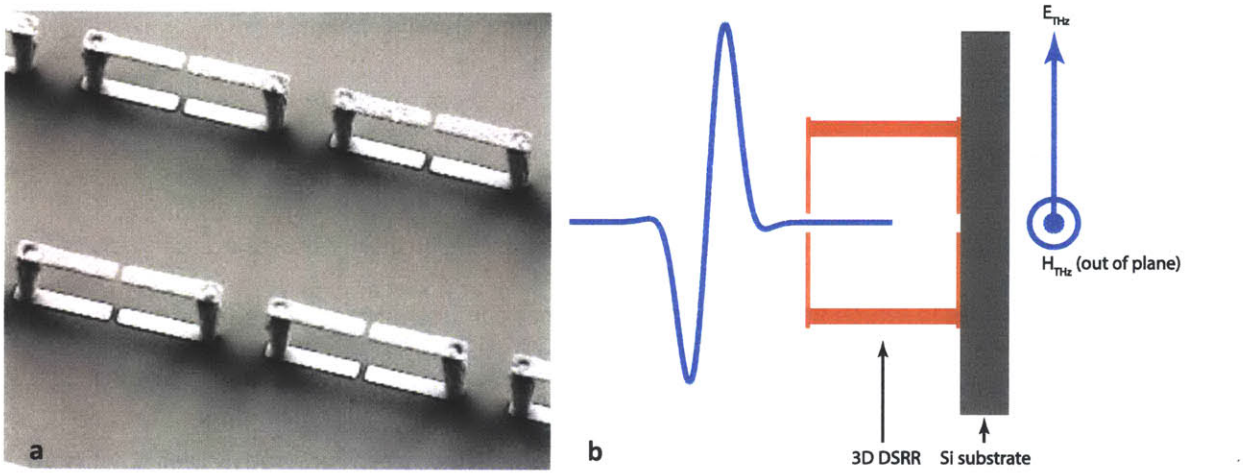

Figure 4.1. (a) SEM image of the 3D DSRR geometry (micrograph by K. Fan). **(b)** Schematic representation of the experimentally used orientation of the electric and magnetic fields of an incident THz pulse relative to the DSRR.

4.1.3

High-Field Behavior of Hi-Res Silicon

Silicon is perhaps the most studied material in the field of semiconductor physics owing to its ubiquity in modern electronics. Carrier electron transport in silicon becomes significantly nonlinear at applied electric fields of approximately 10 kV/cm and above due to several factors, beginning with nonlinear drift velocity behavior due to increased inelastic carrier scattering at high carrier energies[12]. At sufficiently high applied electric fields, carrier drift velocity saturation is encountered, with both experiments and Monte Carlo simulations indicating that this occurs at field values of approximately 100

kV/cm[13,14]. Impact ionization is also expected for applied fields of this magnitude. In this process, carriers are accelerated to energies greater than the bandgap by the applied field, and can lose energy through promotion of valence electrons to the conduction band. The threshold for impact ionization under DC fields in silicon is reported to be 200 kV/cm[15]. Finally, Zener tunneling (direct liberation of valence electrons by the applied field) is possible, but the reported DC field threshold for this effect, which is 1 MV/cm, is nearly an order of magnitude higher than the field threshold for impact ionization[15]. As a result, impact ionization is expected to be the dominant high-field response of silicon for fields on the order of 200 kV/cm and higher.

To date, nonlinear THz signal has been observed in n-type silicon[4] but not in hi-res samples, as the carrier density (1×10^{10} cm^{-3})[16] is simply too low for a response to be seen. Indeed, hi-res silicon is frequently encountered in THz measurements (including some nonlinear THz measurements[1]) not as a sample but instead as a sample substrate or THz window due to its essentially flat dispersion and extremely low absorption in the THz frequency range[17]. As a result, obtaining a nonlinear THz signal as the result of metamaterial application lends significant support for the use of engineered structures to enable new nonlinear THz science.

4.2

Experimental Apparatus

Intensity-dependent THz transmission and THz-pump/THz-probe data were obtained using the collinear THz-pump/THz-probe instrument described in Chapter 3, with wiregrid polarizers being used for both types of measurements, as sample damage was an issue at the highest THz field strengths capable of being produced by the instrument. Peak fields were measured to be in excess of 730 kV/cm through EOS detection. Some measurements were also taken on the older iteration of this instrument,

which was described in Chapter 3 and utilized 2 inch (50 mm) diameter OAP reflectors with longer EFLs. In this case, the maximum field obtained was approximately 375 kV/cm.

4.3

Sample Description

Both 2D SRR and 3D DSRR arrays were fabricated on hi-res silicon substrates. The 2D SRR samples were fabricated from gold using standard photolithographic techniques[18], and measured 36 μm in side length with 1 μm antenna gaps (Fig. 4.2 (a)). The enhancement factor for the peak electric field in the time domain, which was obtained through simulation, was approximately 3.2. The 3D DSRR samples were fabricated from copper using multilayer electroplating in combination with photolithography techniques[11,19], and yielded 3D DSRR structures measuring 34 μm in height and 85 μm in width, with 2 μm gaps (Fig. 4.2 (b)). For clarity, the gap in contact with the silicon substrate will be referred to as the "bottom gap", and the other gap, which is freestanding in air, will be referred to as the "top gap" hereafter. Despite the absence of coupling of the LC resonance to the THz electric field in these samples, enhanced electric fields are still expected in the capacitive gaps as a result of currents driven around the structure by the THz magnetic field. In the samples used here, the magnetic-field-induced peak electric field in the bottom gap is expected to be enhanced relative to the electric field of the THz pulse by a factor of 8. For the top gap, enhancement by a factor of 40 is expected. For both samples, an unpatterned portion of the wafer used as the sample substrate was kept as a spectroscopic reference for all THz spectra.

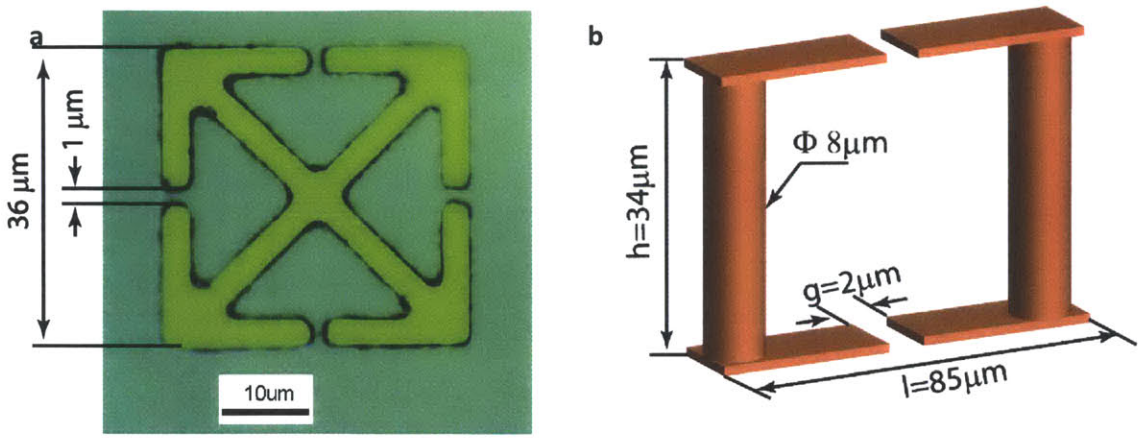

Figure 4.2. (a) Optical microscope image of 2D SRR array on hi-res Si wafer, with length and gap spacing annotated. **(b)** Schematic drawing of 3D DSRR with dimensions annotated (K. Fan).

4.4

Nonlinear THz Spectroscopy of 2D SRR Arrays on Hi-Res Silicon

Transmission spectra of the 2D SRR samples on hi-res silicon taken at varying THz field strengths (Fig. 4.3) exhibit an immediately apparent dependence on incident THz field strength. As the incident field is varied from 30 to 280 kV/cm (96 to 900 kV/cm in-gap), the LC resonance exhibits a decrease in absorption in addition to broadening and shifting to higher frequencies. When field strengths are further increased, this trend continues until fields exceed 500 kV/cm (1.6 MV/cm in-gap). At this point, the LC resonance exhibits a dramatic shift to higher frequencies and an increase in absorption (Fig. 4.4). This field strength also resulted in damage to the Si substrate, which is seen spectroscopically through the inability to recover the original LC absorption magnitude when the THz pump field is returned to its original value of 21 kV/cm (67 kV/cm in-gap).

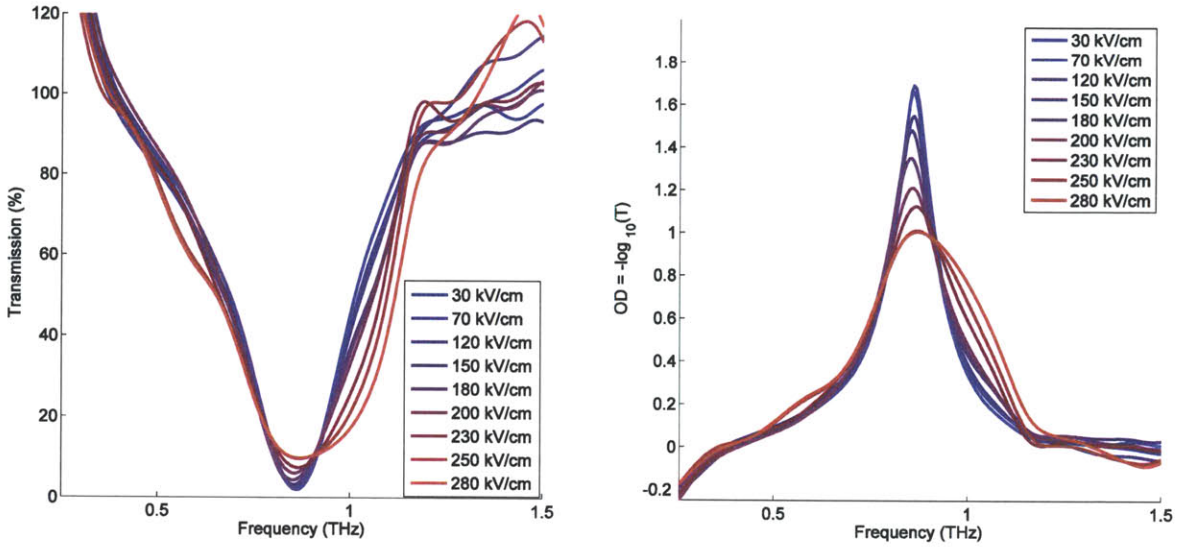

Figure 4.3. Intensity-dependent THz pump transmission of 2D SRR arrays on hi-res silicon plotted as transmission (left) and optical density (right).

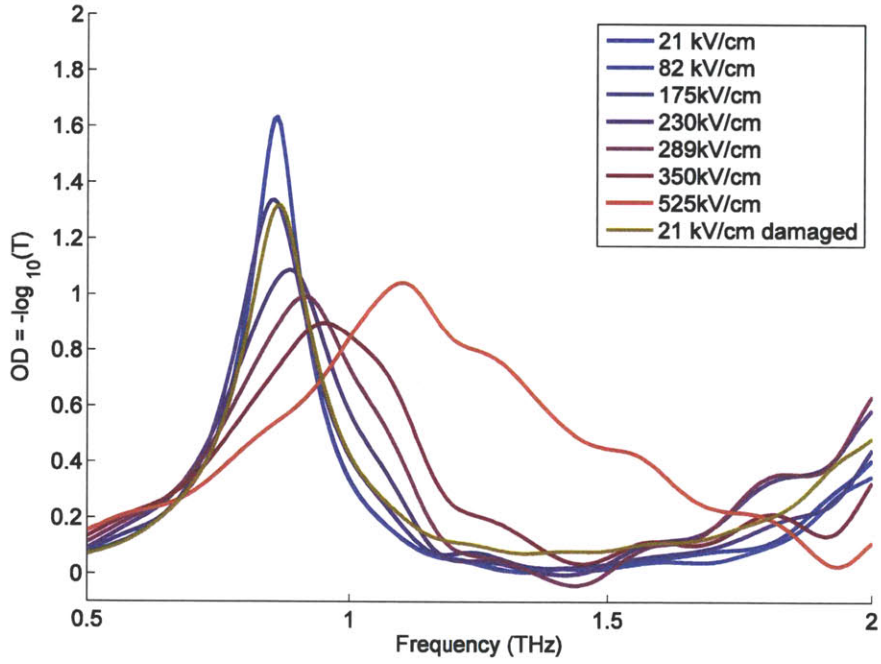

Figure 4.4. Intensity-dependent THz pump absorption of 2D SRR arrays on hi-res silicon at very high field strengths (shown as free-space field strengths), showing frequency shift at 525 kV/cm (1.7 MV/cm in-gap) as well as spectroscopic signature of THz-induced damage, which occurred at 525 kV/cm incident field strengths and is shown by comparison of the initial 21 kV/cm incident field (67 kV/cm in-gap) absorption trace (blue) to a spectrum taken at the same field level post-damage (brown), revealing incomplete absorption recovery.

The intensity-dependent THz transmission spectra give evidence of the presence of a THz-driven electronic nonlinearity, but do not reveal any dynamical information. For this purpose, THz-pump/THz-probe spectra were obtained using the collinear pump/probe instrument. In this case, THz pump fields were set to 175 kV/cm (560 kV/cm in-gap) to guard against sample damage. Full THz-pump/THz-probe spectra (Fig. 4.5) show that the bleaching and blueshifting observed at the LC resonance in the case of the intensity-dependent THz pump transmission spectra develop more fully over the course of the pump/probe delay trace. Comparison of transmission spectra taken before and after the pump/probe overlap shows an absorption decrease of roughly 50% at the LC resonance frequency combined with a blueshift and dramatic broadening (Fig. 4.6), which is consistent with the simulated spectra shown in Fig. 4.5. Examination and fitting of the time-dependent transmission of the unpumped LC resonance frequency (Fig. 4.7) shows that the bleaching effect grows in with a lifetime of 1.1 ps.

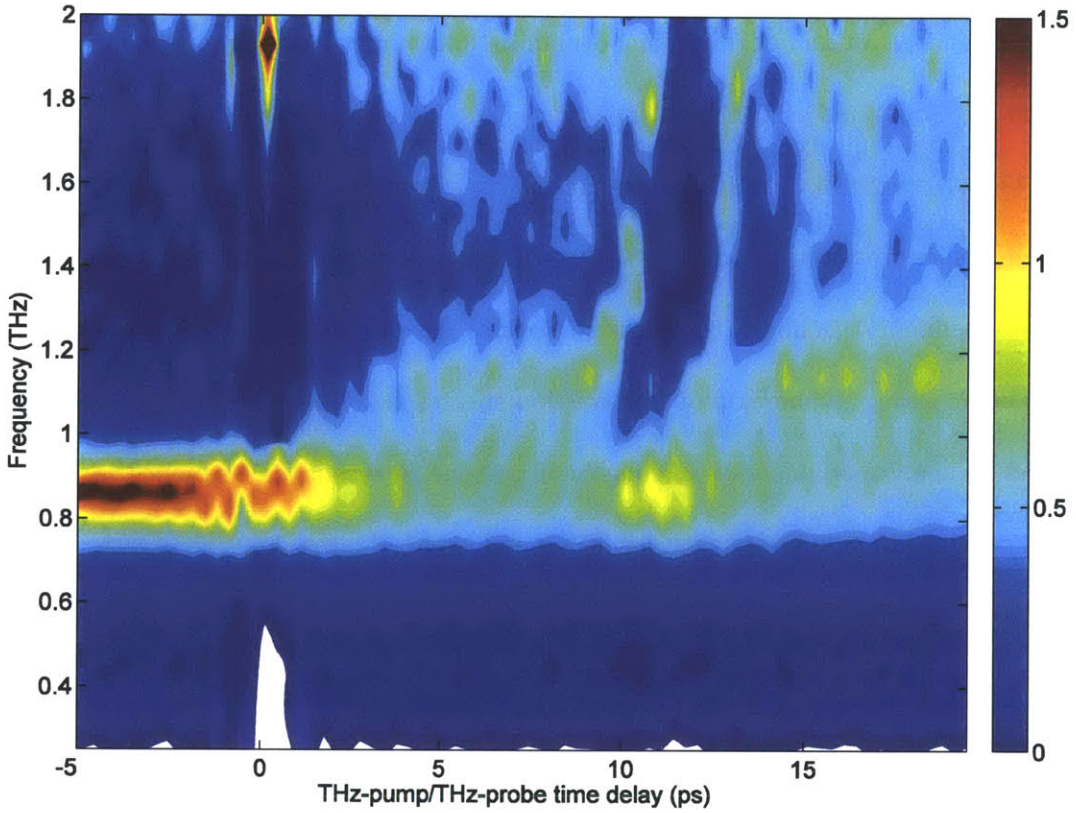

Figure 4.5. THz-pump/THz-probe absorption spectrum (in units of OD = $-\log_{10}(T)$) of 2D SRR arrays on hi-res silicon obtained using 175 kV/cm incident (560 kV/cm in-gap) THz pump field.

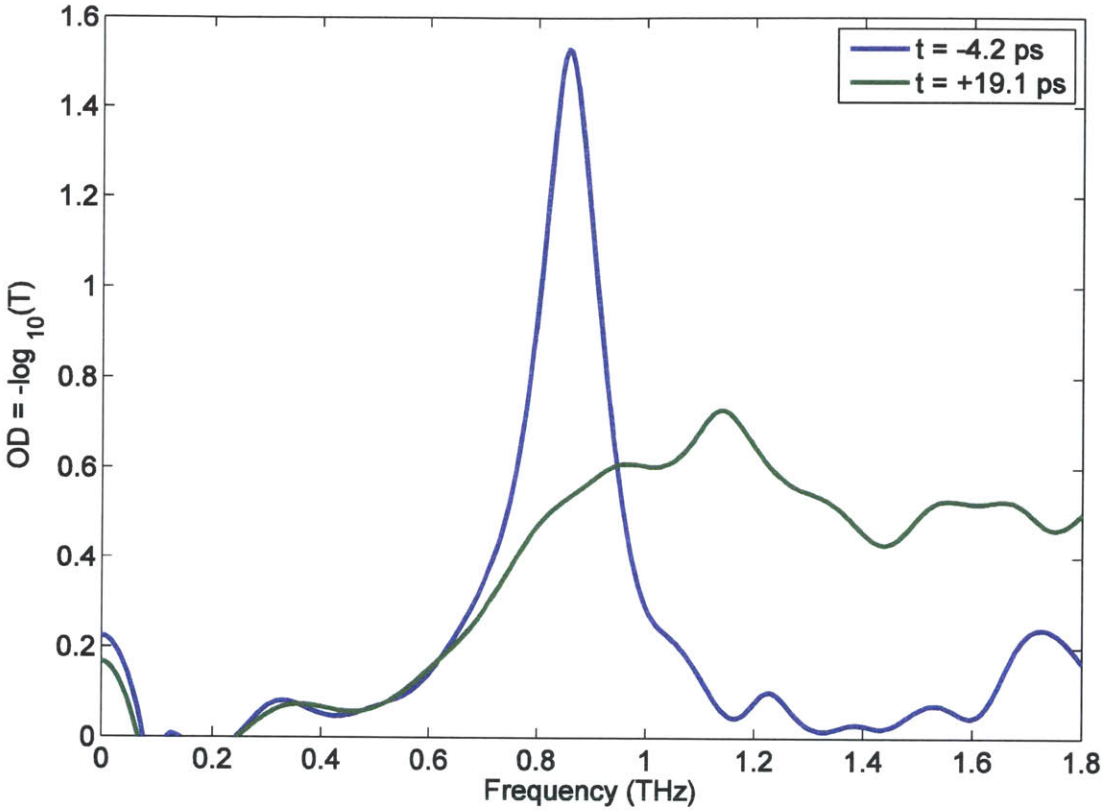

Figure 4.6. THz probe transmission spectra obtained for -4.2 and +19.1 ps THz-pump/THz-probe delay, showing broadening, blueshift, and decrease in LC resonance absorption.

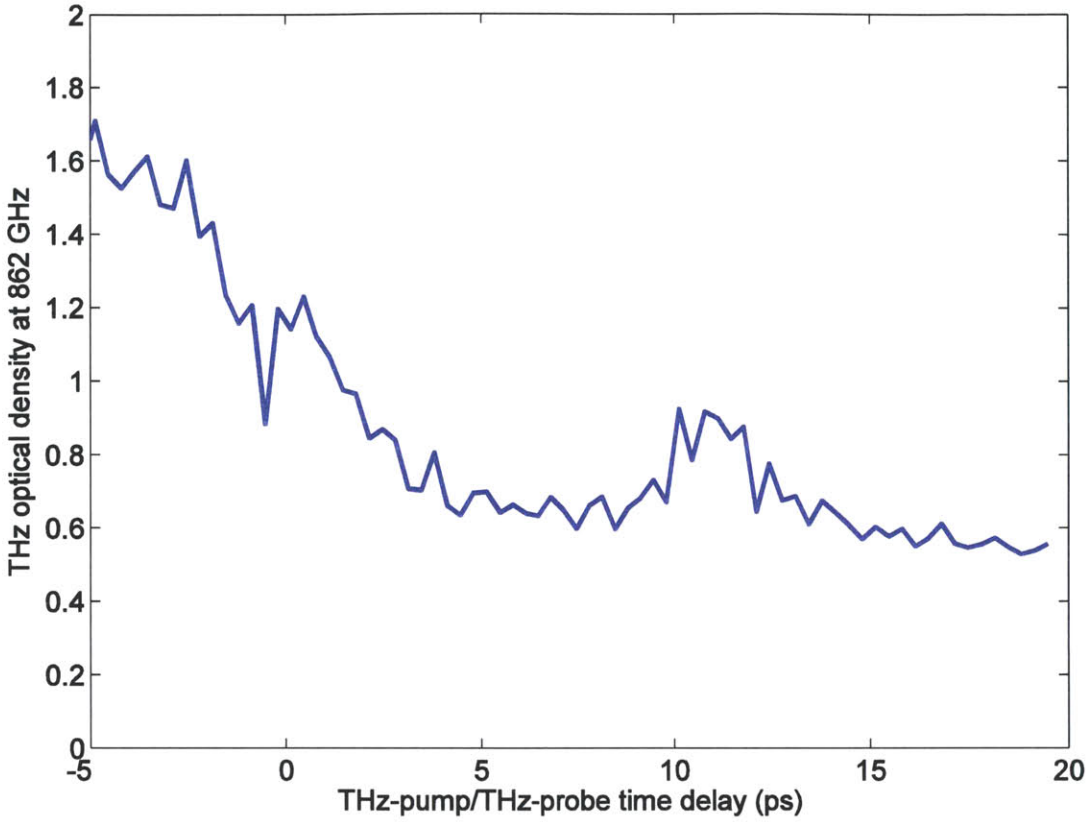

Figure 4.7. THz probe transmission at low-field LC resonance absorption maximum of 862 GHz, showing buildup of the THz-driven LC resonance bleach with a 1.1 ps lifetime.

4.5

Nonlinear THz Spectroscopy of 3D DSRR Arrays on Hi-Res Silicon

THz pump transmission spectra taken on the 3D DSRR sample on hi-res silicon showed a strong dependence on the incident THz field strength (Fig. 4.8), with the magnitude of the THz-driven modulation of the LC resonance being greater than in the case of the 2D SRR sample. As the incident THz field was varied from 30 to 280 kV/cm, the LC resonance absorption exhibited a strong decrease in intensity in addition to broadening and shifting to lower frequencies. The lack of coupling of the DSRR to the THz electric field necessarily implies that this effect is driven solely by the THz magnetic field;

however, as mentioned earlier, the observed effects are still due to electrical shorting of the antenna gaps (as will be further analyzed in the discussion in Section 4.6 below), as a result of the current driven around the DSRR structure by the THz magnetic field. In this case, the in-gap electric field for the bottom gap was varied from 240 kV/cm to 2.2 MV/cm, and the in-gap electric field for the top gap was varied from 1.2 MV/cm to 11.2 MV/cm.

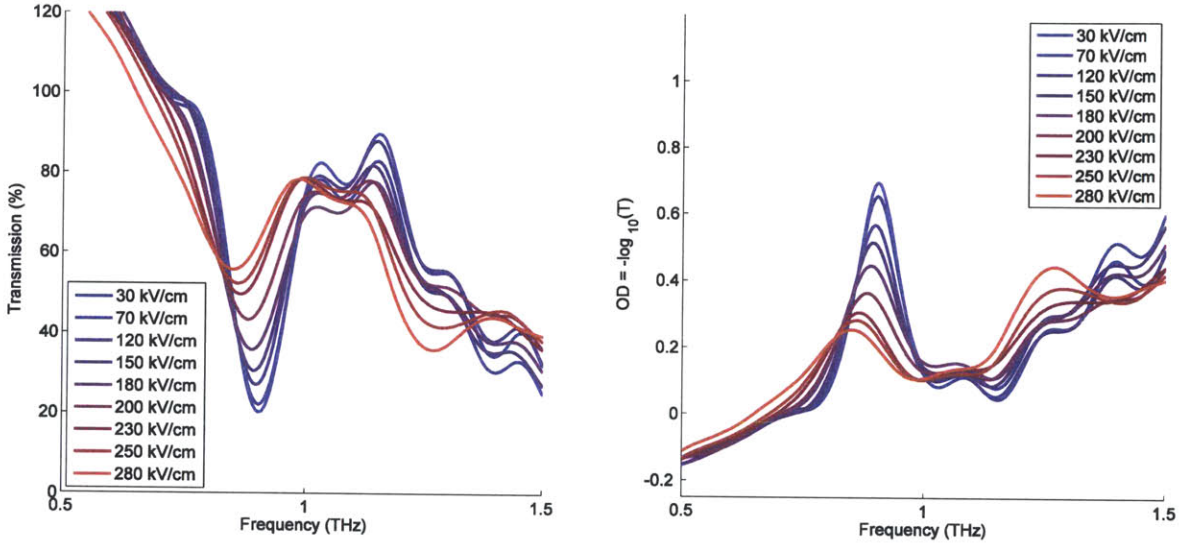

Figure 4.8. Intensity-dependent THz pump transmission of 3D DSRR structures on hi-res silicon plotted as transmission (left) and optical density (right).

4.6

Discussion

The nonlinear transmission results obtained for both types of metamaterial structures can be interpreted through simulations of the response of the LC resonance to THz fields for varying conditions of the in-gap substrate. Simulations were performed at the Boston University Photonics Center for both types of metamaterials used.

The observed THz-driven modulation of the LC absorption in the case of the 2D SRR arrays can be attributed to impact ionization, which was described in Section 4.1.3. The reported DC threshold for the impact ionization process is approximately 200 kV/cm[15], which is well below the expected values of the maximum in-gap THz fields used here, which were approximately 900 kV/cm. Furthermore, examination of Fig. 4.4 shows that increasing the incident field from 30 to 70 kV/cm (96 to 220 kV/cm in-gap) results a small degree of bleaching at the LC resonance, which is consistent with the published DC threshold value of 200 kV/cm for the impact ionization process.

Simulations of the 2D SRR THz transmission spectra for which the in-gap conductivity was varied from 100 to 2000 $cm^{-1}\Omega^{-1}$ replicated the observed transmission bleach at the LC resonance absorption, but were unable to reproduce the concomitant blueshifting of the resonance frequency with increasing applied field. Reproduction of both effects required simulations based on the Drude absorption model, in which not only the number of carrier electrons but also the carrier mobility was varied. Figure 4.9 displays simulated LC absorptions at various carrier concentrations and mobilities, which match the absorption decrease and blueshifting observed experimentally in the static case (shown in Figs. 4.3-4.4). The simulations shown in Fig. 4.9 also show good agreement with absorption spectra taken before and after the arrival of the THz pump in the THz-pump/THz-probe data (Fig. 4.6). Examination of the simulated transmission data shows that carrier concentrations between 10^{17} and 10^{18} cm^{-3}, which are between 7 and 8 orders of magnitude higher than the intrinsic carrier concentration in hi-res silicon[16], are required to generate the observed effects. The increase in the carrier concentration by 7 to 8 orders of magnitude is similar to previous measurements in semi-insulating GaAs, in which an increase of 10 orders of magnitude was observed[10].

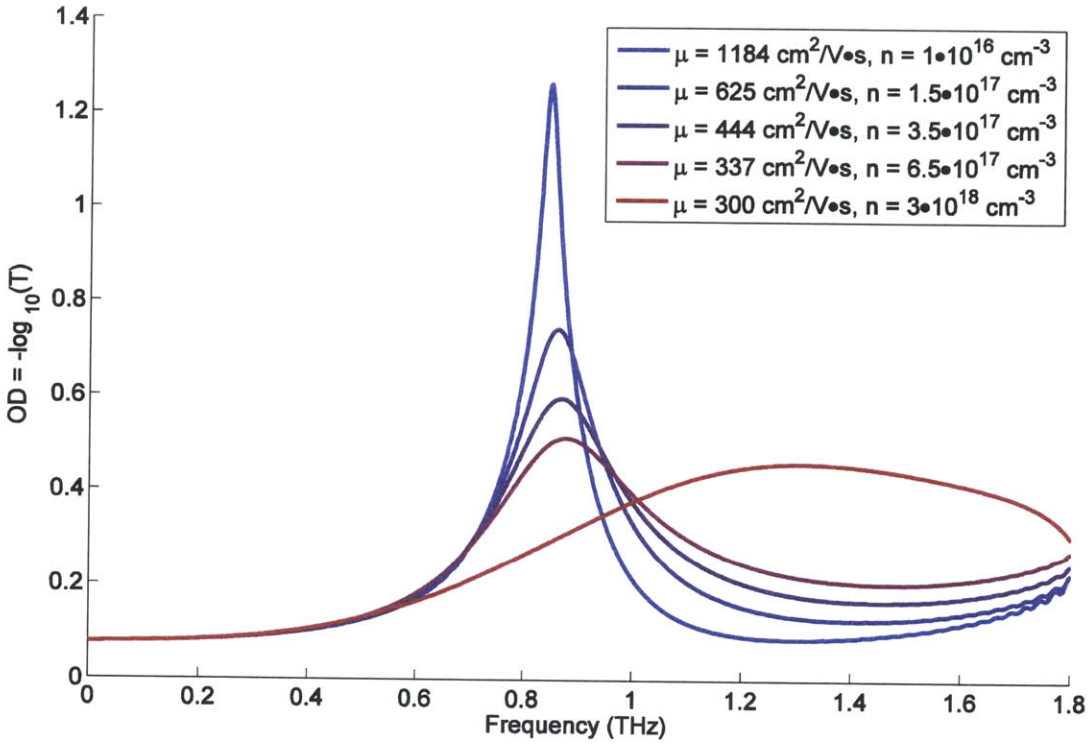

Figure 4.9. Simulated THz response of 2D SRR arrays on hi-res silicon calculated using a Drude model response, with values of mobility (μ) and carrier concentration (n) noted.

Interpretation of the effect observed in the 3D DSRR sample is somewhat more complicated when compared to the case of the 2D SRR arrays, as each structure contains two distinct capacitive gaps. Comparison to simulations of the conductivity varying in either gap independently or both gaps concurrently revealed that the observed redshift (see Fig. 4.8) is only obtained if the conductivity in only the bottom gap is varied, implying that some degree of silicon impact ionization occurs without any THz-driven conductivity change in the air within the top gap. This is consistent with the published 200 kV/cm DC threshold for silicon impact ionization, as the electric field created by the current driven by the THz magnetic field is expected to be well above this value for the bottom gap (in-gap fields varied from 240 kV/cm to 2.2 MV/cm in the bottom gap in the data shown in Fig. 4.8). At first glance, then, it is tempting

to conclude that silicon impact ionization occurs and air ionization does not for the in-gap field strengths applied in this case.

This conclusion, however, is incomplete. A more careful analysis of the observed nonlinear response reveals a strong dependence on the position of the sample in the propagation direction of the THz pump pulse. Comparison of intensity-dependent THz pump transmission spectra collected at varying positions in the THz focus show results that match simulations for all combinations of gap shorting (Fig. 4.10). Note that this implies the existence of THz-driven air ionization within the top gap, which is a subject that will be treated in depth in Chapter 5. As will be shown in Chapter 5, the maximum expected in-gap electric field strength for the top gap in the data shown in Fig. 4.10 (approximately 7 MV/cm for the maximum incident field of 175 kV/cm) is well above the electric field strengths necessary for air breakdown in a 2 μm copper gap at 1 THz frequencies, which can be estimated to be between 500 kV/cm and 5 MV/cm, depending on the surface quality of the DSRR surfaces near the gaps[20].

Examination of Fig. 4.10 shows that positioning the sample 1 mm behind the THz focus gives intensity dependent spectra that match simulations in which only the conductivity in the top gap is varied. Similarly, placing the sample 1 mm in front of the focus produces results that match simulations of the conductivity in only the bottom gap being varied, reproducing the initially-observed effect in Fig. 4.8. Finally, placing the sample at the focus yields results that match simulations for the conductivity being varied in both gaps. In this case, simulations show a stronger magnitude of the LC absorption bleach as compared to either gap being ionized individually, which is reproduced by experiment. The good match between experiment and theory in this case shows that the two distinct gap types may be ionized selectively as a function of position within the THz focus. This may be of use in future applications of nonlinear THz spectroscopy in which precise spatial control over the THz-driven response is required.

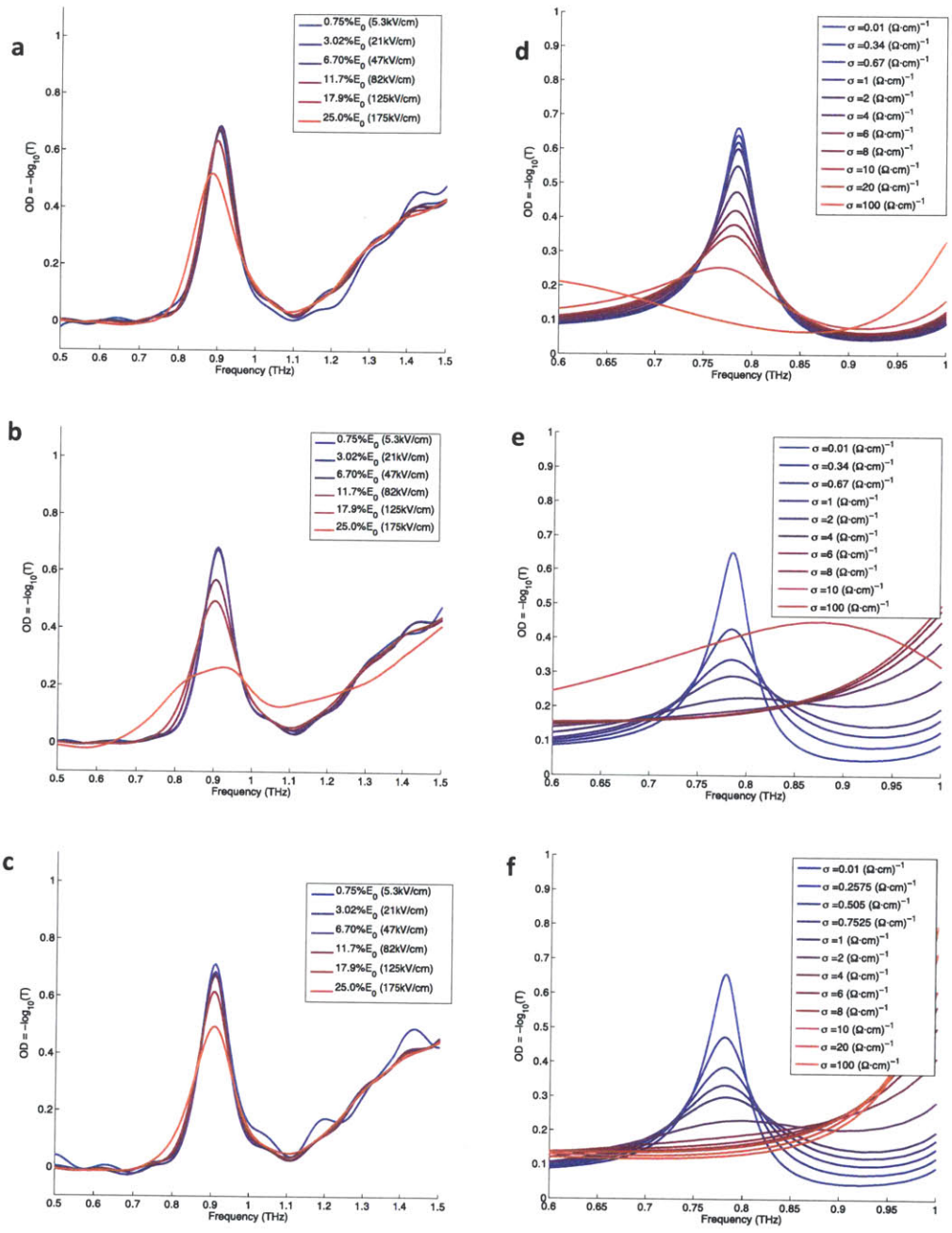

Figure 4.10. Experimental intensity-dependent THz pump transmission spectra for 3D DSRR arrays on hi-res silicon positioned 1 mm in front of the THz focus **(a)**, at THz focus **(b)**, and 1 mm behind the THz focus **(c)**, compared to simulated THz transmission for 3D DSRR structures for **(d)** bottom gap conductivity varying, **(e)** both gaps varying, and **(f)** top gap conductivity varying, showing qualitative agreement with corresponding experimental spectra.

4.7

Conclusions

The application of THz-enhancing SRR structures has been shown to be able to drive nonlinear THz interactions in hi-res silicon, which previously did not show any nonlinear response in the THz range. In arrays of 2D SRR structures, the LC resonance absorption is observed to blueshift, broaden, and decrease as incident THz fields are increased, consistent with a large increase in the in-gap carrier density due to impact ionization. THz-pump/THz-probe spectra show the time-dependent evolution of this effect, which appears with a lifetime of approximately 1.1 ps. Moving to more complicated 3D DSRR structures, for which THz electric field coupling to the LC resonance is not possible, shows the continued existence of a nonlinear interaction at high field strengths, therefore giving evidence that THz magnetic fields are also capable of driving electronic nonlinearities as a result of magnetic-field-driven currents in the DSRR structure. Furthermore, this effect shows a position dependence that is related to the selective shorting of either the top or bottom DSRR gap, giving promise to future applications of more precise control over THz-driven material interactions.

References

1. Hwang, H. Y. *et al.* Nonlinear THz conductivity dynamics in P-type CVD-grown graphene. *J. Phys. Chem. B* **117,** 15819 (2013).

2. Hoffmann, M., Hebling, J., Hwang, H., Yeh, K.-L. & Nelson, K. Impact ionization in InSb probed by terahertz pump—terahertz probe spectroscopy. *Phys. Rev. B* **79,** 161201 (2009).

3. Hoffmann, M. C., Hebling, J., Hwang, H. Y., Yeh, K. & Nelson, K. A. THz-pump/THz-probe spectroscopy of semiconductors at high field strengths [Invited]. *J. Opt. Soc. Am. B* **26,** A29 (2009).

4. Hebling, J., Hoffmann, M. C., Hwang, H. Y., Yeh, K.-L. & Nelson, K. A. Observation of nonequilibrium carrier distribution in Ge, Si, and GaAs by terahertz pump–terahertz probe measurements. *Phys. Rev. B* **81,** 035201 (2010).

5. Katayama, I. *et al.* Ferroelectric soft mode in a $SrTiO_3$ thin film impulsively driven to the anharmonic regime using intense picosecond terahertz pulses. *Phys. Rev. Lett.* **108,** 097401 (2012).

6. Hoffmann, M. C., Brandt, N. C., Hwang, H. Y., Yeh, K.-L. & Nelson, K. A. Terahertz Kerr effect. *Appl. Phys. Lett.* **95,** 231105 (2009).

7. Liu, M. *et al.* Terahertz-field-induced insulator-to-metal transition in vanadium dioxide metamaterial. *Nature* **487,** 345 (2012).

8. Fan, K. *et al.* Optically tunable terahertz metamaterials on highly flexible substrates. *IEEE Trans. Terahertz Sci. Technol.* **3,** 702 (2013).

9. Padilla, W. *et al.* Electrically resonant terahertz metamaterials: Theoretical and experimental investigations. *Phys. Rev. B* **75,** 041102 (2007).

10. Fan, K. *et al.* Nonlinear terahertz metamaterials via field-enhanced carrier dynamics in GaAs. *Phys. Rev. Lett.* **110,** 217404 (2013).

11. Fan, K., Strikwerda, A., Zhang, X. & Averitt, R. Three-dimensional broadband tunable terahertz metamaterials. *Phys. Rev. B* **87,** 161104 (2013).

12. Yu, P. Y. & Cardona, M. *Fundamentals of Semiconductors*. (Springer-Verlag Berlin Heidelberg, 2010).

13. Canali, C., Jacobini, C., Nava, F., Ottaviani, G. & Alberigi-Quaranta, A. Electron drift velocity in silicon. *Phys. Rev. B* **12,** 2265 (1975).

14. Kunikiyo, T. *et al.* A Monte Carlo simulation of anisotropic electron transport in silicon including full band structure and anisotropic impact-ionization model. *J. Appl. Phys.* **75,** 297 (1994).

15. Rodin, P., Ebert, U., Hundsdorfer, W. & Grekhov, I. Tunneling-assisted impact ionization fronts in semiconductors. *J. Appl. Phys.* **92,** 958 (2002).

16. Sze, S. M. & Kwok, K. N. *Physics of Semiconductor Devices*. (John Wiley & Sons, Inc., 2007).

17. Grischkowsky, D., Keiding, S., Exter, M. Van & Fattinger, C. Far-infrared time-domain spectroscopy with terahertz beams of dielectrics and semiconductors. *J. Opt. Soc. Am. B* **7,** 2006 (1990).

18. Tao, H. *et al.* Performance enhancement of terahertz metamaterials on ultrathin substrates for sensing applications. *Appl. Phys. Lett.* **97,** 261909 (2010).

19. Fan, K., Strikwerda, A. C., Tao, H., Averitt, R. D. & Zhang, X. Broadband tunable 3D metamaterials at terahertz frequencies. *2011 IEEE 24th Int. Conf. Micro Electro Mech. Syst.* 680 (2011). doi:10.1109/MEMSYS.2011.5734516

20. Radmilović-Radjenović, M. & Radjenović, B. An analytical relation describing the dramatic reduction of the breakdown voltage for the microgap devices. *EPL (Europhysics Lett.* **83,** 25001 (2008).

Chapter 5

Metamaterial-Enabled Terahertz-Driven Atmospheric Breakdown Phenomena in Microgaps

The previous chapter showcases the ability of metamaterial SRR structures to enhance free-space THz fields to levels necessary to drive nonlinear responses that were previously unattainable without enhancement. The range of systems to which metamaterial enhancement may be applied, however, is typically limited due to the need to deposit SRR structures directly to the surface of the sample of interest. Thus, initial studies have been limited to materials that may be found in robust wafer or thin film form, such as vanadium dioxide[1], gallium arsenide[2], and silicon (previous chapter). In an attempt to circumvent this requirement, samples were developed in which arrays of SRRs are situated on 400 nm freestanding silicon nitride membranes, with the area beneath each antenna gap having been removed through an etching process. This allows for the insertion of a sample of interest into the antenna gap for study by enhanced THz fields without the need for direct SRR deposition on the sample surface. In addition to allowing for enhanced THz fields to be applied to additional classes of samples, as will be explored further in Chapter 7, characterization of the responses of the metamaterials with empty

gaps to MV/cm THz fields yields valuable information on breakdown processes at μm lengthscales and THz frequencies, for which very little experimental data exist. This chapter describes these responses, which include THz-driven breakdown of air at atmospheric pressure as well as 8 mTorr pressure.

This work was performed in collaboration with Kebin Fan, Xiaoguang Zhao, and others in the research groups of Richard Averitt and Xin Zhang at the Boston University Photonics Center, where the simulation and sample fabrication work was performed.

5.1

Breakdown in Microgaps

5.1.1

DC Breakdown Phenomena

Electrical breakdown between electrodes spaced at macroscopic distances due to an applied DC field has been studied since the 19th century, and has been well described by Paschen's law, which states that the breakdown voltage will be a function of the reduced variable *pd*, where *p* is the gas pressure and *d* the distance between the electrodes[3]. Two processes are well established to contribute to breakdown at large gap spacing (typically taken to be 10 μm or more), namely electron impact ionization and secondary electron emission[4]. In electron impact ionization, free electrons in the electrode gap (theorized to result from processes such as cosmic rays) are accelerated by the applied field, and they gain enough energy to ionize atoms and molecules through collision processes. Secondary electron emission results from the close approach of these charged ionic species to the metal electrode surfaces. Modification of the metal potential by the strong local electric field surrounding the

ion results in additional electron emission, further contributing to the buildup of charged particles in the electrode gap.

Breakdown occurs when the buildup of charged particles due to electron impact ionization and secondary electron emission is larger than the loss of these particles to diffusion, recombination, and migration to the anode and cathode for electrons and ions, respectively[4]. This runaway buildup of charges, known as the Townsend avalanche criterion for breakdown, is described mathematically by the condition

$$\gamma_{se}\left(e^{\alpha d}-1\right)=1 \tag{5.1}$$

which includes the contributions of election impact ionization and secondary electron emission through the α and γ_{se} terms, respectively. The (unitless) secondary electron emission coefficient γ_{se} describes the probability of electron generation during an ion-cathode impact event, while α is known as Townsend's ionization coefficient and is given by

$$\alpha = Ap\exp\left(-\frac{Bpd}{V}\right) \tag{5.2}$$

where V is the applied potential and A and B are tabulated, gas-specific constants. Substituting Eq. 5.2 into Eq. 5.1 and solving for the applied potential V gives the commonly displayed formula for the breakdown voltage V_b given by Eq. 5.3[5].

$$V_b = \frac{Bpd}{\ln(pd)+\ln\left(\frac{A}{\ln(1/\gamma_{se}+1)}\right)} \tag{5.3}$$

Plotting V_b as a function of pd gives Paschen's curve for breakdown, which is shown in Fig. 5.1 for p = 760 Torr and γ_{se} = .01, which is a typical value for this parameter[4].

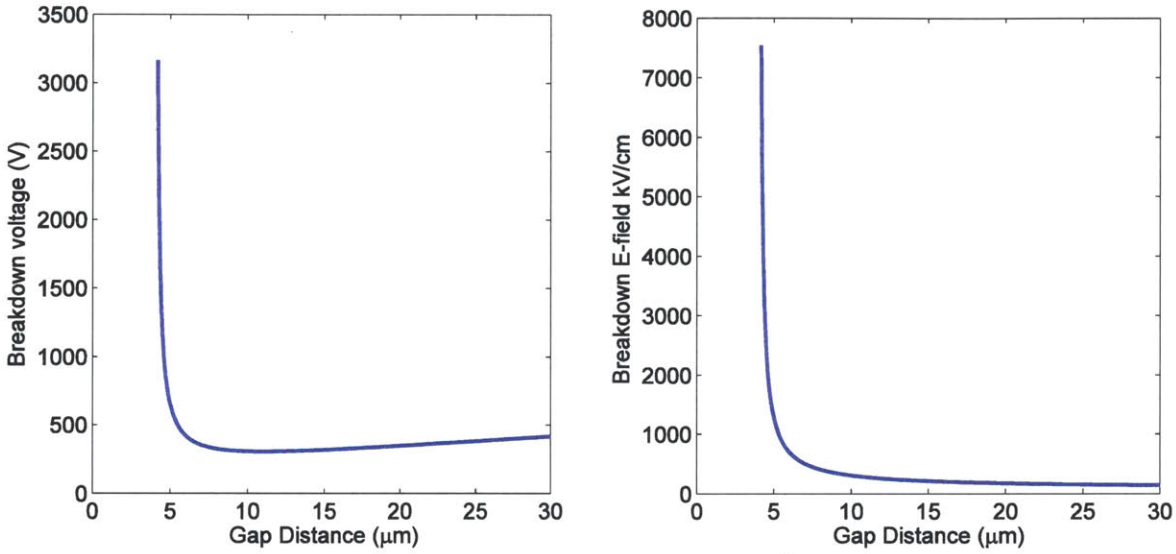

Figure 5.1. Paschen's curve showing breakdown threshold in air for p = 760 mTorr and γ_{se} = .01 given by voltage (left) and E-field (right).

Examination of Fig 5.1 immediately shows that Paschen's curve predicts that atmospheric breakdown is impossible for gaps smaller than approximately 4 μm, as the breakdown voltage diverges at this value of d at atmospheric pressure. The divergence arises due to the need for sufficient populations of ionizable species within the electrode gaps for the breakdown to occur, and at very small gap sizes, this condition is physically impossible to fulfill. Deviations from Paschen's law in this region have long been observed[6], and it is well established that a third process, field emission, is responsible for the observed breakdown in this region. Field emission, which is also responsible for electrical breakdown between electrodes in vacuum[5], describes the tunneling of electrons from the cathode surface in the presence of a strong electric field. The current density generated by the tunneling process is described by the Fowler-Nordheim equation[7], typically written as

$$j_{FN} = \frac{A_{FN}\beta^2 E^2}{\phi t^2(y)} \exp\left(-\frac{B_{FN}\varphi^{3/2} v(y)}{\beta E}\right) \tag{5.4}$$

where j_{FN} is the current density induced by the applied electric field E, A_{FN} and B_{FN} are constants, φ is the work function of the metal, and the terms $t^2(y)$ and $v(y)$ are described by

$$t^2(y) \approx 1.1 \tag{5.5}$$

$$v(y) \approx 0.95 - 1.03y^2 \tag{5.6}$$

$$y = 3.62 \times 10^4 \frac{\sqrt{E}}{\varphi} \tag{5.7}$$

and are corrections added later[8]. The enhancement factor β accounts for discrepancies between the predicted and experimentally observed values of j_{FN} for a given field, and is typically taken to correspond to the enhancement of the surface field by microscopic surface protrusions, with a reported range of 1.5 to 250 for various experiments[9,10].

Unification of the Townsend avalanche criterion (Eq. 5.1) with the added effects of field emission for small gaps results in the modified Paschen curve, for which various numerical and analytical solutions have been given[11–15]. For the purposes of this thesis, the simplified form for small gaps given by Radmilovic-Radjenovic et. al.[12] will suffice, which gives the breakdown field as

$$E_{DC} = \frac{D + Bp}{\ln(ApdK)} \tag{5.8}$$

where A and B are the Townsend criteria constants from Eq. 5.2, p is the pressure, d is the gap spacing, and K is left as a fitting parameter, typically on the order of 10^7 according to fits to experimental data[13]. The parameter D is an experimentally determined alternative Fowler-Nordheim constant and is given by

$$D = 6.85 \times 10^7 \frac{\varphi^{3/2}}{\beta} \tag{5.9}$$

where the enhancement factor β and work function φ have the same meaning as Eq. 5.4. Fig. 5.2 shows Eq. 5.8 plotted with along with Eq. 5.3 (solved for $E = V_b/d$).

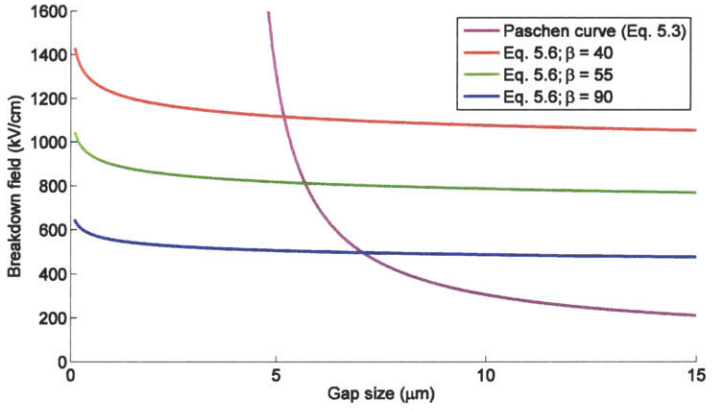

Figure 5.2. Paschen curve (Eq. 5.3) plotted with modified Paschen curves (Eq. 5.8) at 760 Torr in air for various values of β, with $\varphi = 5.1$ (corresponding to gold electrodes), $K = 10^7$ and $\gamma_{se} = .01$.

Finally, for very small gap sizes, experimental values for the breakdown threshold in air converge upon a constant value for the electric field, which has been reported to be on the order of 100 V/μm (1 MV/cm) by several sources[16–19]. This convergence is the consequence of the gap size approaching the value of the mean free path of an electron in air at atmospheric pressure and the ionization mean free path, which are typically reported as 400 nm and 1 μm, respectively[4,13]. In this limit, an emitted electron participates in very few ionization processes as it traverses the gap, resulting

in the observed nearly constant breakdown field. The range of gap sizes over which the breakdown field is expected to be constant has been the subject of some debate, with the maximum gap size for this regime being reported experimentally as 1.5[16] or 4[20] μm and theoretically as 1[21] or 3[13] μm. At this limit, due to the nearly unimpeded movement of field emitted electrons across the electrode gap, the breakdown process is assumed to be essentially identical to the breakdown process observed in vacuum[20], in which field emission of electrons is responsible for current flow between vacuum-isolated electrodes[5].

5.1.2

AC Breakdown Phenomena

The issue of moving from the DC breakdown phenomena described thus far to breakdown at AC frequencies is a problem which has been studied since the mid-20th century[22]. Though the underlying processes (electron impact ionization, secondary electron emission, and field emission) are identical, the overall breakdown mechanism is significantly more complex due to the effect of the time-varying applied electric field on the generation and loss of the charged particles necessary for avalanche breakdown within the electrode gap[4,23]. As the frequency of the applied electric field increases, the system eventually enters a regime in which the direction of the applied field reverses course before the electrons and ions can migrate across the gap. Consequently, the buildup of charged particles in the gap is significantly enhanced relative to DC breakdown, and the breakdown threshold is therefore lowered relative to the DC breakdown threshold[23]. The onset of this reduction in the breakdown potential is referred to as the critical frequency f_{cr}.

Recent reports of Monte Carlo simulations of breakdown phenomena at atmospheric pressure in microgaps indicate that f_{cr} for should lie between 10 and 500 GHz for gaps ranging from 15 to 0.5 μm

in argon with nickel electrodes (note that the samples used in the work presented in this chapter, described in the next section, consisted of gold electrodes in air, which should behave similarly based on the similar work functions for gold and nickel and the similar breakdown coefficients for air and argon)[23]. For $f < f_{cr}$, it is expected that the RMS breakdown voltage should be within 10% of the DC breakdown voltage, as breakdown phenomena should be qualitatively similar to DC breakdown because the field variation is sufficiently slow to allow for electron and ion migration to the electrodes before the field switches sign. Breakdown thresholds for $f > f_{cr}$ are again expected to be relatively constant as frequency is increased until the threshold again rises for very high frequencies, which are expected to be above 1 THz, which is a result of the decreased oscillatory amplitudes of very high frequency electric fields. Finally, the magnitude of the decrease of the breakdown threshold as the critical frequency is reached is dependent on the mechanism of gap breakdown, and is therefore directly dependent on the gap spacing d. For very small gaps, as mentioned previously, field emission is expected to be the dominant breakdown process, implying a smaller reliance on ionization processes and hence a smaller dependence of the breakdown threshold on the presence of ions in the gap. As a result, the relative change in the breakdown threshold at the critical frequency is greatly reduced for very small gaps, as the critical frequency behavior is directly related to the trapping of ions in the gap. Simulations show that the critical-frequency-dependent breakdown threshold decrease becomes very small for gaps of less than 2 μm at atmospheric pressure[23].

5.2

Sample Description

Two-dimensional metamaterial SRR structures, similar to those used in the previous chapter, were fabricated through a photolithographic process onto a 400 nm membrane of amorphous silicon

nitride (SiN_x), which was supported by a 500 μm thick silicon wafer[24]. Removal of the central portion of the silicon substrate through an etching process yielded a freestanding portion of the 400 nm thick SiN_x substrate supported by a silicon "frame", in which the central clear aperture of the silicon support measured 0.2 x 0.2 inches (5.1 x 5.1 mm). A schematic of this sample geometry is shown in Fig. 5.3 (a). To allow for insertion of arbitrary samples into the antenna gap, in which THz field enhancement occurs, the SiN_x membrane directly beneath each antenna gap was removed through reactive ion etching, leaving an open hole, which is illustrated in Fig. 5.3 (b) and (c). The circular form of the removed area, which measured roughly 10 μm in diameter, was chosen to prevent arcing in the substrate at high applied field strengths, which had been observed previously in samples where only the small area of substrate directly beneath the antenna gap had been etched. For added versatility, multiple gap sizes were fabricated, ranging from 1.5 to 3 μm. All measurements described here utilized gap sizes of either 1.5 or 3 μm, with LC resonance frequencies being 903 and 830 GHz, respectively. Note that these gap sizes fall directly into the range in which the breakdown criteria given in Eq. 5.5 are expected to transition to the constant breakdown field expected at very small gap spacing.

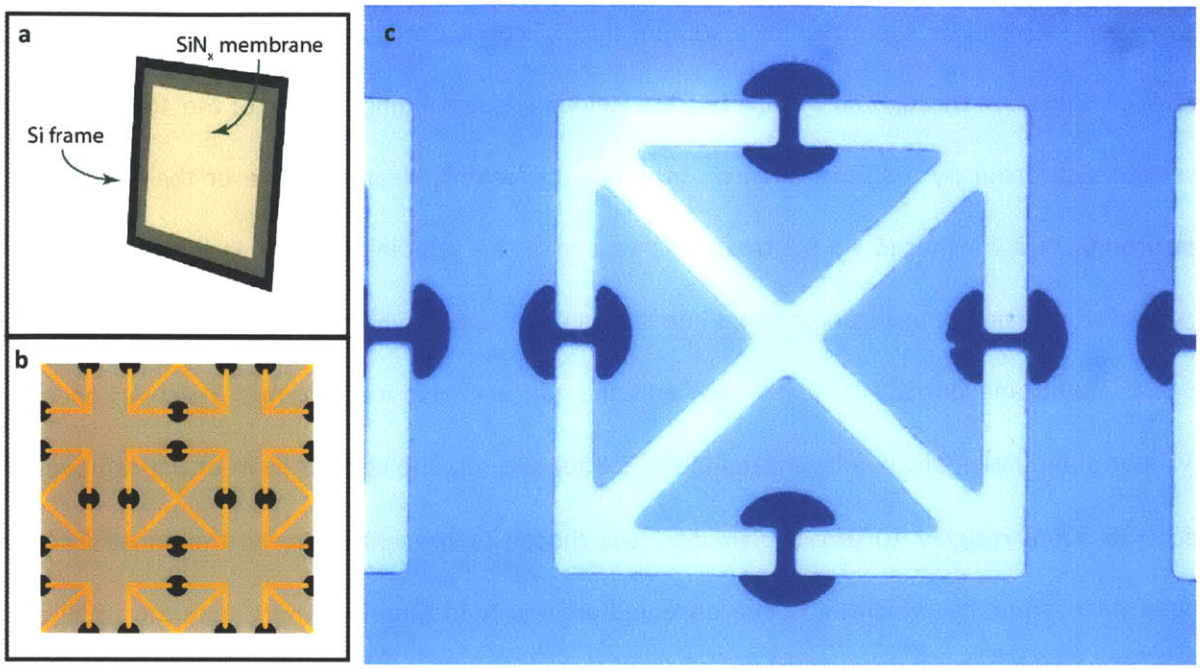

Figure 5.3. (a) Schematic illustration of SiN_x substrate geometry, showing silicon frame and SiN_x membrane. **(b)** Schematic illustration of SRR structures deposited on SiN_x, showing area of etched substrate beneath antenna gaps. **(c)** Optical microscope image of fabricated SiN_x SRRs, showing etched gap regions.

Full-wave simulations of the frequency-dependent THz field enhancement due to SRR coupling for structures with 1.5 μm gap spacing were carried out by the groups of Richard Averitt and Xin Zhang at the Boston University Photonics Center. The results reveal a peak enhancement factor of roughly 93 at 910 GHz (Fig. 5.4 (a)), which corresponds to the LC resonance of the SRR structure. Time-domain simulations reveal peak fields of approximately 11.6 MV/cm after SRR enhancement for a 440 kV/cm incident peak field, which is a factor of approximately 26.5 higher than the measured field strength of the unenhanced free-space THz pump pulse (Fig. 5.4 (b)).

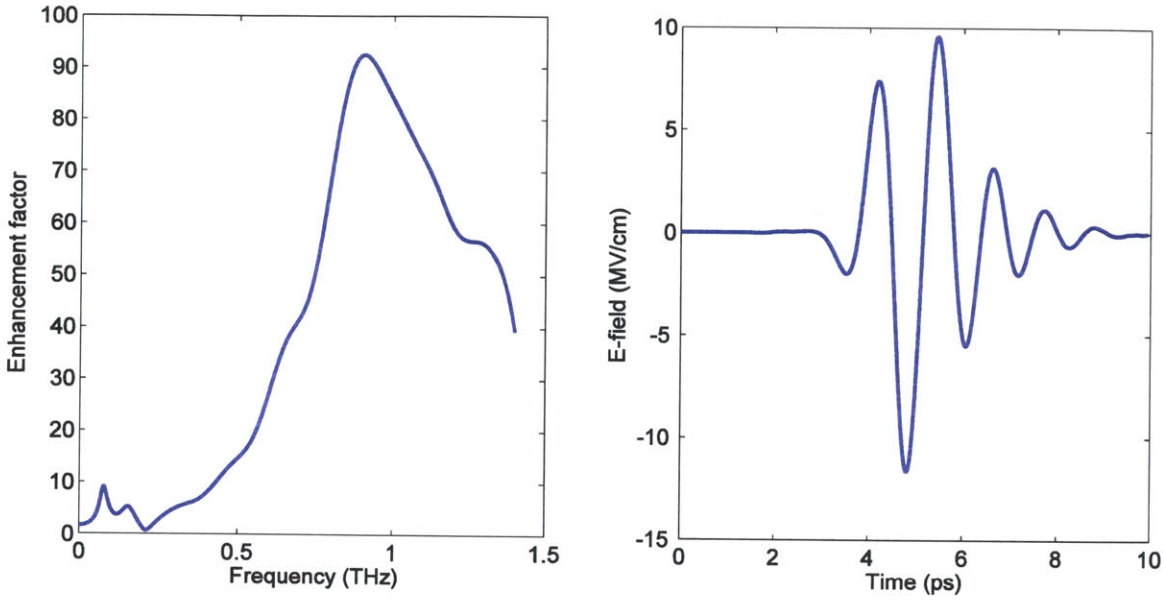

Figure 5.4. (a) Frequency-dependent free-space THz enhancement factor for SRRs with 1.5 μm gap spacing, showing maximum at LC resonance frequency of approximately 910 GHz. **(b)** Time-domain profile of THz pulse after SRR enhancement, calculated for a 440 kV/cm incident pulse, showing peak field strengths reaching 11.6 MV/cm, which corresponds to an enhancement factor of 26.5 for the peak in-gap electric field.

5.3

Experimental Apparatus

THz-pump/THz-probe measurements were performed using the collinear THz-pump/THz-probe instrument described in Chapter 3 (Fig. 5.5), with peak fields measured to be between 420 and 730 kV/cm (without enhancement) for the measurements presented here. Modification of the THz spectrometer to yield these field strengths, as described in previous chapters, requires the use of OAP focusing mirrors with very large numerical apertures. This enforces spatial constraints on the sample region of the spectrometer due to the large diameters and small focal lengths of the OAPs chosen. In the case of the instrument used here, the clear space between the second and third OAPs is only 1 inch (25.4 mm). As such, performing measurements at low pressure necessitated the design and construction

of a thin chamber that could be situated in the sample region of the spectrometer with enough space present to precisely position the sample in the THz propagation direction.

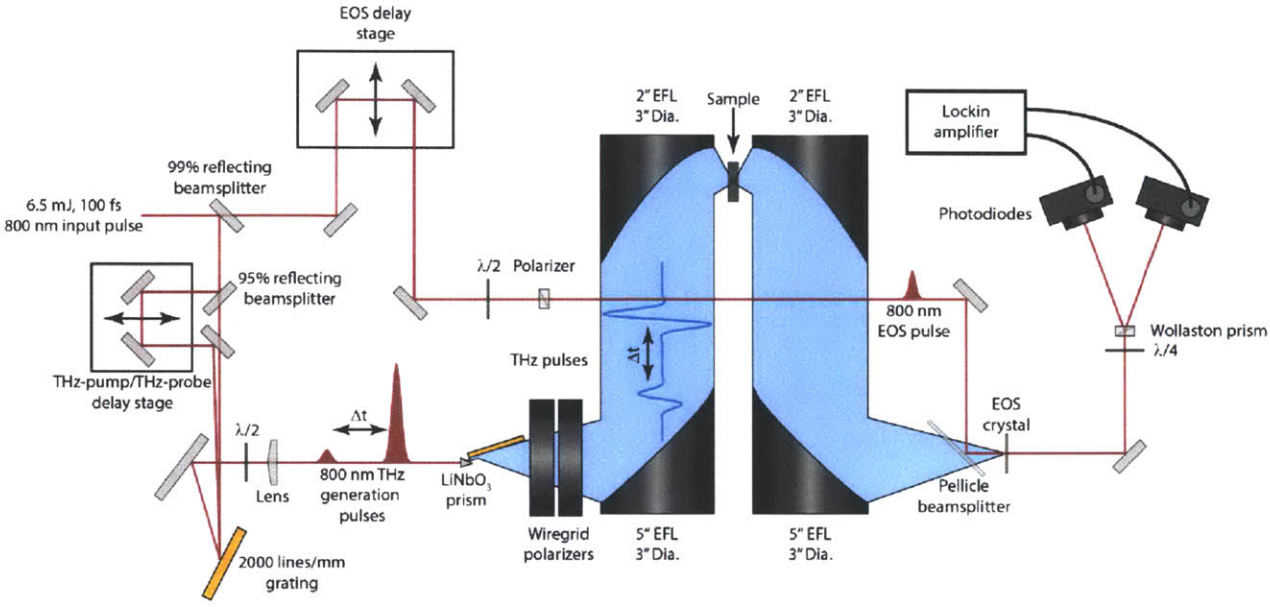

Figure 5.5. THz-pump/THz-probe instrument used for all measurements.

The chamber utilized for the measurements (Fig. 5.6) consists of a 0.5 inch (12.7 mm) wide body combined with 2.0 inch diameter fused silica windows of 1/16 inch thickness (50.8 and 1.59 mm, respectively), which are held in place by 1/8 inch (3.18 mm) thickness aluminum window holders. This yields an overall chamber thickness of 0.75 inches (19 mm), leaving ample room for precise positioning of the sample in the THz propagation direction. Fused silica was chosen as the window material despite its poor THz transmission at higher frequencies due to the commercial availability of windows with the desired minimum thickness yet sufficiently large area to avoid clipping the THz beam as it is focused by the high-numerical aperture OAP focusing optic. Testing of the chamber, once built, revealed a minimum attainable pressure of 3 mTorr. THz transmission spectra of the fused silica windows show moderate THz absorption above roughly 1 THz as well as reflective losses of approximately 31% at the peak electric field strength.

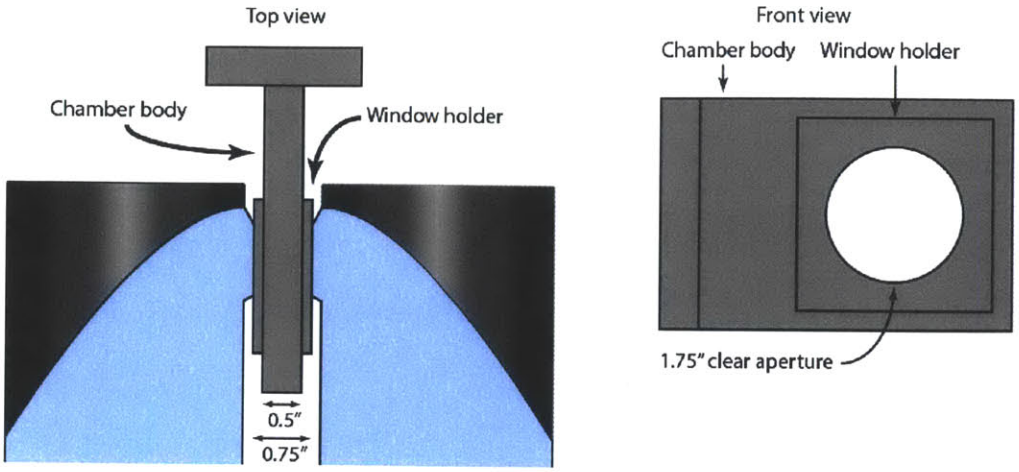

Figure 5.6. Schematic view of vacuum chamber used for low-pressure measurements from a top perspective (left) and front perspective (right).

5.4

THz-Pump/THZ-Probe Measurements at Atmospheric Pressure

Full frequency-dependent THz-pump/THz probe data (Fig. 5.7) taken on a sample with a gap spacing of 3 μm at atmospheric pressure with peak pump fields of 730 kV/cm in free space show unmistakable evidence of greatly increased in-gap conductivity, beginning shortly after the pump/probe temporal overlap range and persisting for the duration of the roughly 20 ps post-overlap scanning window. Beginning immediately after the 2.5 ps inaccessibility window around the overlap position, THz intensity transmission at the LC resonance shows a strong increase, from around 1% transmission pre-overlap to 30% intensity transmission post-overlap. Simultaneously, new resonances are observed post-overlap near 1.5 and 2.25 THz. Examination of the pump/probe traces at 830 GHz and 1.5 THz (Fig. 5.8) shows that the onset is essentially instantaneous on the timescale of the approximately 2.5 ps region of inaccessibility due to the overlap of the optical pulses in the $LiNbO_3$ THz generation prism. Both the

bleaching of the LC resonance and the observed higher frequency absorptions show essentially flat dynamics over the temporal window of the pump/probe scan, with no decay apparent.

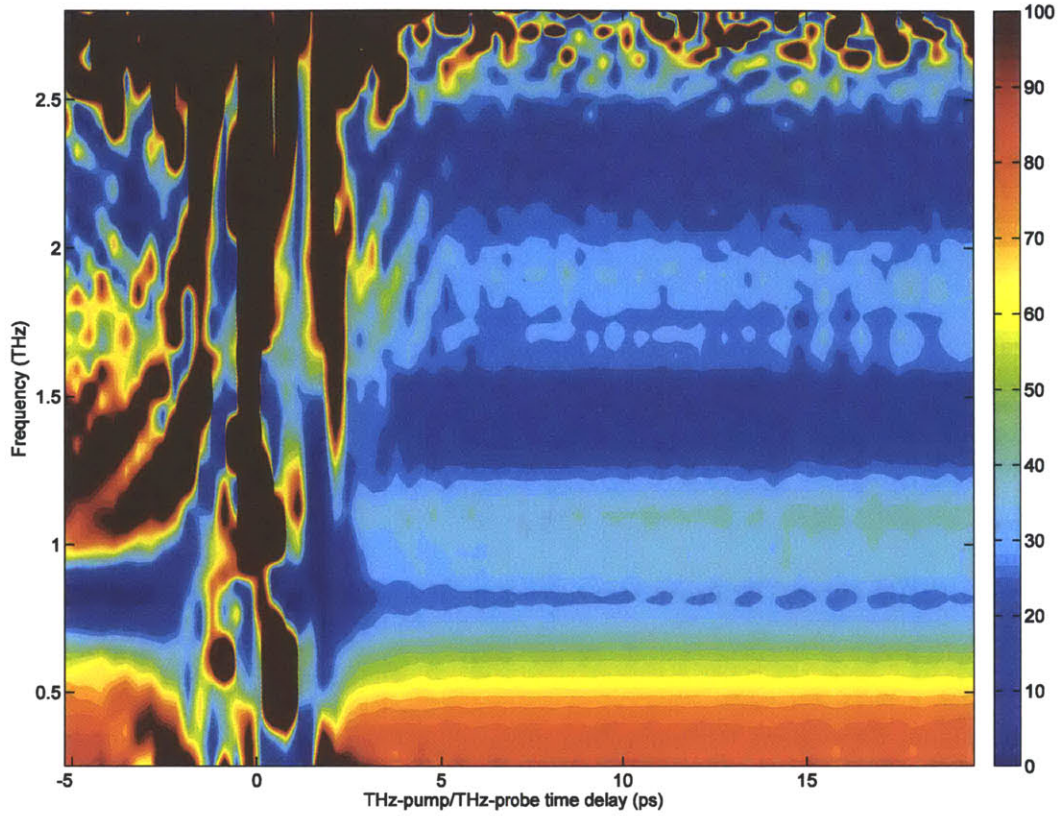

Figure 5.7. Percent THz probe intensity transmission as a function of THz-pump/THz-probe delay time for 3 μm gap SRRs at atmospheric pressure, showing bleaching of LC resonance at 830 GHz and redshift of higher order dipole resonances at 1.5 and 2.25 THz.

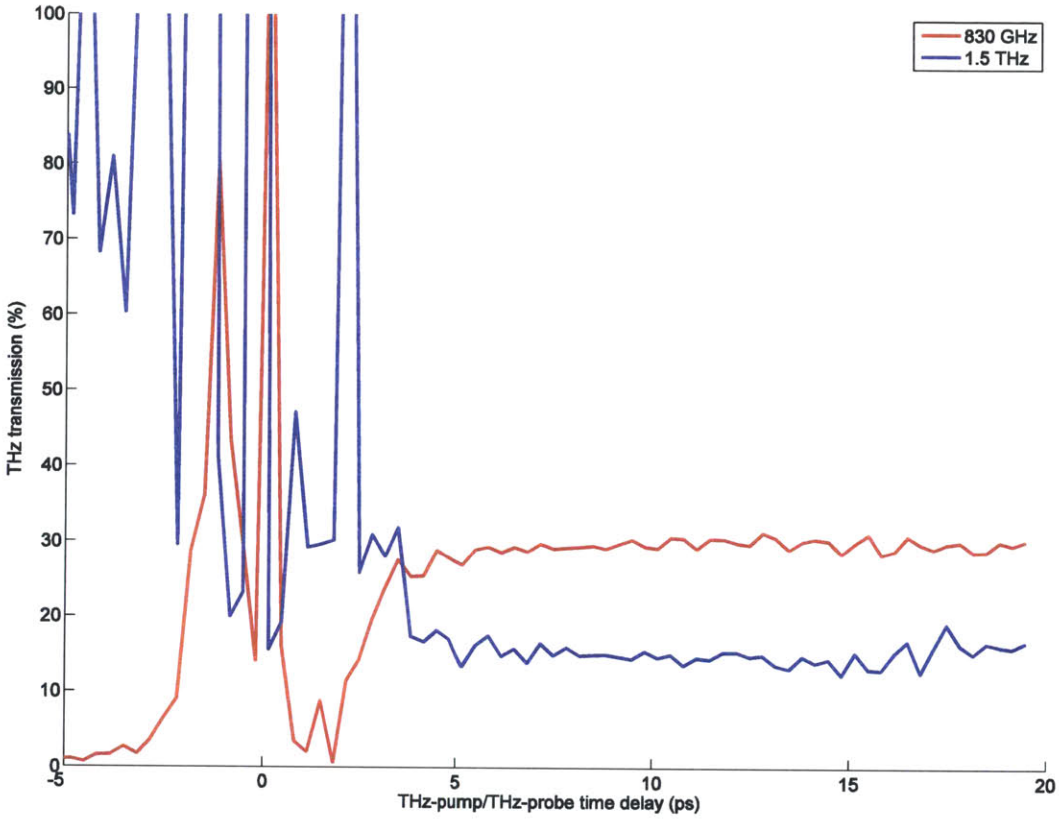

Figure 5.8. Time dependent THz probe transmission intensity as a function of THz-pump/THz-probe time delay at 830 GHz and 1.5 THz, corresponding to the LC resonance and post-overlap redshifted dipole modes, respectively, of SRRs with 3 μm gap spacing.

Examination of the sample after the approximately 18 hour THz-pump/THz-probe scans were taken revealed signs of field-induced damage to the corners of the SRR structures (Fig. 5.9), both for the measurements presented in Figs. 5.7 and 5.8 and when repeated with an identical sample and a peak pump field of 440 kV/cm. Furthermore, examination of the THz-pump/THz-probe data shows spectroscopic indications of damage (Fig. 5.10). Examination of Fig. 5.10 reveals that the THz probe absorption before the THz pump arrival time is unchanged, while the pump transmission 7.3 ps after the THz-pump/THz-probe overlap (t = +7.3 ps) is significantly broadened and bleached after the sample has

been intentionally damaged by THz irradiation at a 1 kHz repetition rate for 45 hours. Continuous examination of the THz probe transmission at this delay position during the 45 hour THz irradiation period showed that the spectroscopic damage signature continuously grew in magnitude with increasing irradiation time. Furthermore, examination of full THz-pump/THz-probe spectra after the damage period show dynamics which are unchanged from those seen in Fig. 5.8.

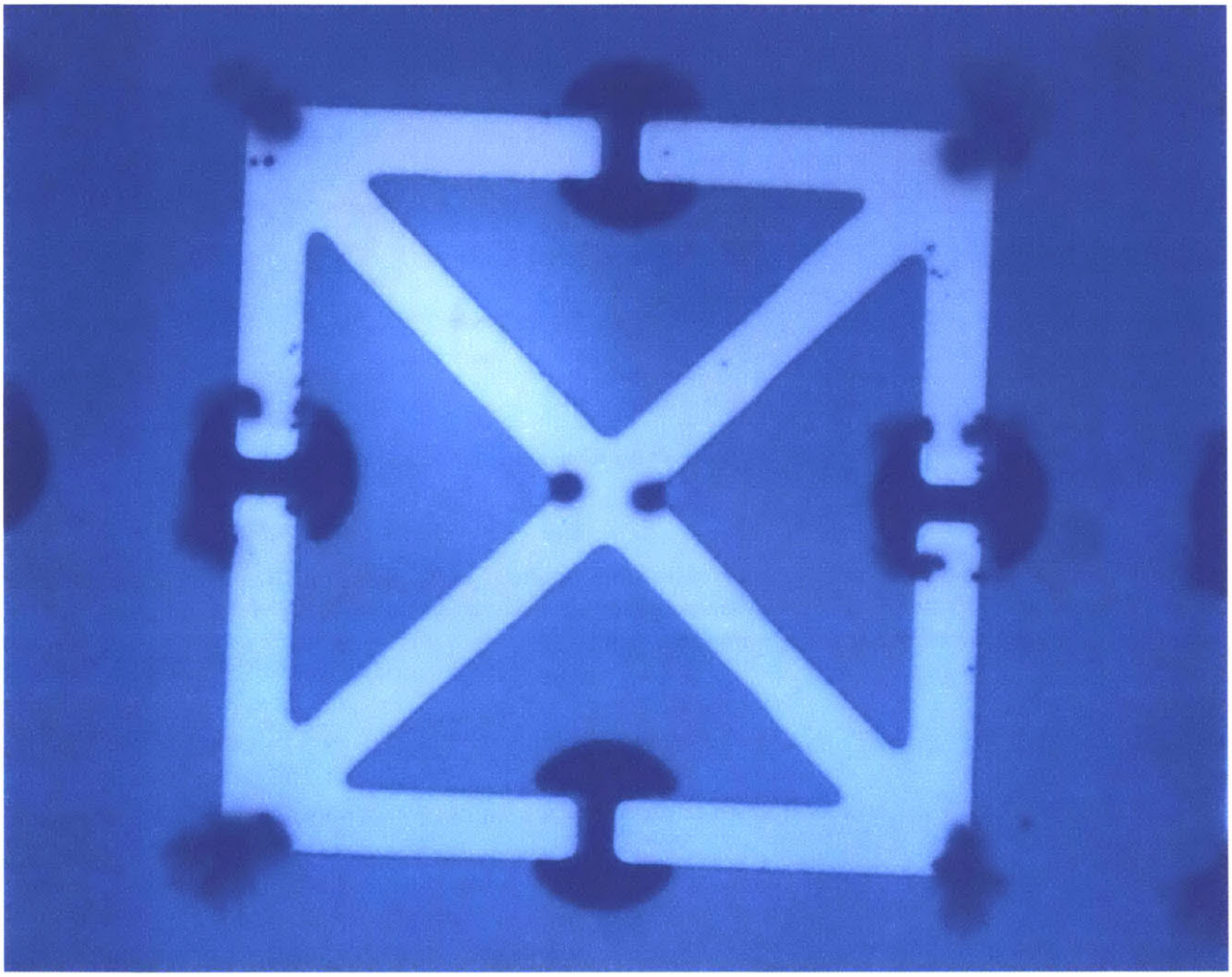

Figure 5.9. Optical microscope image of damage to SRR corners and gap region as a result of THz irradiation during the collection of THz-pump/THz-probe scans at 1 KHz repetition rate for approximately 18 hours.

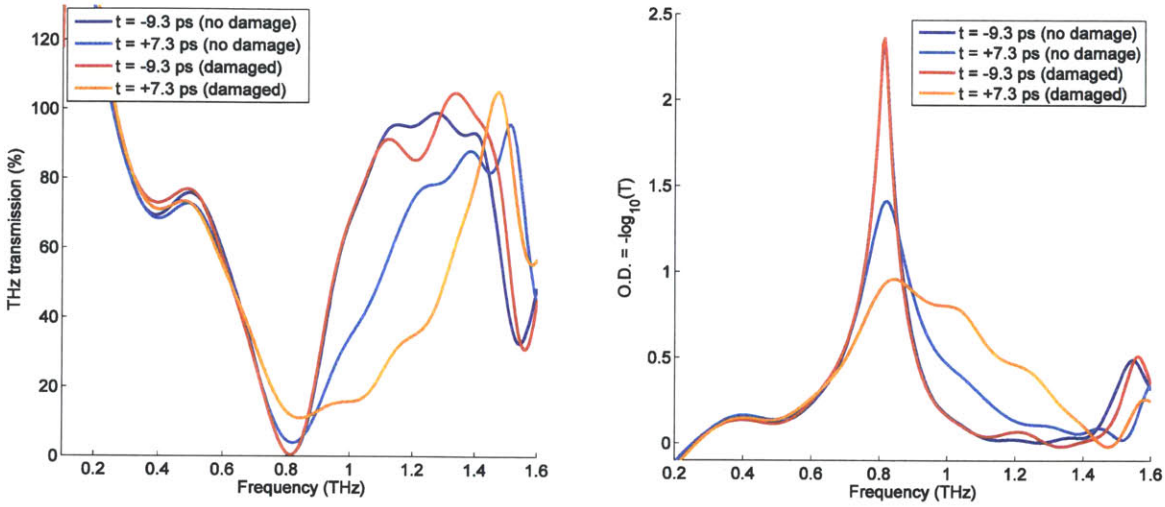

Figure 5.10. Spectroscopic signatures of damage to SRR structures as a result of THz irradiation, plotted as transmission (left) and optical density (right). Pre-overlap spectra at -9.3 ps time pump/probe delay show no change after irradiation. At +7.3 ps pump/probe delay, minimum transmission increases from 3.89% to 11.1% as a result of irradiation, with the corresponding peak frequency shifting from 820 GHz to 844 GHz.

When the gap spacing is reduced from 3 μm to 1.5 μm, the damage effect is again seen, but manifests itself more strongly, resulting in a full shift of the post-overlap LC resonance from its initial value of 903 GHz to a final value of 1.05 THz. The THz probe transmission for pre-overlap pump/probe delay times was not modified by the observed damage, consistent with the results obtained for the 3 μm gap spacing. THz-pump/THz-probe time slices taken at a damaged area of the sample are shown in Fig. 5.11 (a), showcasing the pump-induced shift in the LC resonance frequency, while identical time slices taken on undamaged areas of the sample (accomplished by rastering) are shown in Fig. 5.11 (b), for which no pump-induced shift is observed, in addition to the magnitude of the pump-induced bleaching being smaller than in the case of the damaged region for time delays immediately after the overlap. Note again that the pre-overlap LC resonance is identical in both cases. Examination of the post-overlap THz probe transmission revealed that the spectroscopic effects of damage grow in much more quickly as compared to case of the 3 μm gap spacing, with saturation of the effect reached after roughly 15 hours.

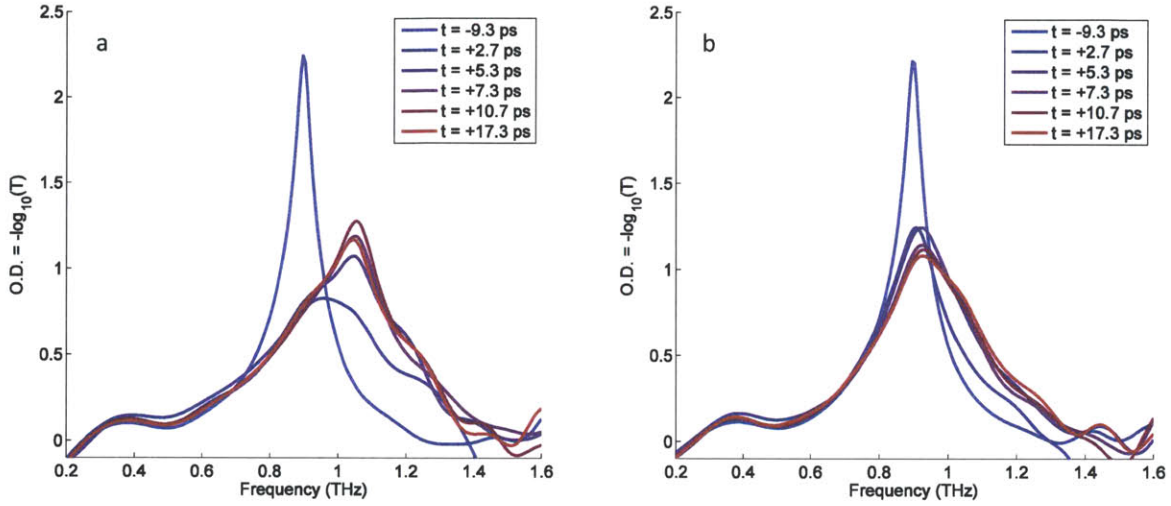

Figure 5.11. (a) THz probe transmission (shown as optical density) taken at varying pump-probe time delays on a previously damaged region of the 1.5 μm gap sample, showing LC resonance shift after THz pumping. **(b)** THz probe transmission taken at time delays identical to those in **(a)** on undamaged sample regions, showing no LC resonance shift and a smaller transient bleach magnitude.

To examine the threshold field level necessary for observable breakdown to occur, intensity-dependent THz probe transmission spectra were taken 7.6 ps after pump/probe overlap for the 1.5 μm gap sample. Examination of the magnitude of the LC resonance bleach relative to the pre-overlap pump transmission spectrum reveals that the threshold for the effect occurs at roughly 220 kV/cm (Fig. 5.12).

In summary, spectral responses and dynamics consistent with THz-driven air breakdown in the antenna gaps of the gold SRR structures is seen for both 1.5 and 3 μm gaps, with the threshold incident field strength necessary for the breakdown to occur being observed to be approximately 220 kV/cm. The breakdown process manifests itself as a transient bleaching of the SRR LC resonance after the arrival of the THz pump pulse, combined with the appearance of additional absorptions at higher frequencies. Furthermore, THz-induced damage to the corners and gaps of the SRR structures is observed after multiple hours of THz irradiation, which is observed spectroscopically as a modulation of the THz-

induced transient LC resonance bleach. A more complete discussion of the atmospheric-pressure results presented here will appear later, in Section 5.6.

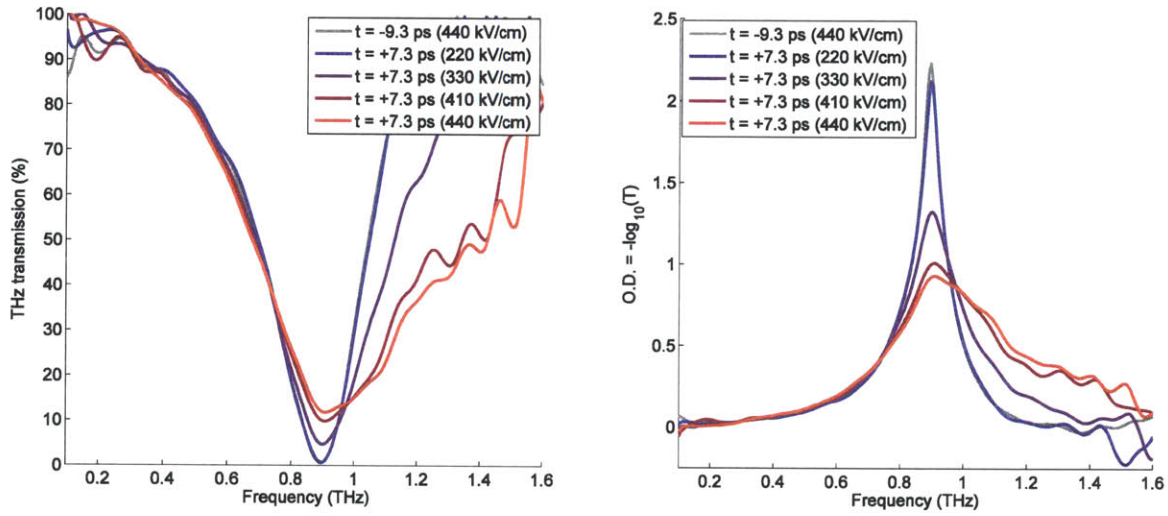

Figure 5.12. Field dependence of pump-induced THz probe transmission modulation at pump/probe delay of +7.3 ps, along with reference at -9.3 ps delay, shown as transmission (left) and optical density (right).

5.5

THz-Pump/THz-Probe Measurements at Low Pressure

To examine breakdown dynamics at low air pressure, THz-pump/THz-probe scans were performed at operating pressures of 8 mTorr and estimated incident peak fields (after transmission through the fused silica vacuum window preceding the sample) of 310 kV/cm (8.2 MV/cm in-gap) using the 1.5 μm gap sample from the previous section. Prior to low-pressure operation, THz-pump/THz-probe measurements were made at 760 Torr air pressure in the chamber and results similar to those discussed above were observed despite the lower peak fields as compared to the air measurements in the

previous section. To guard against THz-induced sample damage, THz probe transmission spectra were taken at new positions on the sample for selected pump/probe time delays.

THz probe transmission spectra taken at selected pump/probe delay times reveal long-lived dynamics at low pressure (Fig. 5.13). When compared to identical time slices taken at atmospheric pressure, the pump-induced bleach in the LC resonance shows no signs of a frequency shift at low pressure, as opposed to the moderate shift observed at atmospheric pressure with an undamaged sample. Comparison of time slices taken at low pressure to time slices taken at similar THz pump field strengths at atmospheric pressure shows that the magnitude of the transient LC resonance bleach is also greatly reduced at low pressure (Fig. 5.14). Finally, the timescale over which the transient LC resonance bleach is observed to persist is unchanged at low pressure when compared to atmospheric pressure over the 20 ps length of the THz-pump/THz-probe scan.

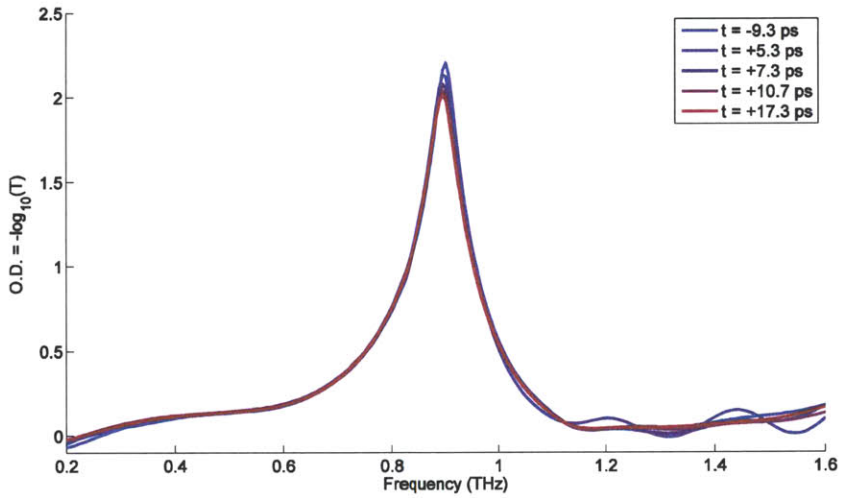

Figure 5.13. THz probe transmission at varying pump/probe delay positions at 8 mTorr pressure, plotted in units of optical density.

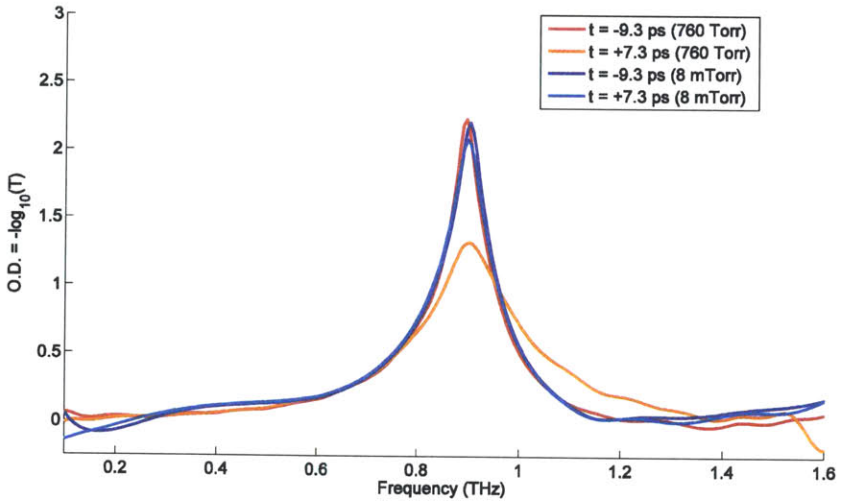

Figure 5.14. Comparison of THz probe transmission at identical time slices and field strength for atmospheric pressure (760 Torr) and low pressure (8 mTorr), showing greatly reduced magnitude for the transient LC resonance bleach at low pressure. The applied THz field strength prior to SRR enhancement was approximately 330 kV/cm and 310 kV/cm at atmospheric and low pressure, respectively.

Sample damage due to THz irradiation, as was observed at atmospheric pressure, was again observed at low pressure; however, at low pressure the damage is far more severe and results in permanent modification of the LC resonance absorption, as opposed to the modulation of the spectroscopic breakdown signature only as seen for damage at atmospheric pressure. Damage at the corners of the SRR structures was again observed, but was more severe in intensity (Fig 5.15 (a)). More dramatic damage was observed in the regions of the antenna gaps, with optical microscope images revealing the possible presence of material within the antenna gap (Fig 5.15 (b)). Furthermore, the gold SRR surface was observed to be discolored, having a red hue. Examination of the damaged gap region with a scanning electron microscope (SEM) reveals the diffusion of the gold electrodes into the antenna gap, effectively fusing it shut (Fig. 5.16), which explains the permanent spectroscopic damage signatures.

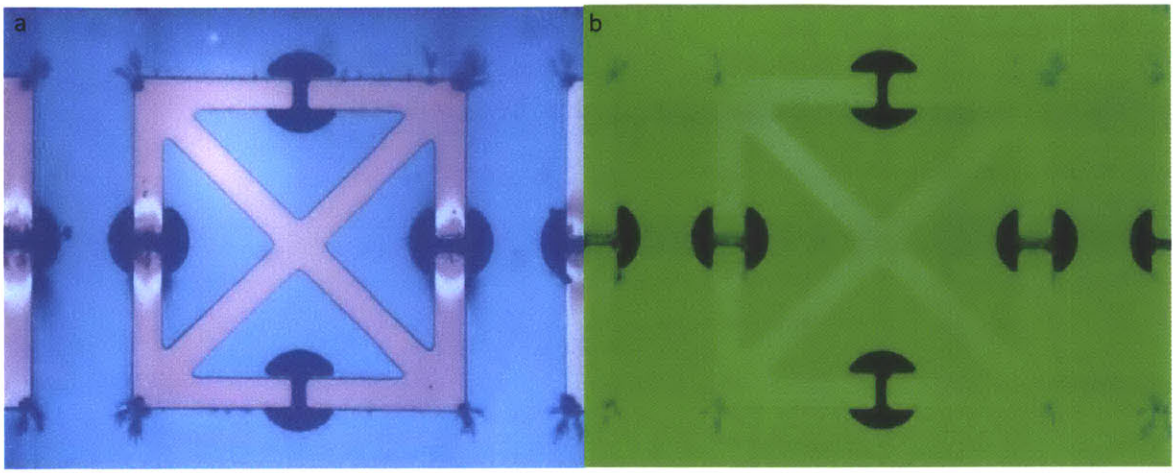

Figure 5.15. (a) Optical microscope image of THz-driven damage to SRR sample at low pressure, showing damage to corners of SRR structure and gap regions as well as discoloration of the gold surfaces. **(b)** SRR from **(a)** imaged with a different optical filter, showing some structure in the antenna gap.

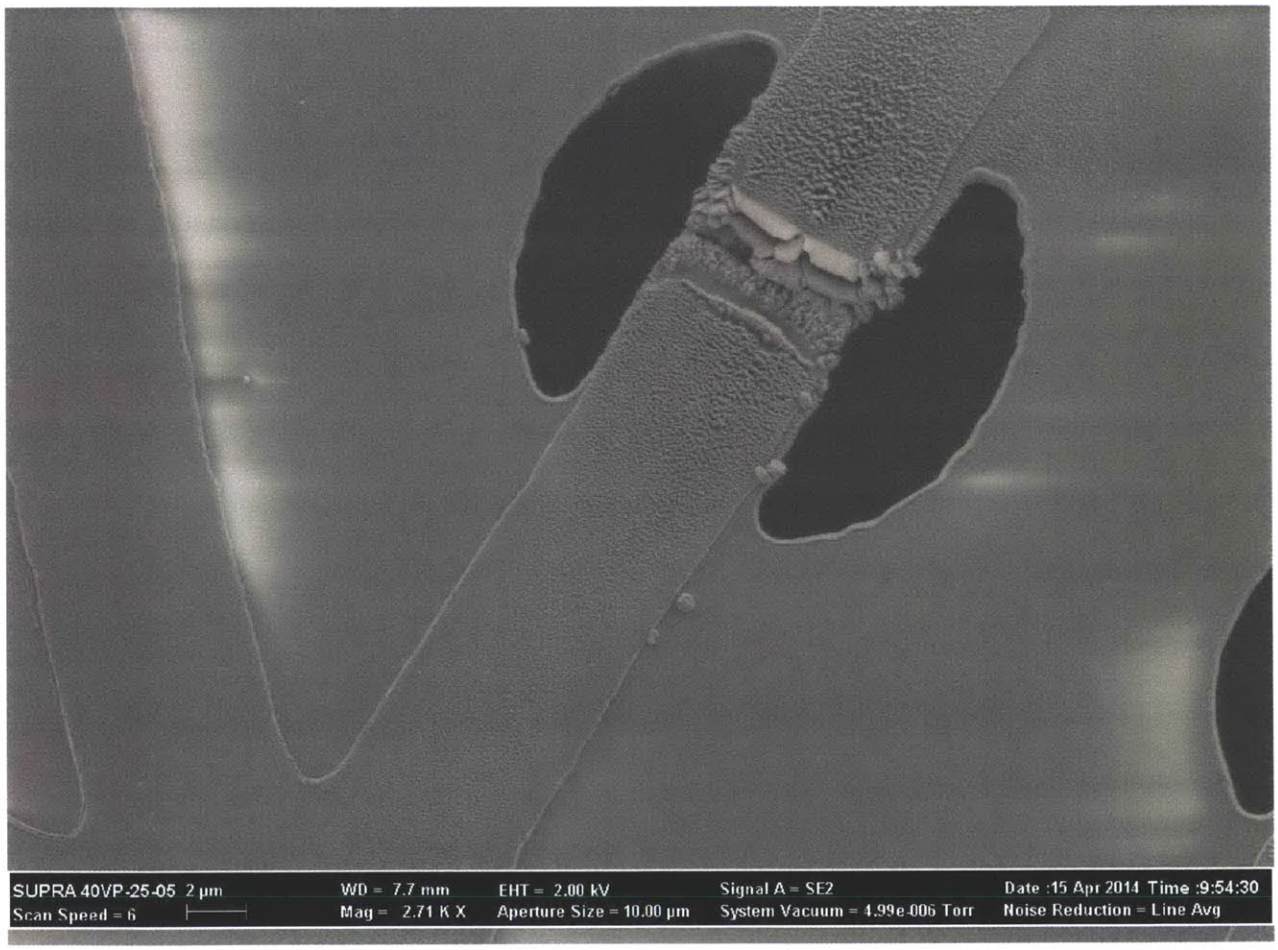

Figure 5.16. SEM image of THz-driven SRR antenna damage at low pressure, showing diffusion of gold electrode material into the antenna gap. Image by K. Fan.

5.6

Discussion

The THz-pump/THz-probe measurements presented above highlight several effects that can all be related to the breakdown processes expected to occur within the SRR antenna gap as a result of the THz electric field. First, the pump/probe traces taken at atmospheric pressure reveal certain evidence of increased in-gap conductivity. This may easily be attributed to THz-driven breakdown of the air in the SRR antenna gap through comparison of the breakdown criteria given in Fig. 5.2 and the enhanced THz field in Fig. 5.3 (b), which clearly shows that the applied fields in are expected to be well in excess of the expected DC breakdown threshold for gaps of the lengths employed (1.5 – 3 μm). Published theoretical results[23], as noted in Sec. 5.1.2, indicate that gaps of this size should exhibit breakdown thresholds at THz frequencies that vary only slightly from measured DC breakdown thresholds as a result of the high contribution of field emission to the overall breakdown process. Therefore, it can be assumed that the enhanced fields, which are far in excess of the DC breakdown potentials for gaps of this size, are also far in excess of the breakdown threshold at the LC resonance frequency at which the breakdown was observed. Furthermore, the essentially flat dynamics observed over the 20 ps pump/probe window (Figs. 5.7 and 5.8) are consistent with the formation of an air discharge, which is expected to persist for a minimum of several nanoseconds[25,26].

Examination of the dependence of the LC resonance bleach on the THz field strength (Fig. 5.12) shows that the onset of the effect in the 1.5 μm gap sample is roughly 220 kV/cm before enhancement, which translates into a breakdown threshold, after SRR enhancement is taken into consideration, of roughly 5.8 MV/cm. Using Eq. 5.8-9, and assuming that $E_{DC}^{Breakdown} \approx E_{THz}^{Breakdown}$, the "surface enhancement" parameter β may be estimated using

$$\beta = \frac{6.85\times10^{7}\varphi^{3/2}}{E\ln(ApdK)-Bp} \tag{5.10}$$

which gives $\beta = 8.2$ using the onset field of 5.8 MV/cm.

The appearance of a long-lived THz-induced LC resonance bleach at low pressure is somewhat harder to explain. At sufficiently low pressures, breakdown occurs only as a result of field emission, as the absence of molecular species within the electrode gap necessarily renders electron impact ionization and secondary electron emission impossible. However, this scenario is incompatible with the observed long-lived LC resonance bleach dynamics, which persist essentially unchanged for the duration of the roughly 20 ps pump/probe window, as seen in Fig. 5.13. Assuming that field emitted electrons begin from rest, the induced acceleration of the electron due to the applied external field results in the electron crossing the gap in a time t_{gap} given by

$$t_{gap} = \sqrt{\frac{2dm}{eE}} \tag{5.11}$$

where d is the gap spacing, m and e are the mass and charge of the electron, respectively, and E is the applied electric field[27]. For the enhanced electric field of 11.6 MV/cm, t_{gap} is calculated to be 120 fs for a 1.5 μm gap, or approximately two orders of magnitude less than the timescale of the observed pump/probe dynamics. Therefore, the observed dynamics are not due to field emission alone, implying the presence of ionized molecular species in the gap despite the low operating pressure. As a result, it can be concluded that the field emission process results in ionization of the small amount of gas molecules present in the antenna gaps at low pressure. It is interesting to note that the electron is accelerated to a velocity of approximately 2.5×10^{7} m/s, corresponding to a kinetic energy of 3.55 keV. This is far in excess of the energy needed to ionize molecules in air[28].

The observed damage, which shows dramatic differences as a function of operating pressure, can be explained by first examining the results observed in vacuum. Irradiation of the SRR structures at low pressure results in diffusion of the gold electrodes into the antenna gap from both directions, resulting in a meeting point in the center of the gap, as can be seen in Fig. 5.16. This diffusion results in the appearance of gold hillocks near the ends of the electrodes, which accumulate and fill the gap. This is readily attributable to electromigration, which is known to occur in thin gold films at high current densities as a result of Joule heating[29,30]. That the gold diffuses into the gap from both electrodes is attributed to the rapid reversal of the THz field, causing current flow in both directions. Electromigration may explain the observed damage at the corners and center of the SRR structures, as these areas are also subjected to high current densities.

The damage observed at atmospheric pressure is more complex in nature, as the damage is observed only spectroscopically in the post-THz pump LC resonance bleach, which is broadened, enhanced and shifted (for 1.5 μm gaps) in damaged samples, as shown in Figs. 5.10 and 5.11. Furthermore, the spectroscopic damage signature is shown to stabilize more quickly for 1.5 μm gaps than for 3 μm gaps. Finally, the gap is not observed to fuse shut as in the case of low-pressure damage, even in the case of significantly higher THz fields, as shown in Fig. 5.9. The lack of gap fusing may be the result of concentration of ionized species in the antenna gap, which is greatly increased at atmospheric pressure as opposed to low pressure. This buildup of charged particles in the antenna gap and the resulting increased collisions of ionized species with the gold antennas may reduce the likelihood of gold protrusion into the gap.

The observed spectroscopic signatures of in-air damage indicate modification to the breakdown process itself, as the pre-overlap THz probe transmission is unchanged for all extents of sample damage. Given that electromigration damage is still observed at the corners and near the gaps of the SRR structures at atmospheric pressure, it is reasonable to assume that some degree of electromigration-

driven modification to the electrode surface occurs. This was confirmed through SEM images of the electrode surfaces near the capacitive gaps of the SRR structures, which show small protrusions (Fig. 5.17). Electrode surface modification would immediately affect the in-gap breakdown process through the Fowler-Nordheim β term, which corresponds to surface field enhancement as a result of surface protrusions. Electromigration-driven increases in the β term would result in higher effective in-gap fields, which would result in increased in-gap ion production. This would result in a higher magnitude of the LC resonance bleach, due to higher THz-induced in-gap conductivity increases. As increased in-gap conductivity should shift the LC resonance to higher frequencies, the observed THz-driven LC resonance shift is also explained by electromigration-induced electrode surface modification.

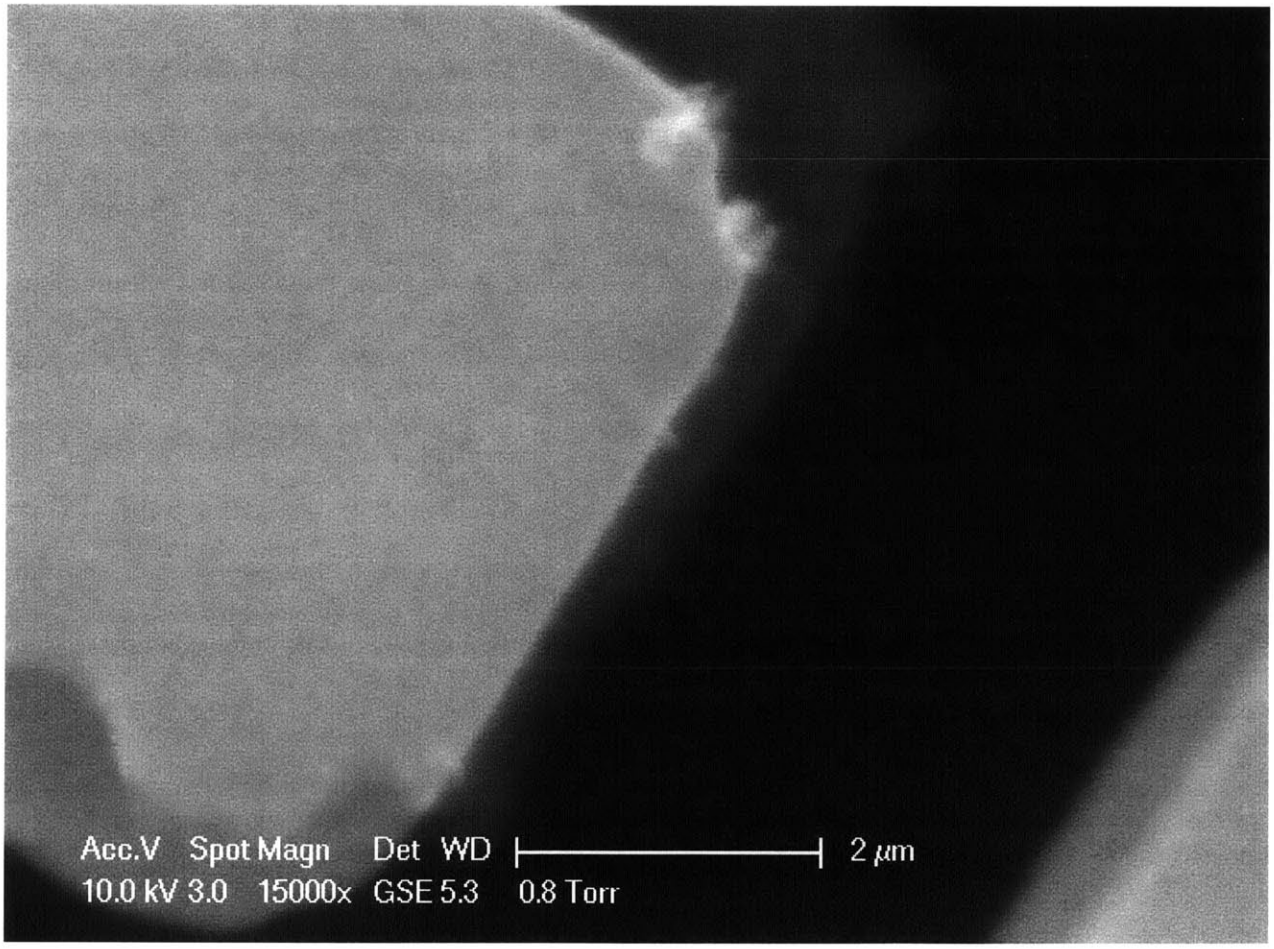

Figure 5.17. SEM image of THz-driven SRR antenna damage at atmospheric pressure, showing capacitive gap with protrusions present on the edge of the gold antenna. Image by P. Sivarajah.

5.7

Conclusions

Free-space THz fields have been shown to induce breakdown in air in the antenna gaps of metamaterial SRR structures at both atmospheric and low pressures, forming the first experimental demonstration of air breakdown between metal electrodes at μm spacing and THz frequencies. At atmospheric pressure, dynamics and frequency responses consistent with in-gap air breakdown are observed for gaps with both 1.5 and 3 μm spacing. In the case of the former, THz fields of roughly 11.6 MV/cm are obtained after SRR enhancement, with threshold fields for breakdown being approximately 5.8 MV/cm. Evidence of air breakdown is further supported by calculated breakdown thresholds, which are approximately one order of magnitude less than the enhanced fields for these lengthscales. At low pressure, THz-driven dynamics with similar timescales but greatly reduced magnitudes are seen, which cannot be attributed to the dominant field emission process, and is instead the result of field-emission-driven ionization despite operating pressures in the single mTorr range.

At low pressure, severe damage is observed after THz irradiation for several hours, which results in the antenna gap becoming fused shut. This is attributed to electromigration due to the high current densities present at the electrode surfaces, with further electromigration seen at the corners of the SRR structures. At atmospheric pressure, corner damage is again seen, but gap fusing is not. Instead, the LC resonance response to the ionization process exhibits evidence of greatly increased transient in-gap conductivity as a result of THz-driven damage, which is postulated to be the result of electromigration-driven growth of protrusions on the electrode surfaces resulting in field localization and enhancement.

The observed effects have strong implications for the study of microgap breakdown phenomena. First, as mentioned previously, the results obtained represent the first demonstration of microgap breakdown phenomena at THz frequencies. Secondly, the ability to drive breakdown

phenomena with THz fields using SRR antennas provides a convenient contact-free platform for more detailed spectroscopic study of high-frequency microgap breakdown, in which ionized species might be identified spectroscopically and their kinetics monitored. Thirdly, the observation of long-lived dynamics for small gap spacing even at low pressure indicates that the assumed similarity between gas and vacuum breakdown at small gap spacing is not applicable at the 1.5 μm spacing employed here. Furthermore, the results obtained, in particular the observed spectroscopic damage signatures in air, showcase the importance of the surface enhancement parameter β in experimental investigations of breakdown as well as the possibility of modification to β and therefore the breakdown process itself as a result of the high current densities typically encountered in microscale structures. This has implications in the design of failure-resistant microelectronic components for high-field applications. Finally, the observation of THz-driven field emission of electrons from the gold surfaces of the SRR antennas has potential applications as a source of high-velocity electrons at THz frequencies, which may be useful in future work involving THz electronics.

References

1. Liu, M. *et al.* Terahertz-field-induced insulator-to-metal transition in vanadium dioxide metamaterial. *Nature* **487,** 345 (2012).

2. Fan, K. *et al.* Nonlinear terahertz metamaterials via field-enhanced carrier dynamics in GaAs. *Phys. Rev. Lett.* **110,** 217404 (2013).

3. Paschen, F. Ueber die zum funkenubergang in luft, wasserstoff und kohlensdure bei verschiedenen drucken erforderliche potentialdifferenz. *Ann. Phys. u Chem.* **273,** 69 (1889).

4. Raizer, Y. P. *Gas Discharge Physics*. (Springer-Verlag Berlin Heidelberg, 1991).

5. Mesyats, G. A. *Pulsed Power*. (Springer Science + Business Media, Inc., 2005).

6. Boyle, W. S. & Kisliuk, P. Departure from Paschen's Law of breakdown in gases. *Phys. Rev.* **97,** 255 (1955).

7. Fowler, R. H. & Nordheim, L. Electron emission in intense electric fields. *Proc. R. Soc. A Math. Phys. Eng. Sci.* **119,** 173 (1928).

8. Burgess, R. E., Kroemer, H. & Houston, J. M. Corrected values of Fowler-Nordheim field emission functions v(y) and s(y). **60,** 515 (1953).

9. Stern, T. E., Gossling, B. S. & Fowler, R. H. Further studies in the emission of electrons from cold metals. *Proc. R. Soc. A Math. Phys. Eng. Sci.* **124,** 699 (1929).

10. Davies, D. K. Vacuum electrical breakdown between plane-parallel copper electrodes. *J. Appl. Phys.* **37,** 2969 (1966).

11. Radmilović-Radjenović, M. & Radjenović, B. Theoretical study of the electron field emission phenomena in the generation of a micrometer scale discharge. *Plasma Sources Sci. Technol.* **17,** 024005 (2008).

12. Radmilović-Radjenović, M. & Radjenović, B. An analytical relation describing the dramatic reduction of the breakdown voltage for the microgap devices. *EPL (Europhysics Lett.* **83,** 25001 (2008).

13. Go, D. B. & Pohlman, D. a. A mathematical model of the modified Paschen's curve for breakdown in microscale gaps. *J. Appl. Phys.* **107,** 103303 (2010).

14. Tirumala, R. & Go, D. B. An analytical formulation for the modified Paschen's curve. *Appl. Phys. Lett.* **97,** 151502 (2010).

15. Venkattraman, A. & Alexeenko, A. A. Scaling law for direct current field emission-driven microscale gas breakdown. *Phys. Plasmas* **19,** 123515 (2012).

16. Dhariwal, R. S., Torres, J.-M. & Desmulliez, M. P. Y. Electric field breakdown at micrometre separations in air and nitrogen at atmospheric pressure. *IEE Proc.-Sci. Meas. Technol.* **147,** 261 (2000).

17. Lee, R.-T., Chung, H.-H. & Chiou, Y.-C. Arc erosion behaviour of silver electric contacts. *IEE Proc.-Sci. Meas. Technol.* **148,** 8 (2001).

18. Farson, D. F., Choi, H. W. & Rokhlin, S. I. Electrical discharges between platinum nanoprobe tips and gold films at nanometre gap lengths. *Nanotechnology* **17,** 132 (2006).

19. Radmilović-Radjenović, M., Matejčik, Š., Klas, M. & Radjenović, B. The role of the field emission effect in direct-current argon discharges for the gaps ranging from 1 to 100 μm. *J. Phys. D. Appl. Phys.* **46,** 015302 (2013).

20. Slade, P. G. & Taylor, E. D. Electrical breakdown in atmospheric air between closely spaced (0.2 um – 40 um) electrical contacts. *IEEE Trans. Components Packag. Technol.* **25,** 390 (2002).

21. Semnani, A., Venkattraman, A., Alexeenko, A. A. & Peroulis, D. Pre-breakdown evaluation of gas discharge mechanisms in microgaps. *Appl. Phys. Lett.* **102,** 174102 (2013).

22. Hatch, A. J. & Williams, H. B. Modes of high-frequency gaseous breakdown. *Phys. Rev.* **112,** 681 (1958).

23. Semnani, A., Venkattraman, A., Alexeenko, A. A. & Peroulis, D. Frequency response of atmospheric pressure gas breakdown in micro/nanogaps. *Appl. Phys. Lett.* **103,** 063102 (2013).

24. Tao, H. *et al.* Performance enhancement of terahertz metamaterials on ultrathin substrates for sensing applications. *Appl. Phys. Lett.* **97,** 261909 (2010).

25. Yang, H. *et al.* Characteristics of self-guided laser plasma channels generated by femtosecond laser pulses in air. *Phys. Rev. E* **66,** 016406 (2002).

26. Tzortzakis, S., Prade, B., Franco, M. & Mysyrowicz, A. Time-evolution of the plasma channel at the trail of a self-guided IR femtosecond laser pulse in air. *Opt. Commun.* **181,** 123 (2000).

27. Young, H. D. & Freedman, R. A. *University Physics*. (Addison Wesley, 2004).

28. Gross, J. *Mass Spectrometry*. (Springer-Verlag Berlin Heidelberg, 2011).

29. Etzion, M., Blech, I. a. & Komem, Y. Study of conductive gold film lifetime under high current densities. *J. Appl. Phys.* **46,** 1455 (1975).

30. Klein, B. Electromigration in thin gold films. *J. Phys. F Met. Phys.* **3,** 691 (1973).

Chapter 6

Ultrafast X-ray Probing of Terahertz-Driven Structural Responses

A major motivating factor in performing nonlinear THz measurements is the desire to drive structural responses in condensed phase systems, with promising applications including next-generation electronics and nonvolatile memory[1,2]. Direct observation of lattice rearrangements following THz pumping therefore forms an extremely valuable tool for the complete understanding of THz-driven dynamics, and is possible with femtosecond X-ray diffraction (XRD). Access to femtosecond XRD probing has been greatly expanded in recent years through the advent of hard X-ray free electron lasers[3–5], which are far brighter than laboratory-based femtosecond X-ray sources[6] and accessible as user facilities. This chapter describes THz-pump/XRD-probe experiments performed at the Linac Coherent Light Source (LCLS) at the SLAC National Accelerator Laboratory, including the observation of lattice rearrangement during the THz-driven insulator-to-metal phase transition in vanadium dioxide and preliminary results showing a possible piezoelectric response following THz pumping of barium titanate. Note that these measurements were performed with a large number of collaborators, who will be identified at the end of the chapter.

6.1

X-Ray Diffraction Probing Methods

6.1.1

X-Ray Scattering by a Single Atom

X-rays are broadly defined as the region of the electromagnetic spectrum that covers 10 to 10^{-3} nm in wavelength[7]. As a result of their extremely short wavelengths, X-rays are capable of diffracting from the inter-atomic spacing within a periodic crystal, as was first realized by Max von Laue[8]. This effect, which is the basis for the ubiquitous use of X-ray diffraction as a probe of crystalline structures, is a result of incident X-rays being scattered by the periodic electron density that exists within a repeating lattice of atoms[7,9]. To understand the details of XRD that will be important in the interpretation of femtosecond XRD experiments, it is useful to first examine the scattering properties of a single object, presented here by reproducing the derivation given by Alloul[9].

The incident X-ray light to be scattered is an electromagnetic wave, for which the time- and position-dependent electric field may be expressed as

$$E_{in}(\mathbf{r},t) = E_0 \mathrm{e}^{i(\mathbf{k}_0\mathbf{r}-\omega t)} \tag{6.1}$$

where E_0 is the incident electric field amplitude, ω is the angular frequency, and the wavevector $\mathbf{k_0}$ points along the direction of propagation and is given by

$$|\mathbf{k_0}| = \frac{\omega}{c} \tag{6.2}$$

After coherent (Thomson) scattering from an electron in an atom (whose electronic composition will be considered later) located at an arbitrary origin, the scattered electric field is given by

$$E_{scat}(\mathbf{r},t) = E_0 \sum_{\mathbf{k}} \alpha_{\mathbf{k}_0,\mathbf{k}} e^{i(\mathbf{k}_0\mathbf{r}-\omega t)} \tag{6.3}$$

where the coefficient α in this case depends both on the scattering medium and the object being scattered.

If the scattering atom is instead placed a distance **u** from the origin, then the position is given by **r - u** and Eq. 6.3 becomes

$$E_{scat}(\mathbf{r},t) = E_0 e^{i\mathbf{k}_0\cdot\mathbf{u}} \sum_{\mathbf{k}} \alpha_{\mathbf{k}_0,\mathbf{k}} e^{i(\mathbf{k}\cdot(\mathbf{r}-\mathbf{u})-\omega t)} \tag{6.4}$$

where the factor $e^{i\mathbf{k}_0\cdot\mathbf{u}}$ corresponds to the phase offset $\mathbf{k_0}\cdot\mathbf{u}$ of the beam scattered by the offset atom as compared to the atom at the origin (i.e. the scenario in Eq. 6.3). In most of our XRD measurements, the scattered X-rays are detected only in a specific direction $\mathbf{k_1}$. Defining the scattering vector $\mathbf{q} = \mathbf{k_1} - \mathbf{k_0}$ allows Eq. 6.4 to be simplified to

$$E_{scat}(\mathbf{k}_1;\mathbf{r},t) = E_0 e^{i\mathbf{q}\cdot\mathbf{u}} \alpha_{\mathbf{k}_0,\mathbf{k}_1} e^{i(\mathbf{k}_1\cdot\mathbf{r}-\omega t)} \tag{6.5}$$

We now turn our attention to the coefficient α in the case that the scattering object is an atom located at the origin with electronic density $\rho(\mathbf{u})$, which will depend on the atomic number of the atom. The amplitude of a scattered X-ray in the $\mathbf{k_1}$ direction is dependent on $\rho(\mathbf{u})$ and is given by

$$E_{scat}(\mathbf{k}_1;\mathbf{r},t) \propto E_0 \rho(\mathbf{u}) e^{i(\mathbf{k}_1\cdot(\mathbf{r}-\mathbf{u})-\omega t)} e^{i\mathbf{k}_0\cdot\mathbf{u}} \tag{6.6}$$

where the vector **u** represents the distance from the scattering electron to the origin. Integration over **u** gives the total scattering by all electrons as

$$E_{scat}(\mathbf{k}_1;\mathbf{r},t) = E_0 \mathrm{e}^{i(\mathbf{k}_1\cdot\mathbf{r}-\omega t)} \int \rho(\mathbf{u})\, \mathrm{e}^{-i\mathbf{q}\cdot\mathbf{u}} d^3\mathbf{u} \tag{6.7}$$

from which comparison to Eq. 6.5 yields

$$\alpha_{\mathbf{k}_0,\mathbf{k}_1} = \int \rho(\mathbf{u})\, \mathrm{e}^{-i\mathbf{q}\cdot\mathbf{u}} d^3\mathbf{u} = f(\mathbf{q}) \tag{6.8}$$

by inspection, where f is referred to as the atomic form factor. This simplifies Eq. 6.5 to

$$E_{scat}(\mathbf{k}_1;\mathbf{r},t) = E_0 f(\mathbf{q}) \mathrm{e}^{i\mathbf{q}\cdot\mathbf{u}} \mathrm{e}^{i(\mathbf{k}_1\cdot\mathbf{r}-\omega t)} \tag{6.9}$$

in the case of X-ray scattering by one atom at position **u** relative to the origin.

6.1.2

X-Ray Scattering by a Lattice

In a crystalline material, atoms are arranged on a periodic lattice based upon a repeating unit cell. The unit cell is defined as the smallest repeating unit, and is described by three sides of length *a*, *b*, and *c*, separated by angles α, β, and γ, as shown in Fig. 6.1. The symmetry of the unit cell is given by one of the fourteen Bravais lattices, of which a full description is widely available[7,9]. Often, XRD measurements are described in terms of the directions **a**, **b**, and **c**, which correspond to the sides of the

unit cell, as well as the planes within a lattice, which are described by Miller indices. Miller indices are given in the form (xyz) where the integers x, y, and z correspond to the fractional intercepts of the lattice plane with the axes **a**, **b**, and **c**. This is shown schematically in Fig. 6.2.

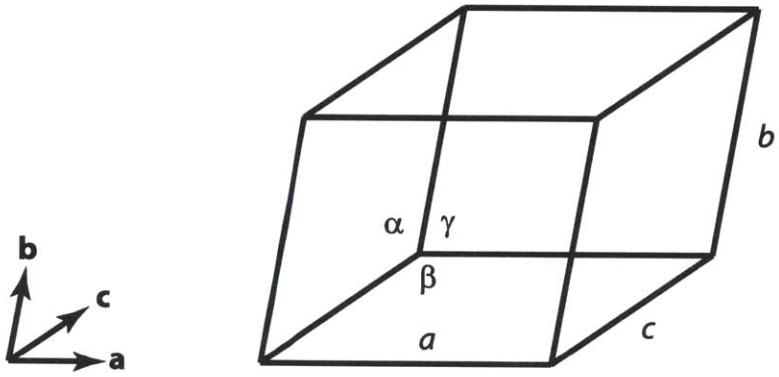

Figure 6.1. Schematic representation of a general unit cell.

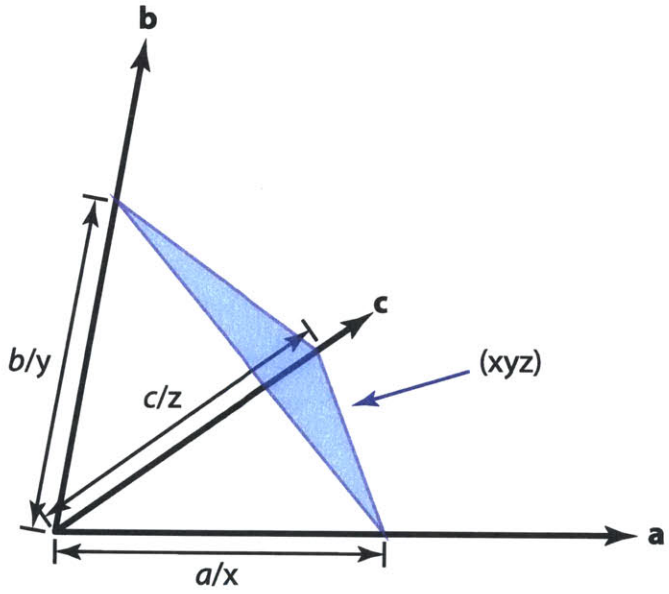

Figure 6.2. Intercepts of (xyz) lattice plane with axes **a**, **b**, and **c**.

Mathematically, scattering of X-rays by a lattice can be developed starting with Eq. 6.9, which describes the amplitude of X-rays that have been scattered by an atom at an arbitrary position **u** relative to an origin. Critically, Eq. 6.9 implies that an X-ray scattered by an atom at position **u** will have a phase

difference $\mathbf{q}\cdot\mathbf{u}$ relative to an X-ray scattered by an atom at the origin[9]. In a crystalline material, the phase difference imparted to X-rays scattered by different atoms will usually result in very small scattered intensities, as the scattered X-rays will add together out of phase. However, certain scattering directions will exhibit additive phase shifts that result in constructive interference between the scattered beams, leading to large scattering amplitudes.

In the context of the lattice planes within a crystal, this gives rise to the Bragg condition for diffraction, which is illustrated graphically in Fig. 6.2. In Fig. 6.2, as two phase-coherent beams $\mathbf{k_0}$ and $\mathbf{k_0}'$ diffract off adjacent lattice planes, phase coherence between the diffracted beams $\mathbf{k_1}$ and $\mathbf{k_1}'$ is achieved only if the extra path distance travelled by $\mathbf{k_0}'$ and $\mathbf{k_1}'$ is an integer multiple of the wavelength of the beam. Mathematically, this is given as the Bragg law

$$2d' \sin\theta = n\lambda \tag{6.10}$$

where λ is the wavelength of the incident X-rays, n is an integer, and

$$d' = nd \tag{6.11}$$

where d is the spacing of the lattice planes[7].

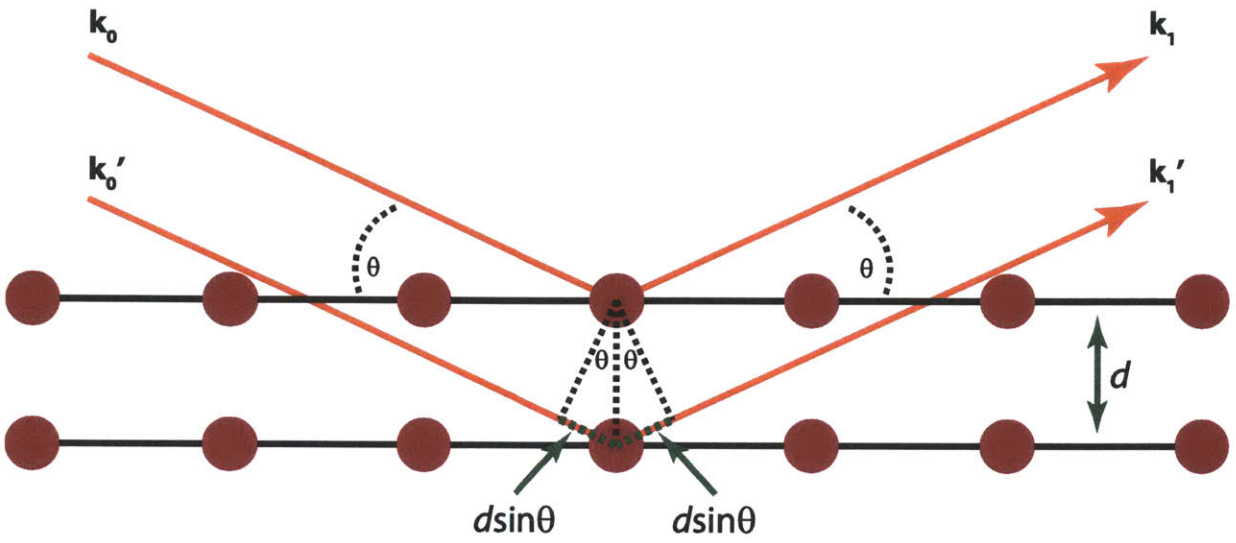

Figure 6.3. Illustration of the Bragg diffraction condition for n = 1, in which scattered X-rays along $\mathbf{k}_1$ and $\mathbf{k}_1'$ add coherently if the additional path segments travelled along $\mathbf{k}_0'$ and $\mathbf{k}_1'$ relative to $\mathbf{k}_0$ and $\mathbf{k}_1$ are each equal to $d\sin\theta$ as indicated.

More generally, the von Laue formulation for XRD may be used, in which the total scattered electric field for n atoms arranged on a lattice is given by

$$E_{scat}(\mathbf{k}_1;\mathbf{r},t) = A(\mathbf{q})\mathrm{e}^{i(\mathbf{k}_1\cdot\mathbf{r}-\omega t)} \tag{6.12}$$

where $\mathbf{R}_n$ represents the spatial position of each atom on the lattice, and the amplitude $A(\mathbf{q})$ is given by

$$A(\mathbf{q}) = E_0 f(\mathbf{q}) \sum_n \mathrm{e}^{-i\mathbf{q}\cdot\mathbf{R}_n} \tag{6.13}$$

For a crystal consisting of N heterogeneous atoms (i.e. $f(\mathbf{q})$ is position-dependent), with the position of each atom within the unit cell given by $\mathbf{r}_l$, the total diffraction amplitude is then given by

$$A(\mathbf{q}) = E_0\left[\sum_{l=1}^{N} f^{(l)}(\mathbf{q})\mathrm{e}^{-i\mathbf{q}\cdot\mathbf{r}_l}\right]\left[\sum_n \mathrm{e}^{-i\mathbf{q}\cdot\mathbf{R}_n}\right] \tag{6.14}$$

where the first summed term is only nonzero if the Bragg condition is met, as it results from the von Laue conditions, and is dependent on the type of lattice symmetry as given by the Bravais lattice. The second term

$$S(\mathbf{q}) = \left[\sum_{l=1}^{N} f^{(l)}(\mathbf{q}) \mathrm{e}^{-i\mathbf{q}\cdot\mathbf{r}_l}\right] \tag{6.15}$$

is referred to as the structure factor, and is dependent upon the basis of the unit cell. Furthermore, Eqs. 6.7-8 show that the atomic form factor *f* is merely the Fourier transform of the electronic density from which the incident X-rays scatter. Taken together, this implies that the total scattered amplitude along $\mathbf{k_1}$ is directly dependent on the Fourier transform of the periodic electronic density within the lattice.

Taken as a whole, it is seen that, when a beam on X-rays is incident upon a crystalline sample, Eqs. 6.12-6.15 imply that the observed diffraction intensity is only nonzero when the Bragg condition is met, directly giving information on the lattice spacing of the crystal (and the unit cell arrangement, discussion of which is widely available[7,9]). Furthermore, the amplitudes of the observed diffraction peaks when the Bragg condition is met (referred to as Bragg reflections) are dependent on the periodic spatial distribution of electrons within the lattice. These two factors form the basis for the use of XRD as a powerful tool for the determination of the structural arrangements of crystalline systems.

6.1.3

Femtosecond XRD Probing

In the static case, collection of XRD patterns requires three basic elements, namely a source of X-rays, a sample, and an X-ray detector[10]. In a commercial XRD spectrometer, these elements are

arranged such that the source is incident upon the sample at an angle θ and the detector is aligned relative to the projected source beam by 2θ (Fig. 6.4). Note that θ corresponds to the angle of the same name in Eq. 6.10, as both represent the angle of incidence of the X-rays upon the sample. While many orientations of the sample relative to the source and detector are possible with additional angular degrees of freedom[11], many static measurements are taken in the θ-2θ geomtery, in which θ and 2θ are varied simultaneously, resulting in a change in the magnitude of the scattering vector **q** but not its direction[12]. As such, only the out-of-place lattice direction along **q** is probed (Fig. 6.5 (a)). By scanning a large enough range $\Delta\theta$, with varying sample orientations, enough Bragg reflections may be collected to allow determination of the unit cell symmetry of the sample.

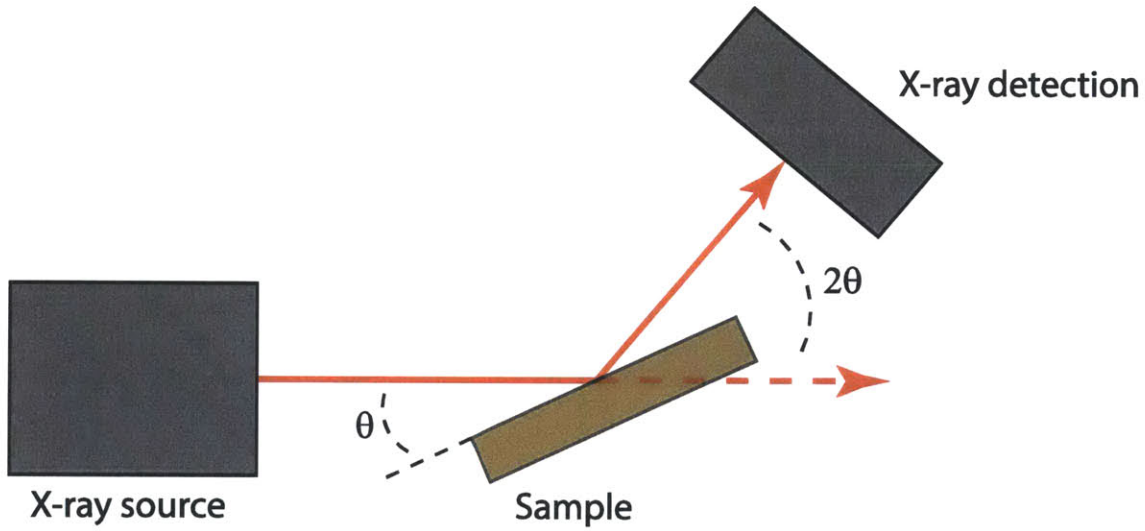

Figure 6.4. Orientation of X-ray source and detection equipment relative to the sample in typical XRD experimental geometry.

Moving to femtosecond XRD probing presents several constraints. First, the low repetition rate and relative scarcity of available beamtime associated with XFEL sources typically permit only a few Bragg reflections to be collected, implying a need for careful sample characterization prior to

femtosecond XRD experiments. The number of reflections that may be collected is also constrained by the relatively noisy output of XFEL sources as well as the need to collect data at varying time delays.

The detection methods employed at the LCLS also require modification to the techniques used to collect Bragg reflections because the detection equipment is frequently immobile. Therefore, the θ-2θ geometry is not useable as it requires a detector that moves in a concerted fashion with the sample rotation angle θ relative to the incident X-rays. Instead, the rocking curve geometry is used, in which the sample is rotated through a small angular range $\Delta\theta$. Because the detection angle is fixed, the scattering vector **q** is varied in direction rather than magnitude, and as such is sensitive to both in-plane and out-of-place lattice parameters (Fig. 6.5 (b))[12].

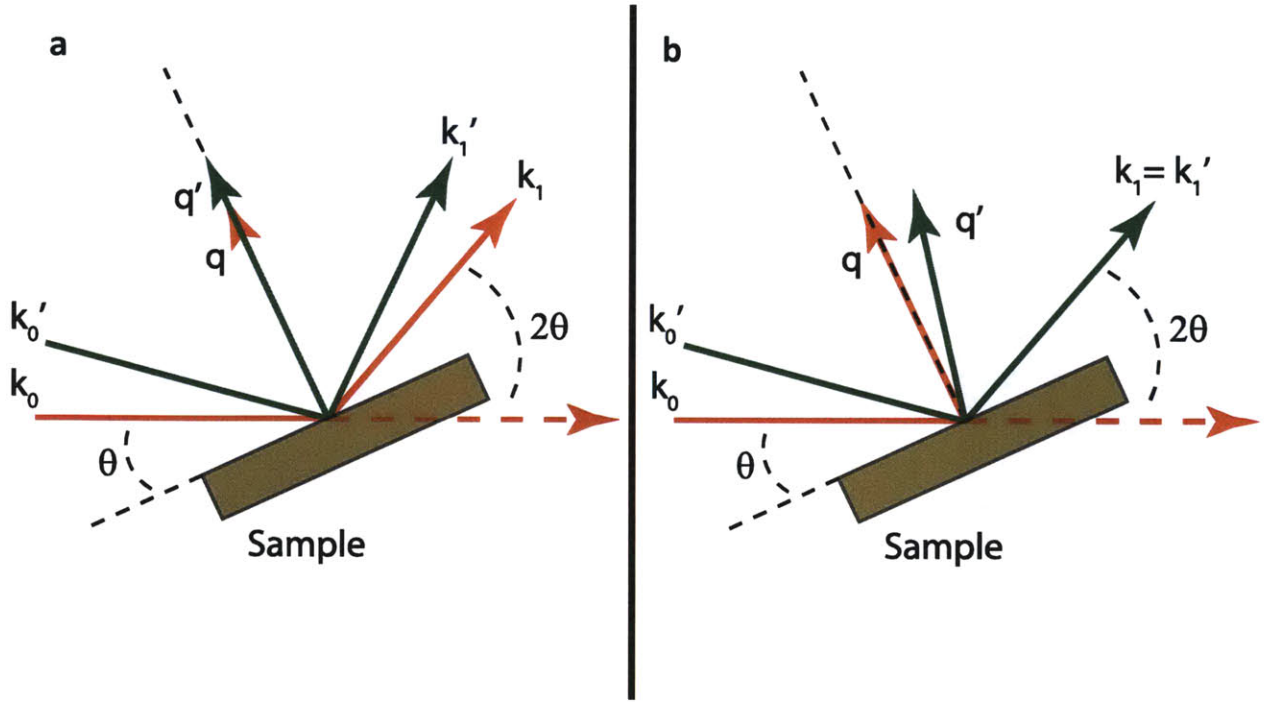

Figure 6.5. (a) Geometry used in θ-2θ scanning method, in which the magnitude of the scattering vector **q** is varied but not its direction. **(b)** Geometry used in rocking curve scanning method, in which the direction of **q** is varied due to $\mathbf{k_1}$ being fixed.

When detected using either the θ-2θ or rocking curve methods, a single Bragg reflection appears as a narrow peak over some angular range with a width $\delta\theta$. Based on the relationships presented Eq. 6.12-6.15, some basic insight can be gleaned from the appearance of the Bragg reflection. First, the angular position of the peak, i.e. the value of θ around which it is centered, corresponds to the value of θ which satisfies the Bragg condition for the incident X-ray wavelength λ and lattice plane spacing d. As λ is known, the position of θ at which the peak appears is a direct report of the lattice plane spacing. Note that the peak position is often reported in the reduced variable $Q = (4\pi\sin\theta)/\lambda$. The intensity of the peak is also of interest, as it is dependent upon the structure factor $S(\mathbf{q})$, which is seen in Eq. 6.15 to correspond to the Fourier transform of the periodic electron density within the crystal (i.e. the location of the electrons in reciprocal space) as well as the atomic form factors $f(\mathbf{q})$. In other words, the intensity of the Bragg reflection is a reporter on the arrangement and types of atoms within the crystal lattice. Furthermore, the width of the Bragg reflection is also dependent upon the structure factor[13]. It should be noted at this point that this analysis is very simplified, and ignores many effects and insights relating to the symmetry and composition of the unit cell; however, for the purposes of this thesis two basic conclusions will suffice: that the position of the Bragg reflection is indicative of the size of the unit cell of the sample, and the intensity and width of the Bragg reflection are indicative of the atomic arrangement and composition within the unit cell.

The recording of a femtosecond XRD measurement as an ultrafast probe implies that many rocking curve scans of the sample must be taken for varying time delays relative to the pump pulse being used (in most cases presented here, it will be a THz pulse). However, the time-consuming nature of rocking curve collection requires that ultrafast pump-induced structural changes be verified first using simpler scanning methods. For this purpose, it is convenient to detect only a single value of θ while scanning the time delay between the pump pulse and the XRD probe pulse. Selection of a point on the side of the Bragg reflection peak gives maximum sensitivity to angular shifts of the Bragg peak to lower

or higher values of θ, implying pump-induced changes in the size of the unit cell. Alternatively, selection of the value of θ that corresponds to the peak of the Bragg reflection is sensitive to changes in both the position of the peak and its intensity, and as such is sensitive to changes in both the size and arrangement of the unit cell. Both methods, as well as the more painstaking collection of time-dependent full rocking curves, will be used throughout this chapter.

6.2

Femtosecond X-Ray Pulses from the Linac Coherent Light Source

The experiments described in this chapter were performed at the Linac Coherent Light Source (LCLS) at the SLAC National Accelerator Laboratory in Menlo Park, CA, which is an X-ray free electron laser (XFEL). Briefly, the operation of a free electron laser (FEL) is based upon the oscillation of a beam of accelerated electrons between alternating pairs of opposing magnets, referred to as an undulator. As the electrons rapidly oscillate in the undulator, they emit electromagnetic radiation, which can be tuned in frequency through variation of the electron energy or undulator magnet spacing[3]. At its simplest, an undulator is capable of producing incoherent light emission, as is done in a typical synchrotron X-ray source. An FEL produces coherent emission by taking advantage of the interaction of the emitted electromagnetic radiation with the electrons generating it. As the electrons pass through the undulator, they interact with the electric field of the light that they emit, and as a result form bunches (the so-called FEL instability), which results in phasematching between the emitted radiation and the propagating electrons (Fig. 6.6)[3,4].

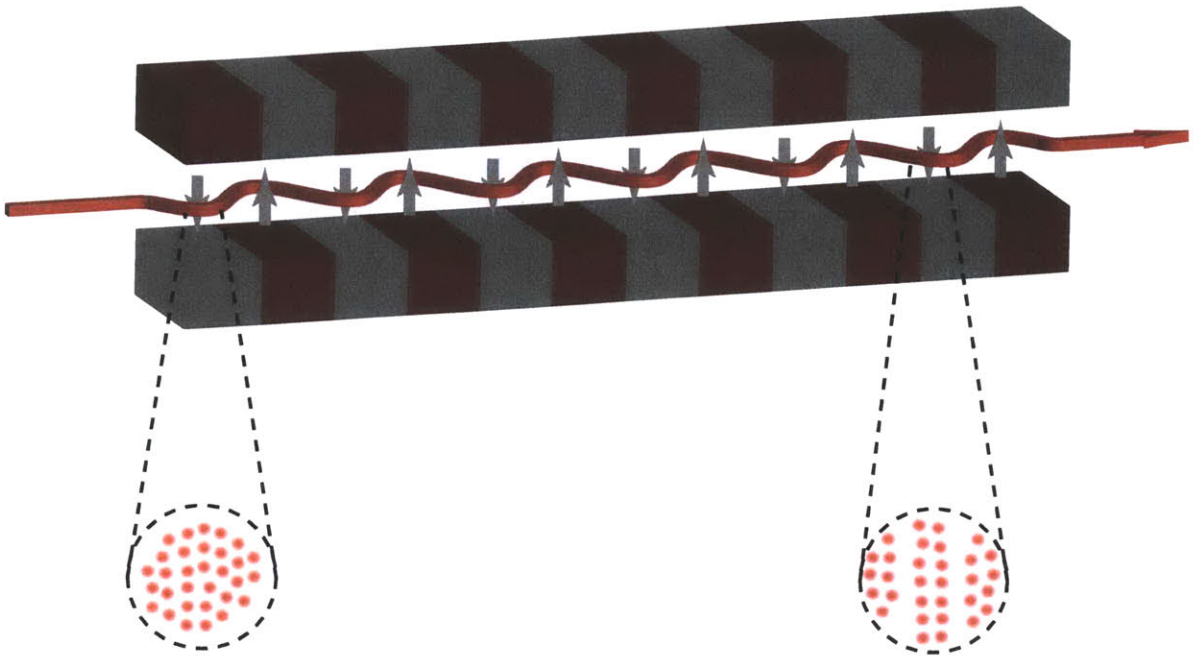

Figure 6.6. Schematic diagram of undulator in FEL operation, in which incoming electron pulses oscillate between alternating magnet pairs, leading to electromagnetic radiation emission. In an FEL, initially uniform electron pulses (left detail) become bunched during propagation (right detail) as a result of interaction with the emitted radiation, leading to phasematched emission of coherent pulses of light.

Operation of an XFEL is significantly more difficult than FEL operation at lower frequencies because of the high electron energies required and the lack of suitable optics, which precludes the use of a cavity[3,4]. The LCLS, which was the first XFEL capable of hard X-ray operation, obtains a very high quality electron beam, with electron energies up to 15 GeV, using one third of the original 1960's-era SLAC linear accelerator, which was originally constructed for particle physics research. The high-energy beam of electrons is passed through a single 132 m undulator, avoiding the need for a cavity altogether[5]. This combination of a very high-energy electron source and a very long undulator is capable of producing femtosecond pulses of hard X-rays with up to 5 mJ pulse energy and 10-250 fs pulse durations at X-ray photon energies ranging from 285 eV to 9.6 keV[14].

All measurements presented here were performed using the X-ray Pump Probe (XPP) instrument at the LCLS, which offers X-ray energies between 4 and 10 keV in pulses with 80 fs nominal

duration. A titanium:sapphire amplified laser system, which produces 24 mJ pulses of 130 fs duration at approximately 800 nm central wavelength and is synchronized to the XFEL repetition rate allows for the implementation of both 800 nm and THz sources that are synchronized to the X-ray pulses.

6.3

THz Implementation at LCLS

Implementation of tilted-pulse-front THz generation at LCLS requires significantly more engineering than laboratory-based THz instruments due to the physical constraints imposed on the setup geometry as a result of the presence of X-ray delivery and detection equipment. The experimental setup used is displayed in Fig. 6.7, and consists of a tilted-pulse-front layout essentially similar to those described in Chapter 2, combined with two 3" diameter parabolic (OAP) focusing optics, with 7" and 3" effective focal lengths. These components were mounted to the support infrastructure surrounding the goniometer used for sample mounting and positioning in the XPP experimental hutch. Overlap of the X-ray and THz pulses was accomplished by drilling a hole in the second OAP focusing optic, through which the X-ray beam passed. An 800 nm pulse that was synchronized with the x-ray pulse was used to generate the THz pulse, thereby enabling THz pump - X-ray probe measurements with reliable timing control.

A second 800 nm pulse, shown in Fig. 6.7, was used for EOS characterization and optimization of the THz source. This pulse was also used for the determination of the relative timing between the THz and X-ray pulses. This was accomplished by first determining the timing between the optical pulse and the X-ray pulse using a sample that gave a measurable optical-pump/XRD-probe signal using either 800 nm or frequency-doubled 400 nm pumping. The optical pulse was delayed relative to the XFEL through electronic methods[15]. Once the relative timing of the optical pulse and X-ray pulse was known, temporal

overlap of the THz and optical pulses using EOS allowed the timing between the THz and X-ray pulses to be determined. This arrangement is shown schematically in Fig. 6.8.

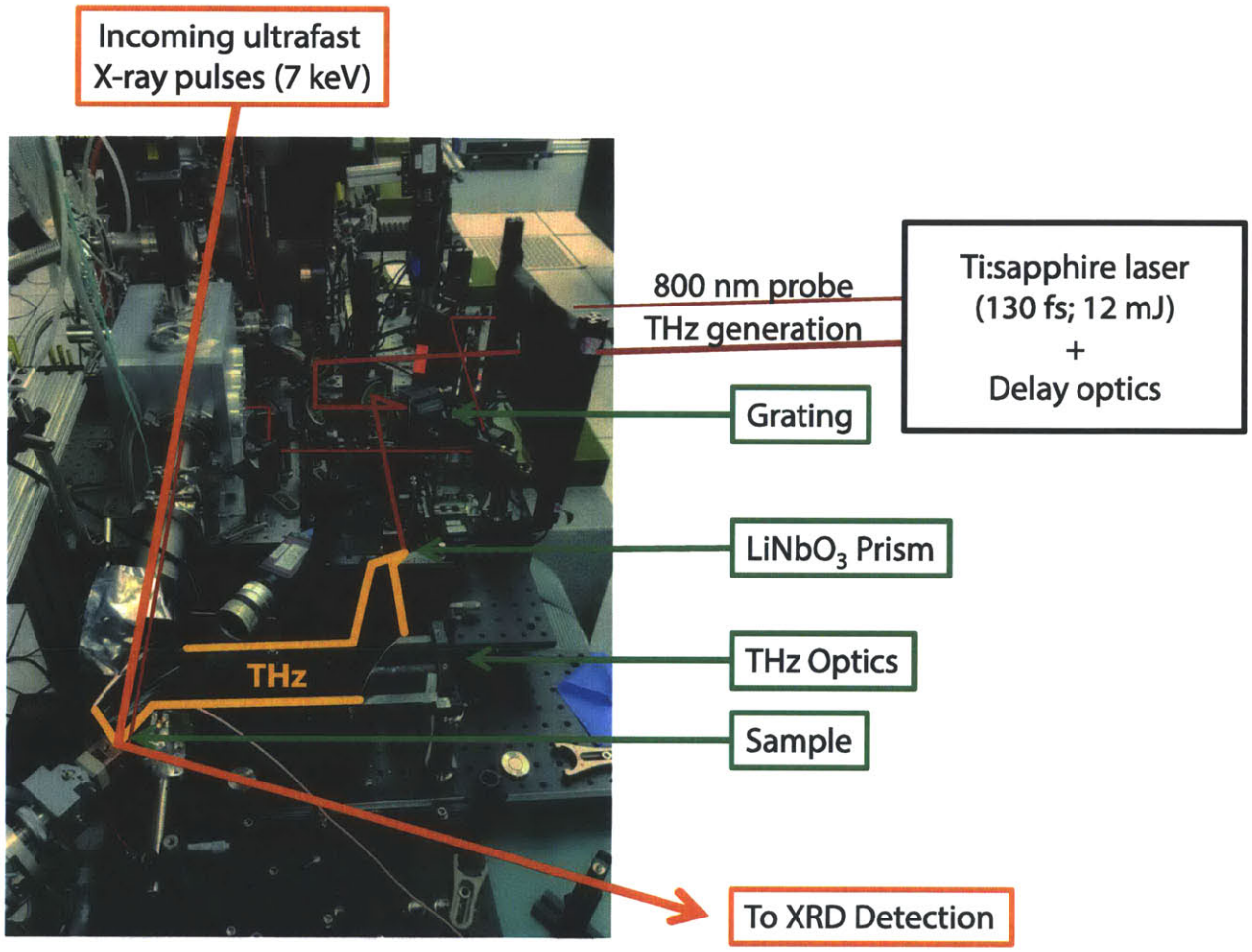

Figure 6.7. Annotated photograph of as-constructed THz-pump/XRD-probe setup in the XPP hutch at LCLS.

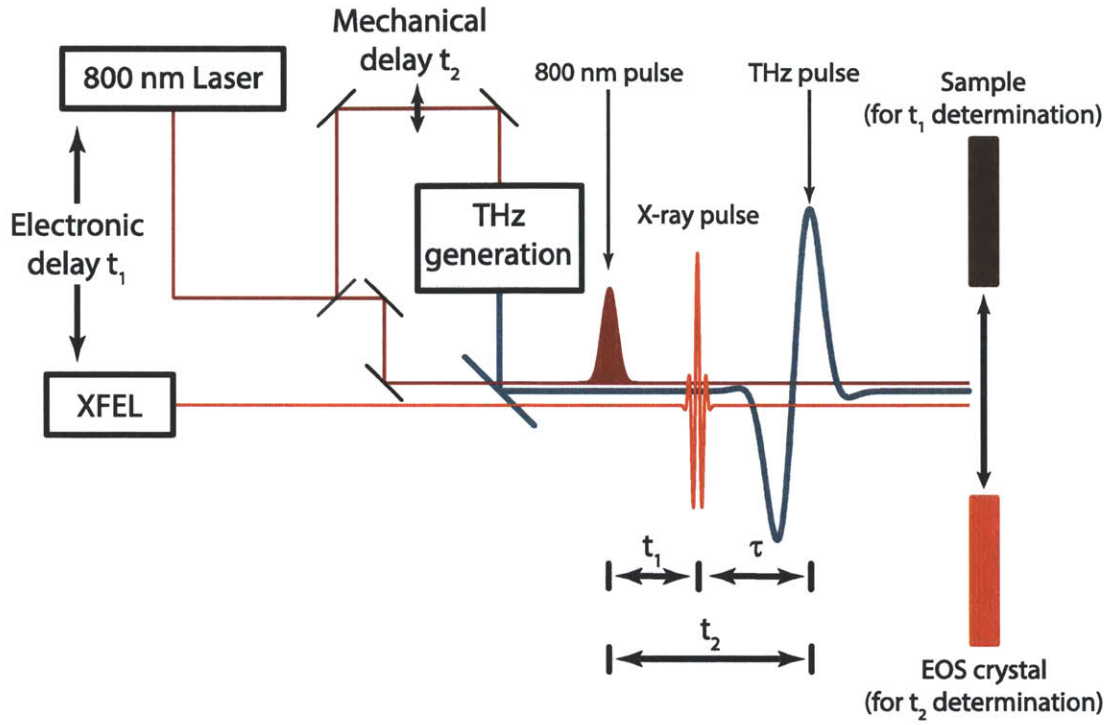

Figure 6.8. Simplified schematic illustration of procedure used to find relative timings between X-ray, THz, and 800 nm pulses, in which the 800 nm pulse timing relative to the X-ray pulses (t_1) is determined using an electronic delay and the 800 nm pulse timing relative to the THz pulse (t_2) is set using a mechanical delay stage, allowing for precise determination of the relative delay (τ) between the X-ray and THz pulses. In typical operation, t_2 is set to zero, and THz-pump/XRD-probe data are acquired by scanning t_1.

Alternate geometrical arrangements are also possible, in which the THz pump pulse is normally incident upon the sample surface. Because the THz pump pulse was vertically polarized, reflective losses at the sample surface would be minimized at this angle of incidence, which is potentially useful for samples such as ferroelectric perovskites with very high THz indices. This geometry is accomplished through the use of an OAP reflector that has a non-90 degree reflection angle (Fig. 6.9). The arrangement presented in Fig. 6.9 utilized a 30 degree OAP, as the angle of incidence for the X-ray pulses on the sample was in this case very close to this angle. To date, while the geometry has been demonstrated in-situ at the LCLS, no successful experiments have been conducted using it.

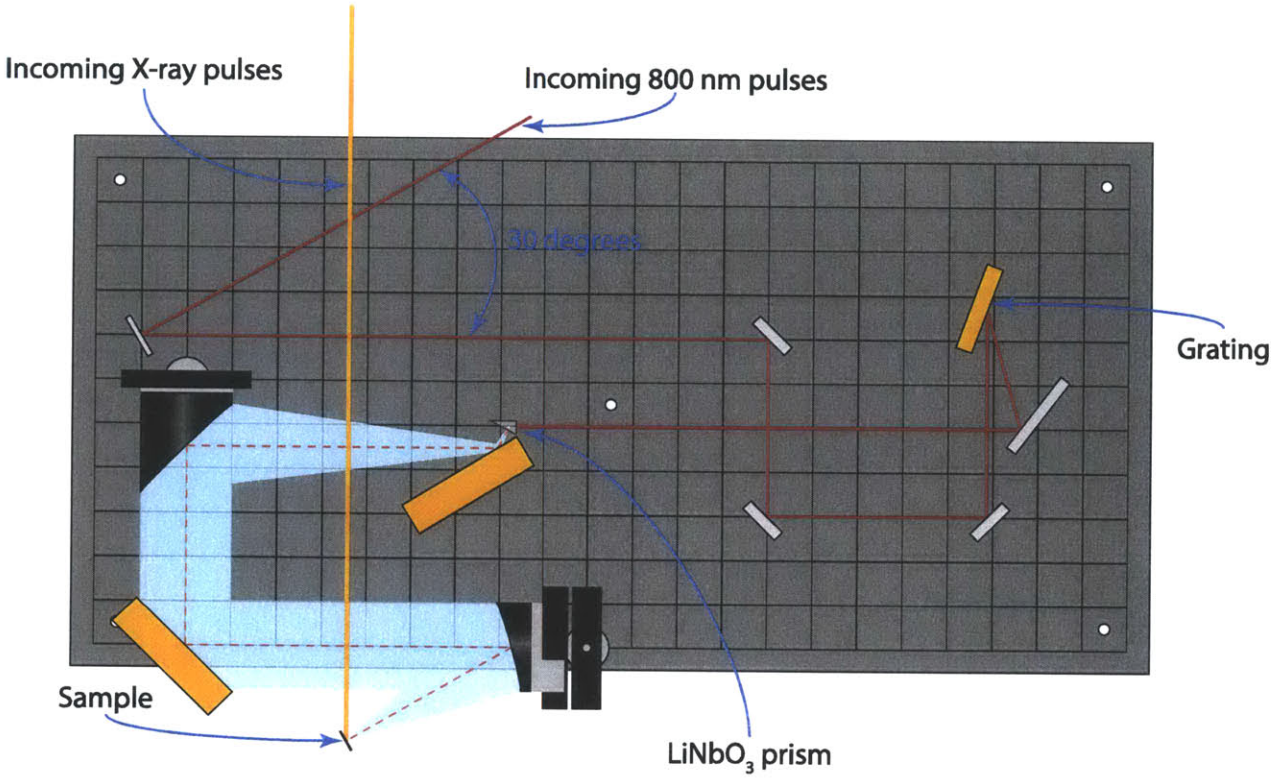

Figure 6.9. Integration of tilted-pulse-front THz source and femtosecond XRD probing in which the THz pulse is normally incident on the sample surface, utilizing a 7.5 inch EFL, 90 degree OAP and a 4.3 inch EFL, 30 degree OAP (some optics omitted for clarity). 800 nm light is coupled into the setup at a 30 degree angle so that the THz focus depth on the sample may be adjusted if the setup is translated parallel to that angle.

6.4

Ultrafast XRD Probing of the Insulator-to-Metal Phase Transition in Vanadium Dioxide

[Note:

The measurements and analysis described in this section are the results of LCLS proposal L702, for which 60 hours of LCLS beamtime were obtained in February, 2013; additional measurements were taken under proposal LC70, for which 48 hours of beamtime were obtained in April, 2014, and analysis is ongoing.]

6.4.1

Vanadium Dioxide Background

Vanadium dioxide (VO_2), which is a prototypical correlated electron material, has attracted much interest in recent years as a result of its fundamental interest and its promising applications in next-generation electronics. Central to these applications is the well-known insulator-to-metal phase transition (IMT), which it undergoes at 340 K[16]. Above the transition temperature, VO_2 exhibits the electronic behavior of a metal[17,18]. In this state, the V 3*d* orbitals participate in several bonding interactions with the O 2*p* orbitals. Of these, the π^* orbital, in which the d_{xz} and d_{yz} orbitals participate, and the $d_{||}$ orbital, in which the $d_{x^2-y^2}$ orbital participates, are of interest in the IMT mechanism (Fig. 6.10 displays the molecular orbital diagram of the metallic state). In the metallic state, both are relatively equally occupied and are located at the Fermi level, leading to the observed metallic behavior[19,20]. Structurally, the metallic phase exhibits a rutile (tetragonal) structure, with each V atom surrounded by a nearly perfect octahedron of O atoms (Fig. 6.11).

If the temperature is lowered beneath the phase transition temperature, both electronic and structural changes are observed, which are shown in Figs. 6.10 and 6.11. Structurally, a transition to a monoclinic phase is observed, with each V atom moving to off-centered positions within the

surrounding O_6 octahedron, which results in V-V dimerization along the c_R axis of the rutile phase (sometimes described as an antiferroelectric displacement due to the alternating offsets of V atoms in each pair of neighboring O_6 octahedra)[17,18]. Electronically, significant changes to the π^* and $d_{||}$ molecular orbitals are seen as the phase transition temperature is crossed. The π^* orbital is shifted upwards in energy as the result of increased *p-d* bonding, which stems from the displacements of the V atoms away from the centers of the octahedra of O atoms surrounding them[18]. The $d_{||}$ molecular orbital displays a more drastic shift as a result of V-V dimerization along the rutile c_R axis, in which energetic factors cause it to split in a fashion analogous to the Jahn-Teller effect, giving rise to a low-lying $d_{||}$ orbital, which is located below the Fermi level, and a higher-energy $d_{||}^*$ orbital, which is located above the π^* orbital. Electronic population is concentrated in the low-lying $d_{||}$ orbital[19]. The splitting of the $d_{||}$ orbital and the increased energy of the π^* orbital result in an optical bandgap, giving rise to the observed insulating behavior in the monoclinic phase, which manifests itself as a decrease in conductivity of several orders of magnitude as the metallic phase gives way to the insulating phase[21]. Significant controversy has arisen over the nature of the phase transition and the relative contributions of the highly intertwined structural and electronic transitions.

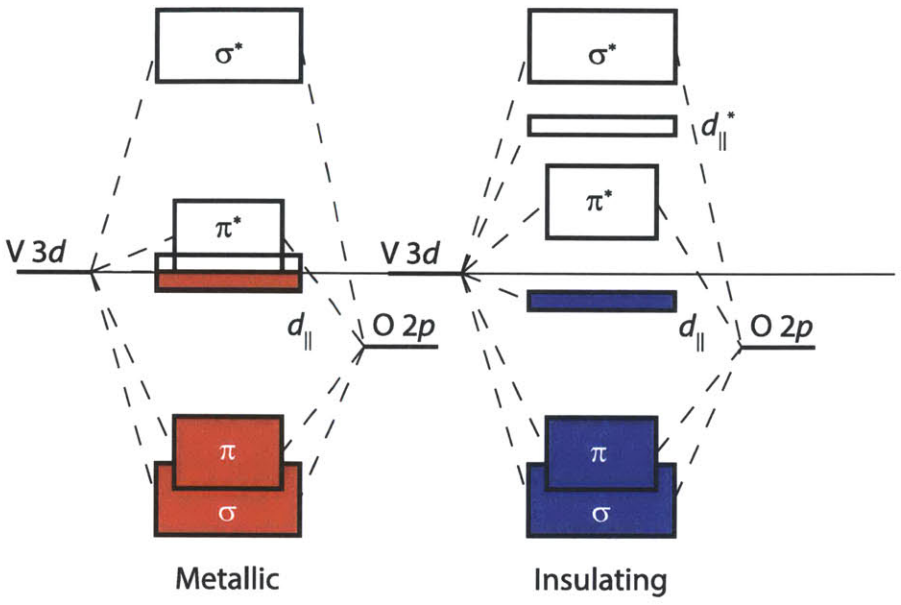

Figure 6.10. Molecular orbital diagrams for the metallic (left) and insulating (right) phases of VO_2. In the insulating phase, the energy of the π^* orbital is raised relative to the metallic phase, and the $d_{||}$ orbitals become nondegenerate, leading to the formation of a bandgap. Figure adapted from Quackenbush, et. al.[22].

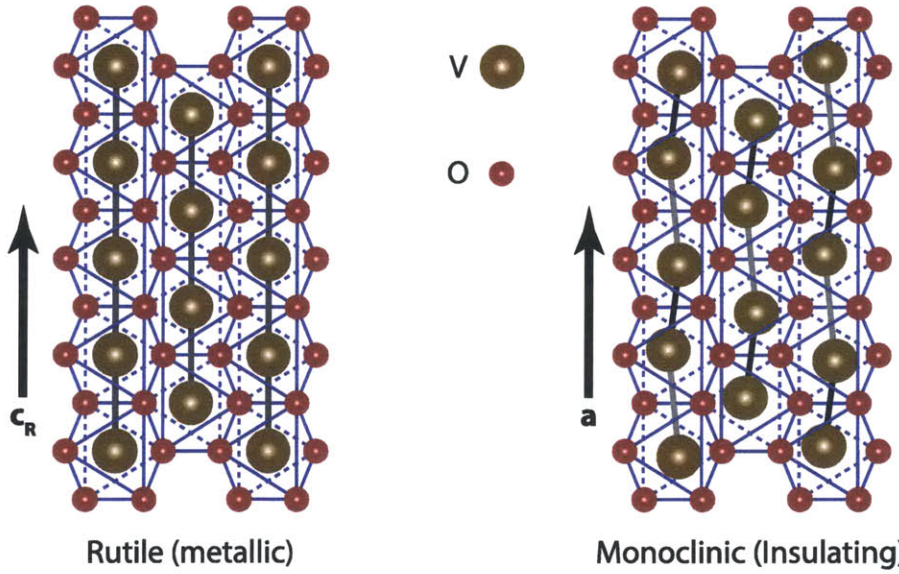

Figure 6.11. Crystal structures of the rutile (metallic) and monoclinic (insulating) phases of VO_2. In the metallic phase, each V atom is centered within an O_6 octahedron, and all V-V distances are equal. In the insulating phase, the V atoms have dimerized along the c_R axis (corresponding to the a axis in the monoclinic phase) and moved to off-center positions within the O_6 octahedra, resulting in unequal V-V distances as shown. Figure adapted from Quackenbush, et. al.[22].

THz driving of the IMT (the first-ever instance of a THz-driven phase transition) was demonstrated in 2012, in which SRR-enhanced free-space THz pulses were shown to drive the transition in thin films of VO_2 on sapphire at an initial temperature approximately 15 K below the phase transition temperature[2]. The spectral response of the phase transition in the THz frequency range was observed through the LC resonance of the SRRs used for field enhancement, using either the transmitted THz pump pulse or a second time-delayed THz probe pulse, as was illustrated in Chapters 4 and 5 of this thesis (Fig. 6.12). The results of these measurements suggested a two-step mechanism, in which the enhanced THz field first liberates electrons in the lattice, and then the enhanced field accelerates the liberated electrons to high energies. The resulting hot electrons raise the lattice temperature through Joule heating, which drives the material through the IMT.

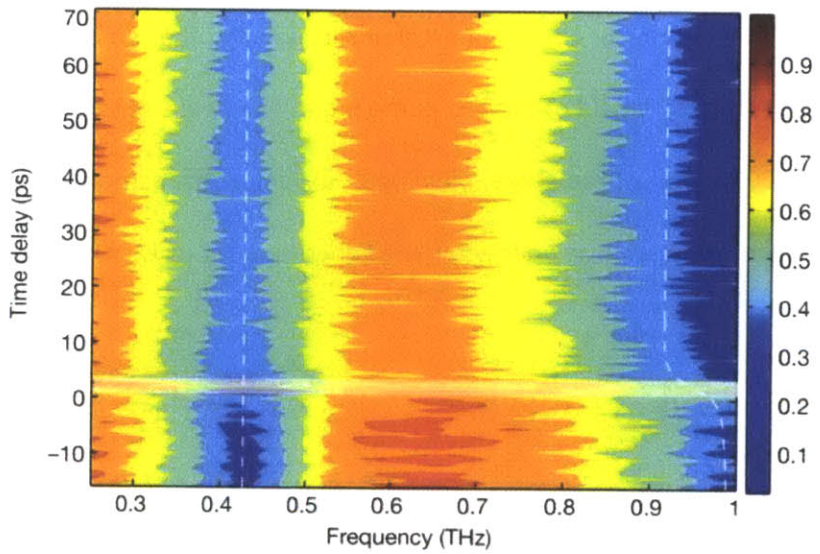

Figure 6.12. (Reproduced from Liu, et. al.[2]) THz probe transmission through an array of SRRs on a 75 nm VO_2 thin film as a function of THz-pump/THz-probe delay time. After arrival of the THz pump at t = 0, a long-lived transmission decrease is observed, which corresponds to increased VO_2 conductivity as a result of the IMT induced by the THz pump.

6.4.2

Sample Characterization

The THz measurements described in the previous section were only sensitive to the electronic signatures of the IMT, as the SRR structures used for monitoring the IMT are sensitive to in-gap conductivity through their LC resonance. Examination of the corresponding ultrafast structural dynamics of the THz-driven IMT was done through THz-pump/XRD-probe measurements at the LCLS using the setup described in the previous section. The samples used in the initial round of measurements consisted of 200 nm films of epitaxially grown VO_2 contained within the field-enhancing regions of gold metamaterial structures, which in this case were long slits (shown schematically in Fig. 6.13). The VO_2 films were grown such that the VO_2 c_R axis (that is, the c axis of the rutile unit cell) was oriented in the out-of-plane direction. Simulations of the metamaterial slits showed that an enhancement factor of 4 was expected for the peak electric field of the THz pump pulse. The field strength of the THz pump pulse was measured to be 500 kV/cm in free space, yielding 2 MV/cm at the sample after metamaterial slit enhancement, with the input laser pulse energy for THz generation set to 12 mJ.

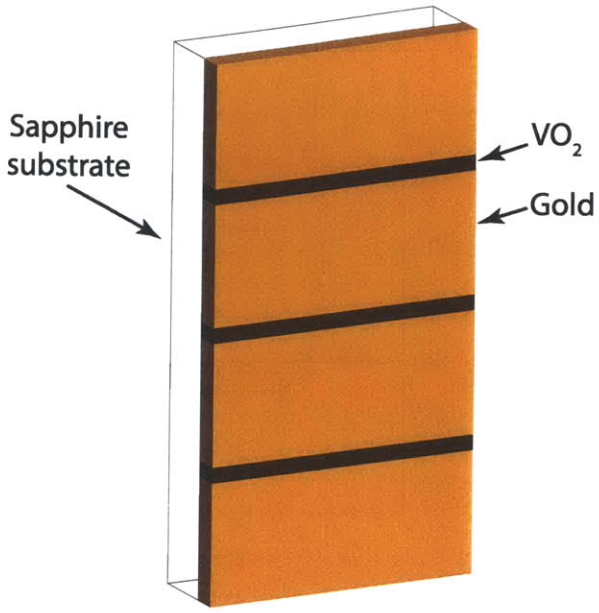

Figure 6.13. Schematic illustration of sample used for THz-pump/XRD-probe measurements on the IMT in VO_2. 200 nm films of epitaxial VO_2 were sandwiched between gold regions, forming slits of 1.65 μm height and 15 μm periodicity. Note that the actual sample width and height were several mm.

Prior to collection of THz-pump/XRD-probe data, the sample was characterized using THz-pump/800-nm probe techniques, in a setup similar to the one displayed in Fig. 3.4 and discussed in Section 3.4.2, with THz fields approximately equal to those produced by the tilted-pulse-front setup installed in the XPP hutch for the THz-pump/XRD-probe measurements. The 800 nm probe pulse was, like the THz probe pulse in the THz-pump/THz-probe measurements discussed previously, sensitive only to the conductivity response of the VO_2 thin film to THz pumping and therefore capable of monitoring only the electronic manifestations of the IMT. Following arrival of the THz pump, the transmission of the 800 nm probe pulse was observed to decrease, corresponding to increased sample reflectivity consistent with the appearance of the metallic phase (Fig. 6.14). In addition to confirming that THz driving of the IMT was possible in the sample, the THz-pump/800 nm-probe measurements also provided useful context for the THz-pump/XRD probe measurements described below, which will be elaborated upon later.

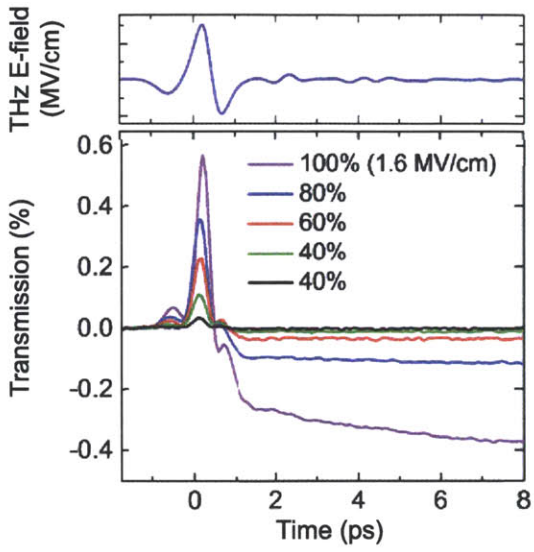

Figure 6.14. THz-pump/800 nm-probe data collected at 324 K at varying field strengths on 200 nm VO_2 thin film sample used for THz-pump/XRD-probe measurements, showing decrease in 800 nm transmission after THz pump arrival at t = 0, which indicates the appearance of the metallic phase. Data collection by A. X. Gray and M. C. Hoffmann; adapted from figure by A. X. Gray.

6.4.3

THz-Pump/XRD-Probe Measurements of the THz-Driven IMT in VO_2

To collect time-dependent XRD data, the peak intensities of the Bragg reflections corresponding to both the metallic and rutile phases were monitored as a function of pump/probe delay time. If the VO_2 film goes through the IMT beginning from an intermediate temperature, the lattice will begin with most unit cells in the insulating phase and end with most unit cells in the metallic phase. As this transition progresses, the amplitude of the reflection corresponding to the insulating phase is expected to decrease, and the amplitude of the reflection corresponding to the metallic phase is expected to undergo a corresponding increase, as the amplitude of a reflection is sensitive to the total number of unit cells which scatter in its specific direction. This was verified in static measurements (Fig. 6.15), where temperature-dependent XRD spectra showed a clear distinction between (002) Bragg reflections

corresponding to the insulating monoclinic and metallic rutile phases, which were separated by approximately 0.5° in θ. Once THz-induced dynamics were observed in the peak intensities of the rocking curves corresponding to each phase, full rocking curves were taken at varying THz-pump/XRD-probe time delays. The LCLS was tuned to 7 keV photon energy for all XRD measurements, and all detection was done using a Cornell-SLAC pixel array detector (CSPAD).

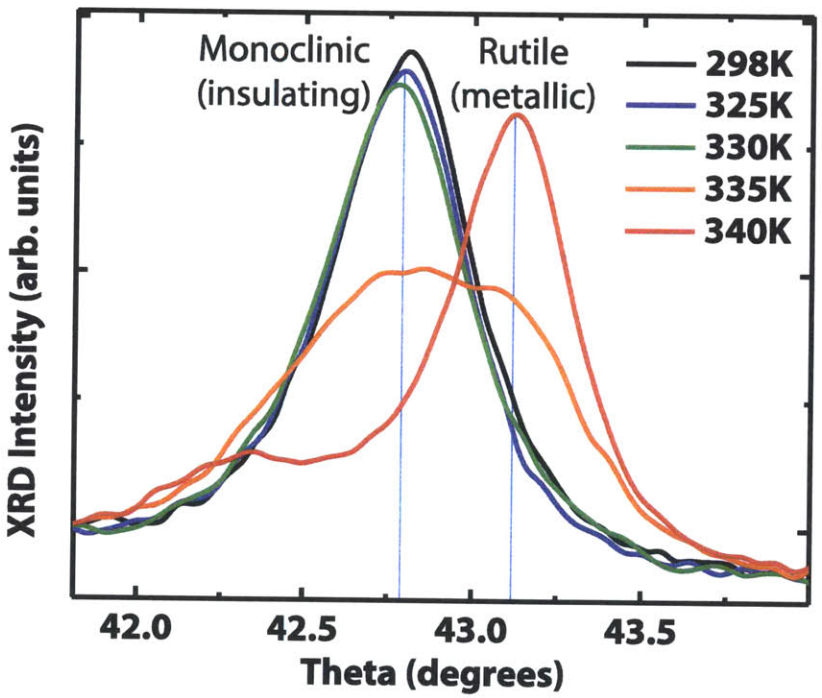

Figure 6.15. Static VO_2 rocking curves as a function of temperature, showing clear separation between low-temperature monoclinic (insulating) and high temperature rutile (metallic) phases. Figure by A. X. Gray.

With the sample temperature set to 324 K (the same temperature used in the tabletop THz-pump/THz-probe measurements described earlier), clear signatures of structural changes following THz excitation were observed, which correspond to the responses expected for the THz-driven IMT (Fig.

6.16). After the THz-pump/X-ray-probe overlap at t = 0, the intensity of the Bragg reflection corresponding to the insulating phase is observed to decrease. At the same time, the intensity of the Bragg reflection corresponding to the metallic phase increases, with similar dynamics. Both effects were observed to decay on nanosecond timescales. This is the first observation of long-lived ultrafast THz-driven structural dynamics with XRD probing. It is noteworthy that neither THz-driven phase transitions nor accessible femtosecond XRD probing of the resulting structural modulations were feasible until very recently.

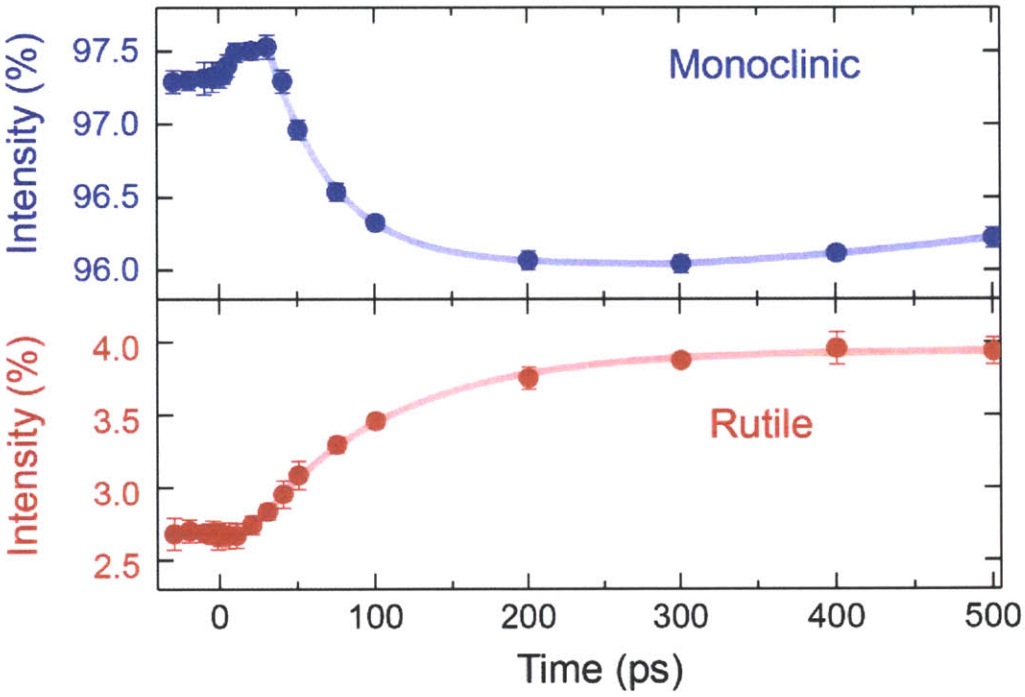

Figure 6.16. THz-pump/XRD probe data obtained for the monoclinic (insulating) and rutile (metallic) XRD peaks in 200 nm VO_2 on sapphire at 324 K, showing decrease in monoclinic peak intensity and corresponding increase in rutile peak intensity due to THz-driven IMT (peak intensity determined from full time-dependent rocking curve data sets through fits of rocking curves at each delay point). Figure by A. X. Gray.

Closer examination of the short-time dynamics for both peaks yields valuable information when compared to THz-pump/800 nm-probe scans taken on the same sample described earlier, as the 800 nm

probe pulse is only sensitive to the electronic manifestations of the IMT. The THz-pump/800 nm-probe results show that the onset of electronic dynamics of the THz-driven IMT is essentially instantaneous after pump/probe overlap at t = 0 (Fig. 6.17 (a)). However, the THz-pump/XRD-probe results show that there is an approximately 4 ps delay between the arrival of the THz pump and the onset of structural dynamics (Fig. 6.17 (b)). The ability to separate the heavily intertwined structural and electronic degrees of freedom associated with IMT allows for greater understanding of the underlying mechanism of the phase transition by considering each separately. The 4 ps delay associated with the onset of structural dynamics indicates that the electronic process associated with the phase transition begins first, in keeping with the mechanism suggested by the pure THz experiment described earlier, in which electrons are first liberated before lattice heating occurs. It is postulated that during this 4 ps delay, electrons are accelerated by the THz field, resulting in the immediate onset of the electronic manifestations of the phase transition as a result of THz-driven ionization processes. After the 4 ps time period, the structural dynamics associated with the transition begin, in which the dimerized V atoms begin to split.

6.4.4

VO_2 Conclusions and Outlook

The THz-pump/XRD-probe results discussed in the previous section are not only the first demonstration of ultrafast XRD probing of a THz driven phase transition, but also allow for new insight into the complicated nature of the IMT in VO_2 through separation of the electronic and structural degrees of freedom associated with the IMT when compared to THz-pump/THz-probe and THz-pump/800 nm-probe measurements. While the THz-pump/XRD-probe measurements reveal a great deal about the structural dynamics of the THz-driven IMT, the corresponding THz- and 800 nm-probe experiments are only sensitive to the overall conductivity of the sample. Further investigations into the

electronic dynamics of the THz-driven IMT are possible through X-ray absorption and X-ray emission spectroscopies (XAS and XES), which reveal changes in specific orbitals and are therefore potentially very useful given the nature of the IMT, which involves changes in specific molecular orbital energies. Preliminary XAS results relating to the V 3*d* orbitals were obtained in February, 2013; however, further refinement of the technique is necessary to yield useable data.

Further THz-pump/XRD-probe results were obtained in April, 2014 using samples consisting of 25 nm VO_2 films on TiO_2, in which the c_R axis was oriented in-plane, either parallel or perpendicular to the gold slit electrodes. The metamaterial design used was similar to the design used previously (Fig. 6.13), but had been adjusted slightly to give an enhancement factor of 7 rather than 4, as was used previously. The orientation of the c_R axis either parallel or perpendicular to the enhanced THz pump electric field was chosen to allow for investigation of the effect of the THz electric field direction on the phase transition as a function of its orientation relative to the dimerized V atoms in the monoclinic phase, which dimerize along the c_R axis (Fig. 6.11). Analysis of these results and their implications on the mechanistic picture presented here is ongoing; however, preliminary analysis shows a difference between the two orientations of the c_R axis. With c_R parallel to the THz electric field, a long-lived decrease in the monoclinic peak intensity and corresponding increase in the rutile peak intensity, similar to the previous results, is seen, but with a very fast onset. However, an initial decrease in the rutile peak intensity is seen if the THz electric field is oriented perpendicular to the c_R axis, warranting further analysis before interpretation of the mechanism responsible for the observed discrepancy is possible.

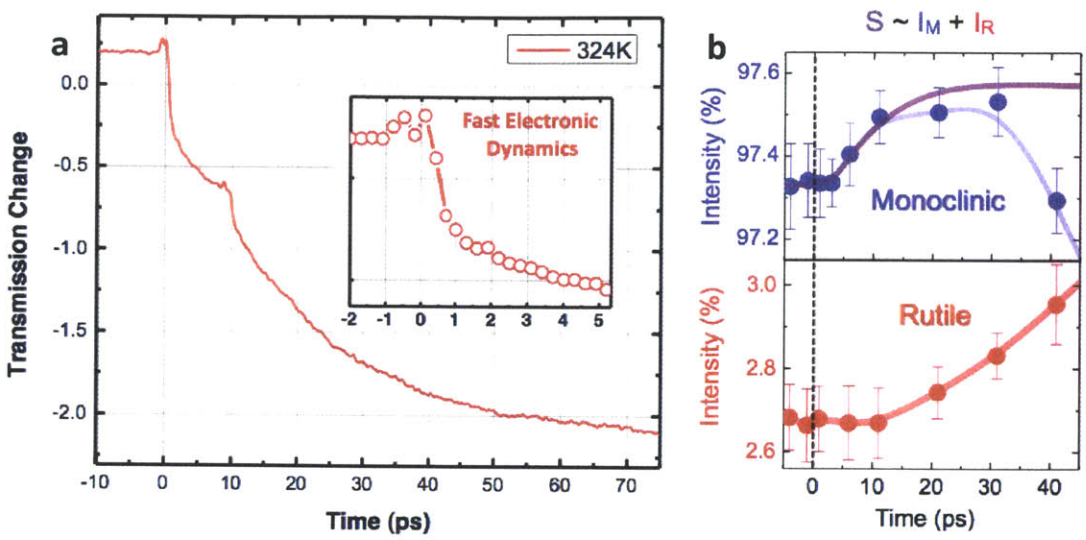

Figure 6.17. (a) THz-pump/800 nm-probe dynamics in 200 nm VO_2 on sapphire at 324 K, showing immediate onset of THz-driven electronic dynamics associated with the IMT, as shown in the inset, which displays a magnification of the data near the arrival of the THz pump at t = 0. The feature at ~ 10 ps is due to a second pass of the THz pulse through the VO_2 film after reflection from the back of the substrate. **(b)** THz-pump/XRD-probe results from Fig. 6.16 magnified, showing monoclinic (top) and rutile (bottom) fitted rocking curve intensities. Both monoclinic and rutile structural dynamics do not begin until 4 ps after the arrival of the THz pump at t = 0. This is revealed through the total structure factor *S* (the sum of the intensities of both rocking curves), as indicated at the top of the figure, which does not change until t = +4 ps. Note that the monoclinic peak intensity shows a transient increase before decreasing as the IMT progresses. Figure by A. X. Gray.

6.5

Ultrafast XRD Probing of Lattice Dynamics in Perovskite Ferroelectrics

[Note:

The measurements on $PbTiO_3$ presented here are the result of LCLS proposal L248, for which 60 hours of beamtime were obtained in October, 2010; results were published in 2012 (Daranciang, D., Highland, M. J., Wen, H., Young, S. M., **Brandt, N. C.**, Hwang, H. Y., Vattilana, M., Nicoul, M., Quirin, F., Goodfellow, J., Qi, T., Grinberg, I., Fritz, D. M., Cammarata, M., Zhu, D., Lemke, H. T., Walko, D. A., Dufresne, E. M., Li, Y., Larsson, J., Reis, D. A., Sokolowski-Tinten, K., Nelson, K. A., Rappe, A. M., Fuoss, P. H., Stephenson, B. G., Lindenberg, A. M., "Ultrafast photovoltaic response in ferroelectric nanolayers", *Phys. Rev. Lett.*, **108**, 087601 (2012)) and a summary appears in this section.

The results concerning $BaTiO_3$ were obtained during LCLS proposal LD06, for which 60 hours of beamtime were obtained in March, 2014; analysis in this case is ongoing.]

6.5.1

Ferroelectricity Background

Ferroelectric materials, which contain a macroscopic electric dipole, have attracted immense interest in recent decades due to their potential applications in next-generation memory applications. In particular, the perovskite class of crystals, characterized by the chemical formula ABO_3, in which A and B are metal cations, has been the subject of much study, as it contains many such materials and exhibits a relatively simple basic structural form[23]. Ferroelectricity arises in a typical perovskite material as a result of lattice distortions, in which the position of the small, highly charged B cation is displaced relative to the octahedron of oxygen atoms that surround it, leading to an asymmetric distribution of charge in the unit cell and the creation of a dipole in the unit cell (Fig. 6.18). The macroscopic ferroelectric dipole is obtained when the dipoles of many unit cells point in the same direction. The ferroelectric phase exists below a Curie temperature T_C, below which the displacement of the central ion becomes energetically favorable. Above T_C, the material exists in the paraelectric phase.

Interest in perovskite materials for use in memory applications stems from the ability to switch the direction of the ferroelectric dipole by applying an external electric field. The switching process involves motions of ions along the coordinate of a low frequency phonon, or soft mode, which corresponds to displacements of the atoms from their positions in one domain orientation into their positions in the new domain orientation, resulting in a reversal of the macroscopic dipole. These modes typically lie in the THz frequency range, which suggest that the switching, and hence memory operations dependent on it, could be accomplished at THz frequencies. As a result, the dynamics of the switching event are of great interest for future fast memory applications.

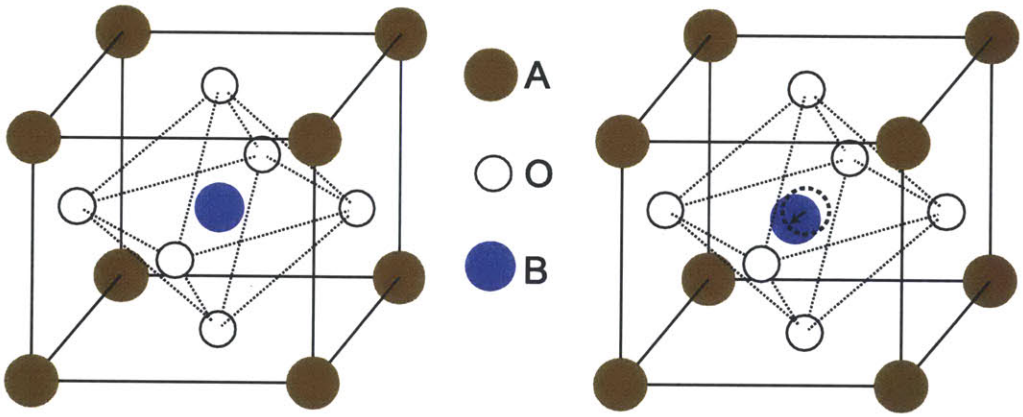

Figure 6.18. Perovskite unit cell in paraelectric (left) and ferroelectric (right) phases. The structural distortion shown in the ferroelectric phase is one of several possible such distortions; in this case, the central B ion is displaced from the center of the surrounding oxygen octahedron.

6.5.2

Femtosecond XRD Probing of Optically-Driven Responses in Lead Titanate

[Note: The discussion and figures here are a synopsis of the results obtained during LCLS proposal L248; a full discussion of the results may be found in Daranciang, D. el. al., "Ultrafast photovoltaic response in ferroelectric nanolayers", *Phys. Rev. Lett.*, **108**, 087601 (2012)]

Lead titanate ($PbTiO_3$ or PTO) exhibits a prototypical perovskite displacive-type ferroelectric transition at T_C = 766 K for bulk crystals[23]. When grown as a thin film, however, its ferroelectric behavior becomes significantly more complicated due to the presence of a depolarizing field. This field, which arises as a result of surface charge density, opposes the ferroelectric polarization and can have far-reaching effects on the morphology of the thin film[24–30]. In some cases, this leads to the formation of stripe domains, in which the film spontaneously forms stripes of alternating ferroelectric polarizations in order to reach an energetic minimum[26,27,31]. The destabilization effect of the depolarizing field in thin films, which is mediated by screening by surface adsorbates and free carriers[24,28], sets a lower limit for ferroelectric film dimensions, and as such is of high interest where memory applications, which rely upon miniaturization, are concerned.

The photovoltaic responses of perovskite ferroelectrics are also of interest for a number of reasons, including potential applications in solar cells, and the degree to which the depolarization interacts with these responses is an ongoing area of investigation. In order to investigate the transient structural component of the photovoltaic response in thin films of PTO, femtosecond XRD probing of PTO films following excitation with an ultrafast 400 nm pulse was conducted at the LCLS. The samples used were grown using chemical vapor deposition[32–34] and consisted of a 20 nm PTO film on a $SrTiO_3$ (STO) substrate and a 100 nm PTO film on a $DyScO_3$ (DSO) substrate. T_C for the former sample was 953 K,

while the latter had a much lower T_C of 743 K[35], with the large variations in T_C reflecting the degree of lattice mismatch between the film and the substrate, larger amounts of which increase strain and T_C in the case of the $SrTiO_3$-based sample. Ultrafast 400 nm-pump/XRD-probe measurements were made using frequency-doubled 800 nm pulses with durations of 40 fs and maximum incident fluences of 5 mJ/cm^2. XRD probing was done using the LCLS at 8.9 keV photon energy with 60 fs pulses. Further work was performed at the Advanced Photon Source, but was limited in time resolution due to the 100 ps pulse duration of the synchrotron-based X-ray pulses at that location.

Below T_C, the PTO/STO sample consists of ferroelectric PTO domains in which the *c* axis of the unit cell, which points along the ferroelectric dipole, is oriented in the out-of-plane direction[25,26,35]. As such, the (00*n*)-type Bragg reflections give information about the length of the *c* lattice parameter[36]. Time-dependent scans taken on the high-and low-angle sides of the (003) rocking curve show somewhat complicated dynamics, in which the rocking curve is first seen to shift to higher values of *Q* immediately after the arrival of the 400 nm pump pulse at t = 0, followed by a long-lived shift to lower *Q*, which persists for several nanoseconds (Fig. 6.19). The initial response corresponds to a decrease in the lattice parameter *c* (per Eq. 6.10), which is limited by the speed of sound (4000 m/s[37]) and the acoustic traversal time through the PTO film. The long-lived response corresponds to an expansion of the unit cell along the direction of the ferroelectric dipole. Note that this is contrary to the observed negative thermal expansion coefficient for PTO in this direction[25,26,35], and therefore cannot be explained by simple laser-driven heating.

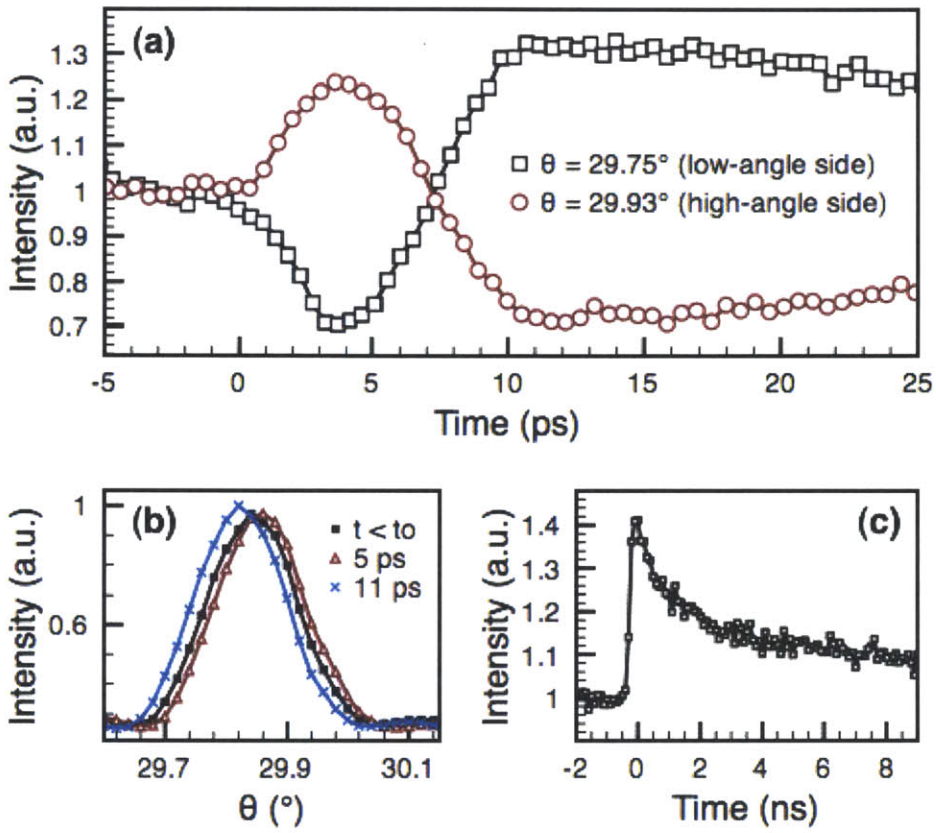

Figure 6.19. (a) Observed ultrafast responses of the low- and high-angle sides of the PTO (003) rocking curve after excitation with a 400 nm ultrafast pulse at t = 0. **(b)** Full rocking curves taken at various time delays. **(c)** Time scan taken on the low-angle side of the (004) PTO rocking curve at 350°C, showing nanosecond decay dynamics of the long-lived low-angle shift.

Further insight as to the nature of the observed ultrafast XRD signal in the PTO/STO sample can be obtained by raising the temperature to 535°C, at which point the PTO thin film enters a stripe domain[26], consisting of stripes of alternating ferroelectric polarization. The formation of a stripe domain is caused by the removal of surface adsorbates at higher temperatures, resulting in an altered free energy in which the strength of the depolarizing field relative to the energy associated with domain wall formation results in stripe formation[31]. The stripes give rise to a diffuse ring of X-ray scattering surrounding the PTO Bragg reflection, which has a radius given by

$$\Delta Q_r = \frac{2\pi}{\Lambda} \tag{6.16}$$

where Λ is the stripe periodicity (in this case approximately 10 nm). Measurement of the ring at varying delay times following an optical pump pulse using an X-ray area detector reveals dynamical responses of both the out-of-plane lattice constant as well as the stripe period that match the response seen in Fig. 6.19 (a) for the monodomain sample (Fig. 6.20). This result shows that the observed ultrafast structural response is independent of the specific ferroelectric domain morphology of the sample.

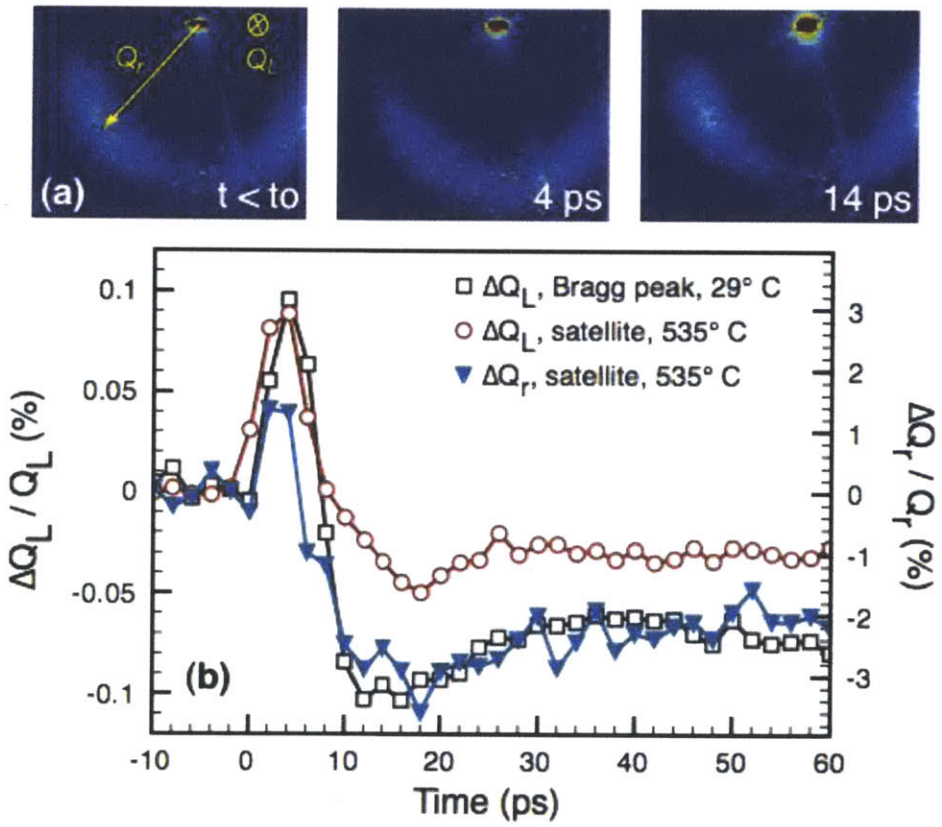

Figure 6.20. (a) Evolution of diffuse scattering ring corresponding to PTO stripe domain as a function of 400 nm-pump/XRD-probe time delay, detected with an X-ray area detector. **(b)** Time-dependent response of Q_L (the position of the diffuse scattering ring along the *L* axis in reciprocal space) and Q_r (the radius of the diffuse scattering ring) after 400 nm pump arrival at t = 0, showing similar dynamics to Fig. 6.19 (a).

Based on this information, the underlying mechanism is proposed to be the result of two factors that result from the displacement of electrons within the lattice and their resulting interaction with the electric fields present. The first part of the response, in which the lattice contracts along the *c* direction, is the result of a shift current. In this second-order response, the ultrafast 400 nm drives electrons away from their equilibrium positions, and the resulting asymmetric potential gives rise to a current, which is directed along the direction of the polarization and therefore acts with the depolarization field[38–40]. The transient increase in the depolarization field caused by the transient shift current is responsible for the observed lattice contraction. The second mechanistic step, which is responsible for the long-lived shift to low *Q* values as a result of lattice expansion, begins when the ultrafast laser pulse is no longer present. At this point, the photoexcited carriers stop acting with the depolarizing field and instead move to screen it. This results in a decrease in the depolarizing field, and therefore an increase in the ferroelectric polarization and an increase in the lattice constant in the direction of the ferroelectric dipole (the *c* direction). Figure 6.21 contains a schematic illustration of both mechanistic steps.

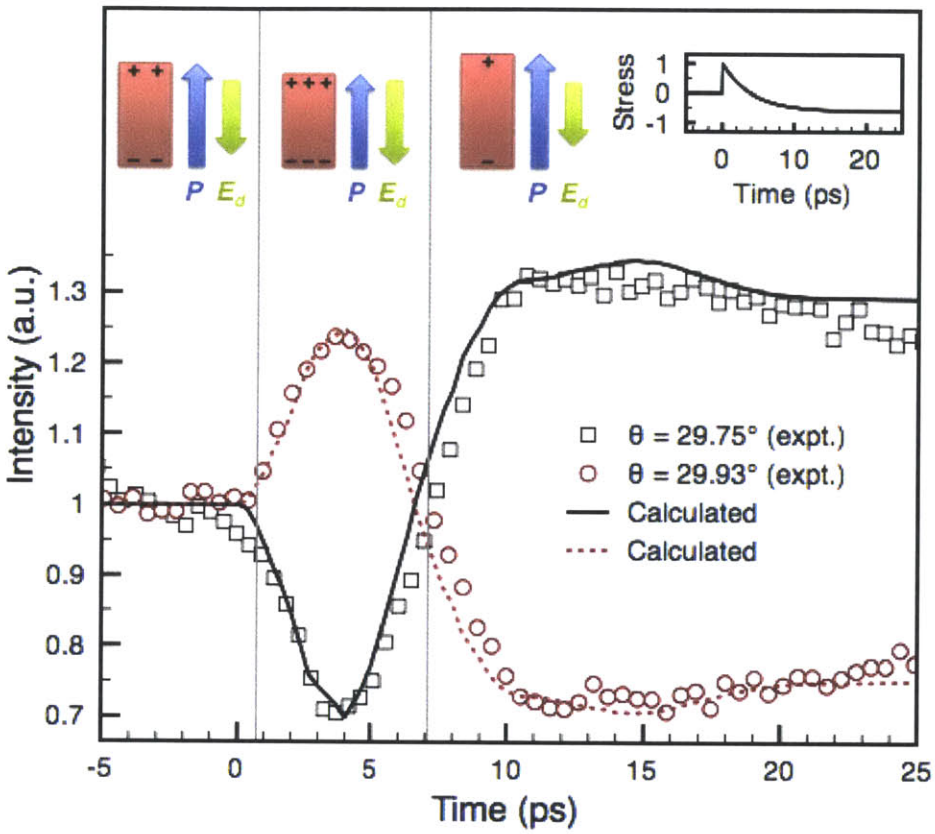

Figure 6.21. Illustration of proposed two-step mechanism plotted with data from Fig. 6.18 (a). At $t < 0$, the depolarization field E_d is represented by a green arrow, the ferroelectric polarization P is represented by a blue arrow, and the position of charges in the thin film is represented schematically in red. For $t < 10$ ps, photoexcited carriers produced by the arrival of the 400 nm pump at $t = 0$ act to increase E_d, leading to lattice contraction in the *c* direction as a result of the shift current, which reaches its fullest extent at approximately $t = 5$ ps. At $t > 10$ ps, the absence of the shift current allows the photoexcited carriers to instead screen E_d, leading to an increase in P and an expansion of the lattice in the *c* direction that lasts for the lifetime of the carriers. Data were fit by modeling the response of the lattice *c* parameter to the simulated time-dependent stress profile shown in the inset, which will be explained further in the text.

This is supported by the observed changes in the stripe periodicity, which reflects the degree of screening of the depolarizing field[24,27,28,30]. Furthermore, examination of the PTO/DSO sample above T_C, at which point the sample is in the paraelectric phase and the second-order shift current response is symmetry forbidden, shows no short-time dynamics. Further support for this mechanism is found through modelling of the expected response of the PTO lattice to the time-dependent strain expected as

a result of the photogenerated currents after 400 nm excitation. This is modeled as a time-dependent pressure using the acoustic wave equation solved for a thin film-substrate system, given by[41]

$$\sigma(t) = H(t)\left[\sigma_{SC} + \sigma_{DP}\left(1 - \exp(-t/\tau)\right)\right] \tag{6.16}$$

where *H(t)* is the Heaviside step function, σ_{SC} is an instantaneous stress, which corresponds to the shift current present immediately after 400 nm pumping, and σ_{DP} is a slowly increasing stress term which corresponds to the screening of the depolarization field by the photoinduced carriers after the shift current is no longer present. Equation 6.16 generates the time-dependent stress profile given in the inset of Fig. 6.21, and can be used to calculate simulated transient PTO (003) rocking curves, which can then be used to fit the time-dependent data shown in Fig. 6.19 (a). Fits appear in Fig. 6.21 and show excellent agreement to the experimental data.

The observed ultrafast structural responses of PTO thin films to 400 nm optical pumping show that the photovoltaic effects of 400 nm excitation result in transient currents, which add and subtract from the electric fields present in the lattice and in doing so modulate the unit cell dimensions that correspond to the ferroelectric polarization. In addition to being of value to future photovoltaic uses of ferroelectric thin films, these results demonstrate that femtosecond XRD probing at the LCLS can be used for direct observation of lattice modulations in ferroelectrics. This lays the groundwork for the observation of THz-driven structural responses in barium titanate, which are detailed in the next section.

6.5.3

Femtosecond XRD Probing of THz-Driven Structural Changes in Barium Titanate

(Ongoing as of May, 2014)

The discovery of ferroelectricity in barium titanate ($BaTiO_3$ or BTO) was a watershed moment for the field of ferroelectrics, as it was the first demonstration of ferroelectricity in a perovskite material, which exhibited a much simpler (and therefore easier to study) structure than any previously discovered ferroelectric[23]. BTO exhibits three ferroelectric phases, with tetragonal, orthorhombic, and trigonal symmetries and transition temperatures of 393, 278, and 183 K, respectively, for the onset of each phase as the temperature is lowered. In addition to the ferroelectric dipole present at temperatures beneath 393 K, BTO also exhibits the piezoelectric effect[42]. In order to study the highly coupled lattice motions in BTO, a 90 nm film of BTO on an $NdScO_3$ substrate was investigated using the THz-pump/XRD probe technique outlined earlier in this chapter, with essentially identical THz parameters as in the VO_2 measurements described in Section 6.4. The ferroelectric dipole in this sample was oriented in the out-of-plane direction, and all measurements were taken at room temperature.

Measurements of the intensity of the BTO (003) Bragg reflection rocking curve as a function of THz-pump/XRD-probe delay time show multiple effects. After THz pumping, a fast transient increase of the structure factor is observed, which lasts for no more than 10 ps. Following this structure factor modulation, a long-lived shift of the rocking curve to lower Q is seen through time-dependent scans of diffraction intensities on the high- and low-angle sides of the rocking curve (Fig. 6.22). This is indicative of expansive strain and corresponds to an expansion of the unit cell in the out-of-place direction (i.e. along the direction of the ferroelectric polarization). Longer time scans reveal that the effect persists for several nanoseconds. Differential rocking curves taken at varying time delays after the pump/probe overlap reveal that the shift is not perfectly symmetric, i.e. the shape as well as the position of the

rocking curve is modified by the THz field even when the initial structure factor modulation is no longer present (Fig. 6.23).

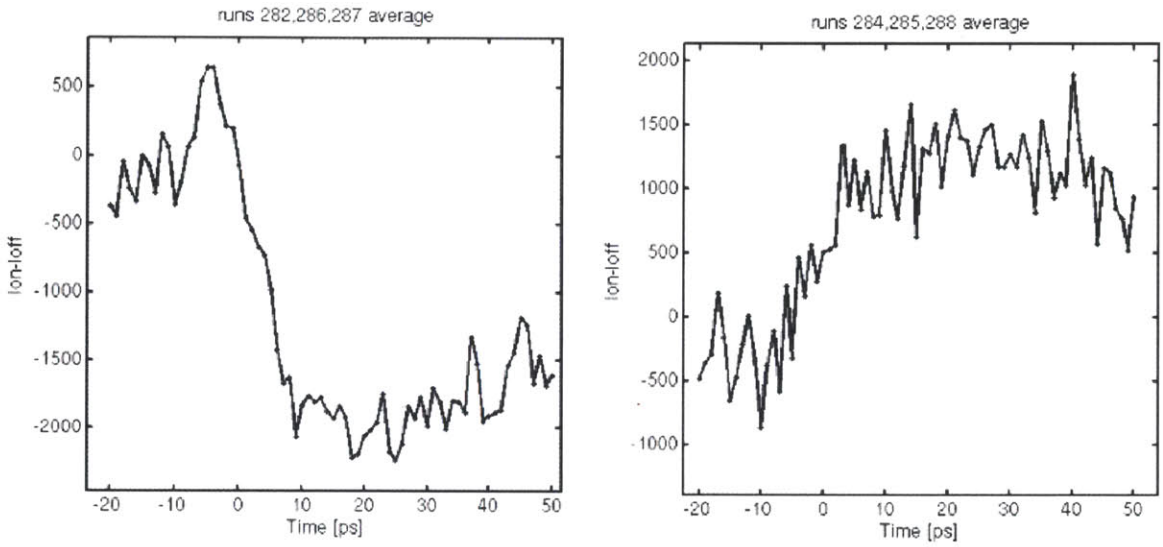

Figure 6.22. Response of high-angle side (left) and low-angle side (right) of BTO (003) rocking curve to THz pumping at t = 0, revealing transient shift of rocking curve to lower angles consistent with lattice expansion in the out-of-plane direction. The initial increase in the high-angle scan at t = 0 is the result of the short-lived structure factor modulation. Data analysis and plotting by F. Quirin and taken directly from experimental logbook.

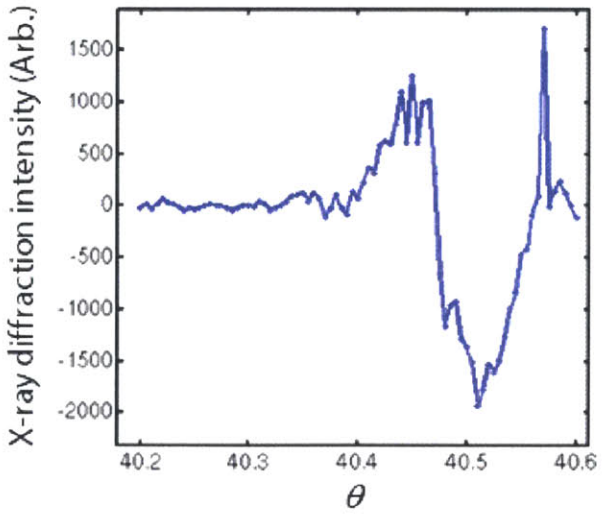

Figure 6.23. Differential BTO (003) rocking curve at t = +10 ps after the arrival of the THz pump pulse, showing transient shift to lower values of θ. Data analysis and plotting by F. Quirin and taken directly from experimental logbook.

Because the ferroelectric polarization is oriented in the out-of-plane direction, the observed effect cannot be the result of coupling between the THz pump field and the ferroelectric dipole directly. Therefore, the observed dynamics instead are the result of coupling to other lattice responses, possibly including piezoelectricity, absorption by lattice vibrations, or electrostriction, which lead to the observed long-lived response. Analysis and simulations to determine the underlying mechanism responsible for the observed dynamics is ongoing at this time.

6.6

Conclusions

X-ray diffraction has been recognized for 100 years as a powerful tool for investigating the arrangements of atoms in crystalline structures, and may now be used as an ultrafast probe of transient structural dynamics thanks to XFEL user facilities. In order to investigate THz-driven structural changes in various systems, a tilted-pulse-front source capable of THz peak fields exceeding 500 kV/cm was installed at the XPP instrument at the LCLS, which required a custom design capable of being integrated to the infrastructure necessary for femtosecond XRD probing. This setup has made possible the observation of THz-driven structural dynamics in both VO_2 and perovskite ferroelectrics, both of which are of high interest due to the fundamental issues they raise concerning the dynamics of coupled electronic/structural phase transitions and the ultimate time scales possible for ferroelectric phase transitions, as well as their application potential in next-generation devices. When carried out on thin films of VO_2, THz-pump/XRD-probe measurements reveal THz-driven structural dynamics consistent with reversible THz driving of the well-known insulator-to-metal phase transition in that material. When compared to THz-pump/800 nm-probe measurements taken under identical conditions, the timescales

of the highly intertwined electronic and structural components of the phase transition may be separated for the first time. Ultrafast XRD probing of lattice dynamics in perovskite ferroelectrics yields important information for both optically- and THz-driven structural responses. When pumped with 400 nm pulses, lead titanate reveals complicated structural dynamics associated with the generation and motion of photogenerated carriers. In barium titanate, a THz-driven structural response is observed, upon which analysis is ongoing but which shows promise for elucidating the ultimate limiting dynamics for electrically-driven responses in that material.

List of Collaborators

[Note: All collaborators for each proposal are shown, with results obtained in parenthesis for each proposal]

Proposal L248 (Photovoltaic response in PTO; October 2010)

SLAC/SIMES

Daranciang, D., Goodfellow, J., Reis, D., Lindenberg, A.

SLAC/LCLS

Fritz, D., Cammarata, M., Zhu, D., Lemke, H.

Argonne National Lab

Highland, M., Wen, H., Walko, D., Dufresne, E., Li, Y., Fuoss, P., Stephenson, B.

University of Pennsylvania

Young, S., Qi, T., Grinberg, I., Rappe, A.

MIT

Nelson, K., Hwang, H., Brandt, N.

University of Duisberg-Essen

Vattilana, M., Nicoul, M., Quirin, F., Sokolowski-Tinten, K.

Lund University

Larsson, J.

Proposal L702 (VO_2; first set of measurements; February 2013)

SLAC/SIMES

Gray, A., Durr, H., Deveraux, T., Reid, A., Sorini, A., Kukreja, R., Graves, C., Wang, T.

SLAC/LCLS

Stohr, J., Hoffman, M., Zhu, D., Schlotter, W.

SLAC/SSRL

Weng, T.-C., Nordlund, D., Ohldag, H., Sokaras, D.

MIT

Nelson, K., Hwang, H., Brandt, N. Hofmann, F.

Boston University

Averitt, R., Liu, M., Abreu, E., Sternbach, A.

IBM Almaden

Parkin, S., Samant, M., Aetukuri, N. P., Jeong, J.

Argonne National Lab

Freeland, J., Wen, H., Zhu, Y.

Proposal LD06 (THz-driven dynamics in BTO; March 2014)

SLAC/SIMES

Chen, F., Goodfellow, J., Shu, M., Zalden, P., Lindenberg, A.

SLAC/LCLS

Hoffmann, M., Zhu, D., Lemke, H., Chollet, M.

Argonne National Lab

Highland, M., Wen, H., Zhu, Y., Fuoss, P., Stephenson, B.

University of Pennsylvania

Young, S., Zheng, F., Liu, S., Grinberg, I., Rappe, A.

MIT

Nelson, K., Hwang, H., Brandt, N., Lu, J.

University of Duisberg-Essen

Quirin, F., Sokolowski-Tinten, K.

Lund University

Larsson, J.

University of Illinois

Damodaran, A., Martin, L.

Proposal LC70 (VO_2; second set of measurements; April 2014)

SLAC/SIMES

Gray, A., Durr, H., Reid, A., Bonetto, S., Trigo, M., Granitzka, P., Kukreja, R., Graves, C., Chen, J., Zwartzenberg, B., Devereaux, T., Moritz, B.

SLAC/LCLS

Stohr, J., Hoffman, M., Zhu, D., Chollet, M.

SLAC/SSRL

Weng, T.-C., Nordlund, D., Ohldag, H., Sokaras, D.

MIT

Nelson, K., Hwang, H., Brandt, N. Lu, J.

Boston University

Averitt, R., Abreu, E.,

UC San Diego

Liu, M., Sternbach, A.

IBM Almaden

Parkin, S., Samant, M., Aetukuri, N. P., Jeong, J.

Argonne National Lab

Freeland, J., Wen, H., Zhu, Y.van Veenendaal, M., Cheng-Chien, C.

References

1. Qi, T., Shin, Y.-H., Yeh, K.-L., Nelson, K. & Rappe, A. Collective coherent control: synchronization of polarization in ferroelectric $PbTiO_3$ by shaped THz fields. *Phys. Rev. Lett.* **102,** 247603 (2009).

2. Liu, M. *et al.* Terahertz-field-induced insulator-to-metal transition in vanadium dioxide metamaterial. *Nature* **487,** 345 (2012).

3. Feldhaus, J., Arthur, J. & Hastings, J. B. X-ray free-electron lasers. *J. Phys. B At. Mol. Opt. Phys.* **38,** S799 (2005).

4. McNeil, B. W. J. & Thompson, N. R. X-ray free-electron lasers. *Nat. Photonics* **4,** 814 (2010).

5. Emma, P. *et al.* First lasing and operation of an angstrom-wavelength free-electron laser. *Nat. Photonics* **4,** 641 (2010).

6. Hada, M., Pichugin, K. & Sciaini, G. Ultrafast structural dynamics with table top femtosecond hard X-ray and electron diffraction setups. *Eur. Phys. J. Spec. Top.* **222,** 1093 (2013).

7. Waseda, Y., Matsubara, E. & Shinoda, K. *X-Ray Diffraction Crystallography*. (Springer-Verlag Berlin Heidelberg, 2011).

8. Freidrich, W., Knipping, P. & von Laue, M. Interferenzerscheinungen bei Rontgenstrahlen. *Ann. Phys.* **346,** 971 (1913).

9. Alloul, H. *Introduction to the Physics of Electrons in Solids*. (Springer-Verlag Berlin Heidelberg, 2011).

10. Suryanarayana, C. & Grant Norton, N. *X-Ray Diffraction*. (Plenum Press, 1998).

11. Helliwell, J. R. in *Int. Tables Crystallogr. Vol. C Math. phyiscal, Chem. tables* (Prince, E.) **C,** 26 (Springer Netherlands, 2006).

12. Daranciang, D. Ultrafast Photovoltaic Responses in Ferroelectric Thin Films. (2012).

13. Klug, H. P. & Alexander, L. E. *X-Ray Diffraction Procedures*. (John Wiley & Sons, Inc., 1954).

14. LCLS Parameters. (2014). at <https://portal.slac.stanford.edu/sites/lclscore_public/Accelerator_Physics_Published_Documents/LCLS-parameters.pdf>

15. Glownia, J. M. *et al.* Time-resolved pump-probe experiments at the LCLS. *Opt. Express* **18,** 17620–30 (2010).

16. Morin, F. J. Oxides which show a metal-to-insulator transition at the Neel temperature. *Phys. Rev. Lett.* **3,** 34 (1959).

17. Goodenough, J. B. The two components of the crystallographic transition in VO_2. *J. Solid State Chem.* **3,** 490 (1971).

18. Eyert, V. The metal-insulator transitions of VO_2 : A band theoretical approach. *Ann. Phys.* **11,** 650 (2002).

19. Haverkort, M. W. *et al.* Orbital-assisted metal-insulator transition in VO_2. *Phys. Rev. Lett.* **95,** 196404 (2005).

20. Koethe, T. C. *et al.* Transfer of spectral weight and symmetry across the metal-insulator transition in VO_2. *Phys. Rev. Lett.* **97,** 116402 (2006).

21. Berglund, C. N. & Guggenheim, H. J. Electronic properties of VO_2 near the semiconductor-metal transition. *Phys. Rev.* **185,** 1022 (1969).

22. Quackenbush, N. F. *et al.* Nature of the metal insulator transition in ultrathin epitaxial vanadium dioxide. *Nano Lett.* **13,** 4857 (2013).

23. Lines, M. E. & Glass, A. M. *Principles and Applications of Ferroelectrics and Related Materials*. (J. W. Arrowsmith Ltd., 1977).

24. Spanier, J. E. *et al.* Ferroelectric phase transition in individual single-crystalline $BaTiO_3$ nanowires. *Nano Lett.* **6,** 735 (2006).

25. Fong, D. *et al.* Stabilization of monodomain polarization in ultrathin $PbTiO_3$ films. *Phys. Rev. Lett.* **96,** 127601 (2006).

26. Streiffer, S. *et al.* Observation of nanoscale 180° stripe domains in ferroelectric $PbTiO_3$ thin films. *Phys. Rev. Lett.* **89,** 067601 (2002).

27. Prosandeev, S. & Bellaiche, L. Asymmetric screening of the depolarizing field in a ferroelectric thin film. *Phys. Rev. B* **75,** 172109 (2007).

28. Chisholm, M. F., Luo, W., Oxley, M. P., Pantelides, S. T. & Lee, H. N. Atomic-scale compensation phenomena at polar interfaces. *Phys. Rev. Lett.* **105,** 197602 (2010).

29. Lichtensteiger, C., Triscone, J.-M., Junquera, J. & Ghosez, P. Ferroelectricity and tetragonality in ultrathin $PbTiO_3$ films. *Phys. Rev. Lett.* **94,** 047603 (2005).

30. Batra, I. P., Wurfel, P. & Silverman, B. D. Phase transition, stability, and depolarization field in ferroelctric thin films. *Phys. Rev. B* **8,** 3257 (1973).

31. Fong, D. D. *et al.* Ferroelectricity in ultrathin perovskite films. *Science* **304,** 1650 (2004).

32. Murty, M. V. R. *et al.* In situ x-ray scattering study of $PbTiO_3$ chemical-vapor deposition. *Appl. Phys. Lett.* **80,** 1809 (2002).

33. Koster, G., Kropman, B. L., Rijnders, G. J. H. M., Blank, D. H. A. & Rogalla, H. Quasi-ideal strontium titanate crystal surfaces through formation of strontium hydroxide. *Appl. Phys. Lett.* **73,** 2920 (1998).

34. Kleibeuker, J. E. *et al.* Atomically defined rare-earth scandate crystal surfaces. *Adv. Funct. Mater.* **20,** 3490 (2010).

35. Pertsev, N. A., Zembilgotov, A. G. & Tagantsev, A. K. Effect of mechanical boundary conditions on phase diagrams of epitaxial ferroelectric thin films. *Phys. Rev. Lett.* **80,** 1988 (1998).

36. Fong, D. *et al.* Direct structural determination in ultrathin ferroelectric films by analysis of synchrotron x-ray scattering measurements. *Phys. Rev. B* **71,** 144112 (2005).

37. Li, Z., Grimsditch, M., Xu, X. & Chan, S.-K. The elastic, piezoelectric and dielectric constants of tetragonal $PbTiO_3$ single crystals. *Ferroelectrics* **141,** 313 (1993).

38. Côté, D., Laman, N. & van Driel, H. M. Rectification and shift currents in GaAs. *Appl. Phys. Lett.* **80,** 905 (2002).

39. Nastos, F. & Sipe, J. E. Optical rectification and current injection in unbiased semiconductors. *Phys. Rev. B* **82,** 235204 (2010).

40. Young, S. M. & Rappe, A. M. First principles calculation of the shift current photovoltaic effect in ferroelectrics. **109,** 116601 (2012).

41. Nicoul, M., Shymanovich, U., Tarasevitch, A., von der Linde, D. & Sokolowski-Tinten, K. Picosecond acoustic response of a laser-heated gold-film studied with time-resolved x-ray diffraction. *Appl. Phys. Lett.* **98,** 191902 (2011).

42. Berlincourt, D. & Jaffe, H. Elastic and piezoelectric coefficients of single-crystal barium titanate. *Phys. Rev.* **111,** 143 (1958).

Chapter 7

Outlook and Conclusions

The work presented thus far in this thesis shows that nonlinear THz spectroscopy can be applied to a broad range of systems. By using tilted-pulse-front THz generation in combination with metamaterial-driven field enhancement and instruments designed for efficient collection and focusing of tilted-pulse-front based sources, nonlinear THz spectroscopy can be effectively implemented for many different sample types in a flexible, versatile instrument which may be easily configured for a wide variety of experimental techniques based on high-field THz pumping.

Chapter 4 demonstrated that metamaterial enhancement, when coupled with appropriately high fields, can be used to drive nonlinear THz interactions in materials previously unknown to exhibit anything but a linear response in the THz range through the demonstration of impact ionization in high-resistivity silicon wafers. Furthermore, moving to more complex metamaterial geometries demonstrated that the THz magnetic field is as capable as the THz electric field at driving nonlinear responses. Finally, it was suggested that the nonlinear responses in different capacitive gaps in complex 3D metamaterial structures could be selectively excited through sample positioning in the THz focus, suggesting that a degree of selectivity could be possible on this basis for nonlinear responses.

Chapter 5 demonstrated that not only could metamaterial-enhanced THz fields drive nonlinear responses in materials previously lacking them, but also that metamaterial-enabled nonlinear THz responses are in some cases dependent on the structure and composition of the metamaterial itself. In

this case, air ionization between the gold electrodes in etched-gap SRRs was observed, which depends not only on THz-driven impact ionization in the air between the gold electrodes but also on the presence of the gold antenna, which serves as a necessary source of electrons for the breakdown process through the secondary electron emission and field emission processes. This was further demonstrated at low pressures, in which current flow across the SRR antenna gap is definitive evidence of THz-driven electron emission from the gold electrodes. Finally, the observation of electromigration in the gold SRR structures as a result of THz irradiation shows that metamaterial-coupled THz fields are not only capable of causing damage to the sample within the enhancing antenna gap but also to the enhancement structure itself.

Chapter 6 shows that THz-driven structural changes can be driven to high enough amplitudes to be seen with ultrafast X-ray diffraction. In the case of vanadium dioxide, ultrafast THz pumping results in X-ray dynamics consistent with the material being driven through the insulator-to-metal phase transition. Critically, this manifests itself with different dynamics than were observed in the case of optical or THz probing after THz pumping, allowing for separation of the previously intertwined structural and electronic degrees of freedom associated with the phase transition. X-ray probing of lattice dynamics in ferroelectric crystals was also demonstrated, first through observation of optically-driven structural changes due to photovoltaic effects in lead titanate, and then through THz-driven structural changes in barium titanate, for which analysis is ongoing.

This chapter presents preliminary results of additional experiments that further the advance of nonlinear THz spectroscopy into new regimes. This includes using SRR structures to drive chemistry in organic materials, probing nonlinear THz interactions with impulsive stimulated Raman scattering (ISRS), examination of the Stark effect at THz frequencies, and applying THz pulses to shock-induced energetic material decomposition.

7.1

THz-Driven Energetic Material Decomposition

7.1.1

Energetic Material Background

In addition to the semiconductor, gaseous, and inorganic ceramic samples to which nonlinear THz spectroscopy has been applied thus far in this thesis, molecular crystals comprise another class of systems that exhibit potentially interesting dynamics at THz frequencies. Many molecular crystals contain several lattice vibrations within the bandwidth of a typical free-space THz source, which arise from collective intermolecular motions. In many cases, these motions are coupled to or contain significant contributions from intramolecular motions such as bond stretching and wagging. Significant interest has been generated in the coupling of these motions to one another, as energy transfer between THz-active vibrations could provide key insights into the chemistry of molecular crystals.

Of particular interest in this area is the coupling of THz-active lattice motions in energetic materials, in which vibrational up-pumping is theorized to be the underlying mechanism responsible for detonation[1,2]. Key to this mechanism is the transfer of energy from lattice vibrations to the intramolecular vibrational manifold, for which THz-frequency "doorway modes" are expected to play key roles[3]. As a result, nonlinear THz spectroscopy presents an ideal tool for the probing of the THz-frequency vibrations and their couplings that are critically important to the proposed up-pumping mechanism. Significant attention has been given to RDX (cyclotrimethylenetrinitramine; Fig. 7.1) as a result of its widespread use in high explosive formulations. RDX exhibits several low-frequency phonon modes in the THz frequency range. Chief among these is a strong absorption at 0.8 THz[4], which is very close to the typical frequency maxima for the tilted-pulse-front THz source described in Chapter 2 (Fig.

2.3) and therefore is an ideal candidate for investigations of the low-frequency mode couplings in RDX through nonlinear THz spectroscopy.

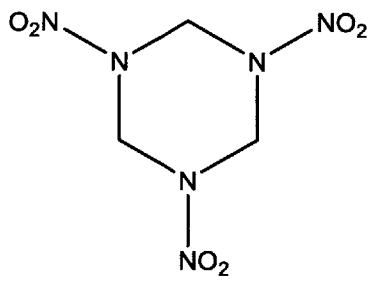

Figure 7.1. Molecular structure of RDX (cyclomethylenetrinitramine).

7.1.2

Applying Metamaterial-Driven Field Enhancement to RDX

The SiN_x-based metamaterial SRR arrays used for the breakdown measurements in Chapter 5 (obtained through collaboration with the Boston University Photonics Center) function as a platform for the application of SRR-enhanced free space THz fields to arbitrary materials as a result of their unique substrate characteristics. Briefly, the samples employed in Chapter 5 are gold SRR arrays patterned onto free-standing 400 nm thick SiN_x films[5]. The SiN_x substrate beneath each capacitive gap of the four-sided SRR structure is removed using reactive ion etching, yielding a void beneath each antenna gap into which any arbitrary sample may be inserted (Fig. 7.2 (a)). As a result, this class of structures shows great promise for expanding the range of materials to which metamaterial-enhanced nonlinear THz spectroscopy may be employed.

In order to utilize SRR field enhancement for nonlinear vibrational excitation of RDX, samples were obtained in which the SRR LC resonance was tuned to match the 0.8 THz RDX phonon absorption. In order to physically place RDX into the capacitive gaps, 10 microliters of a saturated solution of RDX in

N,N-dimethylformamide was applied to the reverse side of the SiN_x substrate of the SRR array. Slow evaporation over a 24 hour period yielded small RDX crystals in each SRR capacitive gap, which were observed to be the result of the growth of a single large crystal on the reverse side of the SRR array substrate, which then grew into each gap during the evaporation process (Fig. 7.2 (b)).

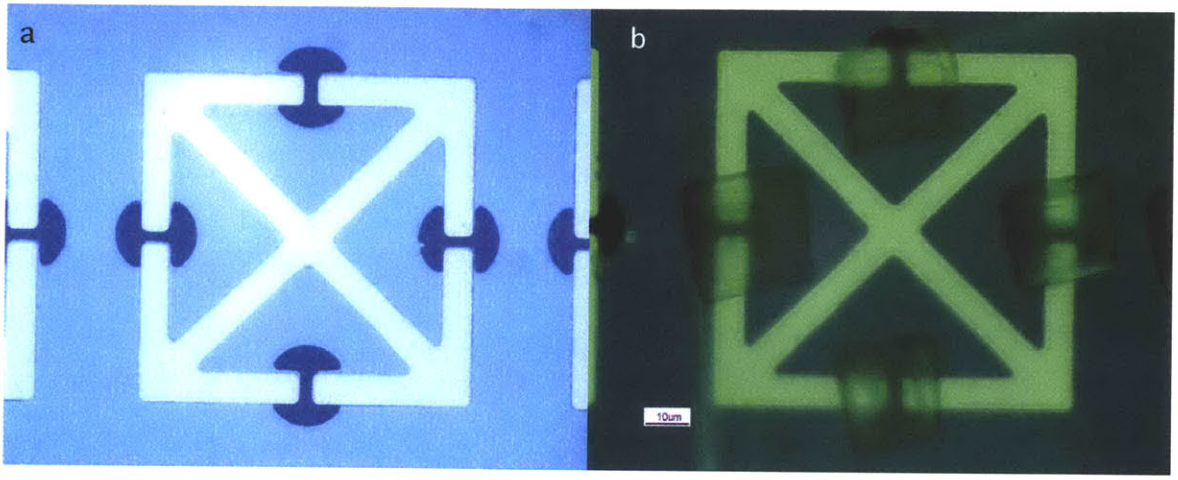

Figure 7.2. (a) SRR arrays on a 400 nm SiN_x substrate in which the SiN_x substrate has been removed from beneath each SRR capacitive gap using an etching process. **(b)** SRR arrays after deposition and evaporation of a saturated solution of RDX to the reverse side of the substrate, resulting in the growth of small RDX crystals into each capacitive gap.

7.1.3

THz-Driven RDX Removal from SRR Arrays

RDX-infused SRR arrays were irradiated with THz fields of approximately 375 kV/cm at 500 Hz repetition rate for six hours using the collinear THz-pump/THz-probe instrument described in Chapter 3 (in this case, the older version with 2 inch diameter OAP reflectors, described in Section 3.3, was employed). Examination of the RDX crystals within each SRR capacitive gap via optical microscopy before and after the THz irradiation period shows dramatic THz-induced damage to the RDX crystals, with circular holes (corresponding to the area of the substrate etching beneath each gap) appearing in

crystals that were in THz-resonant capacitive gaps (Fig. 7.3 (a)). In many cases, the crystalline material is essentially completely removed. Furthermore, RDX crystals in gaps that were not resonant with the incident vertically polarized THz pulse show no damage at all. Examination of the reverse side of the sample reveals that the circularly-shaped THz-driven RDX removal extends in some cases throughout the entirety of the much larger RDX crystal on the reverse side of the sample (Fig 7.3 (b)). THz transmission spectra taken before and after the irradiation period reveal signatures consistent with complete RDX removal (Fig. 7.4).

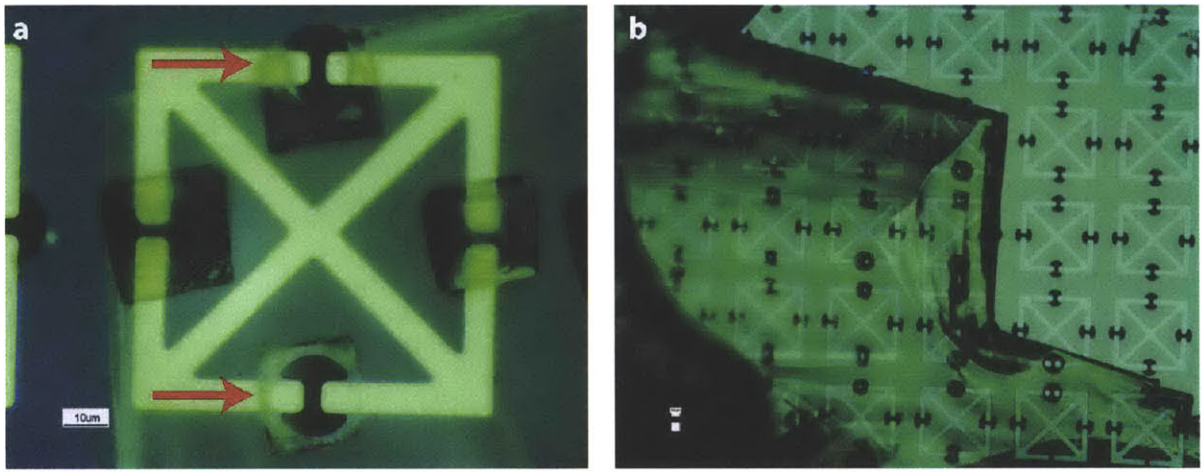

Figure 7.3. (a) THz-induced removal of RDX crystals from SRR capacitive gaps, showing near-complete removal of RDX from gaps aligned with the polarization of the incident THz pump pulse (top and bottom gaps; indicated by red arrows), and no effect on gaps perpendicular to the THz polarization (left and right gaps). The THz polarization was parallel to the horizontal direction in this case. **(b)** Reverse side of the THz-damaged RDX-impregnated SRR array, showing clean removal of the RDX beneath the SRR capacitive gaps in some cases.

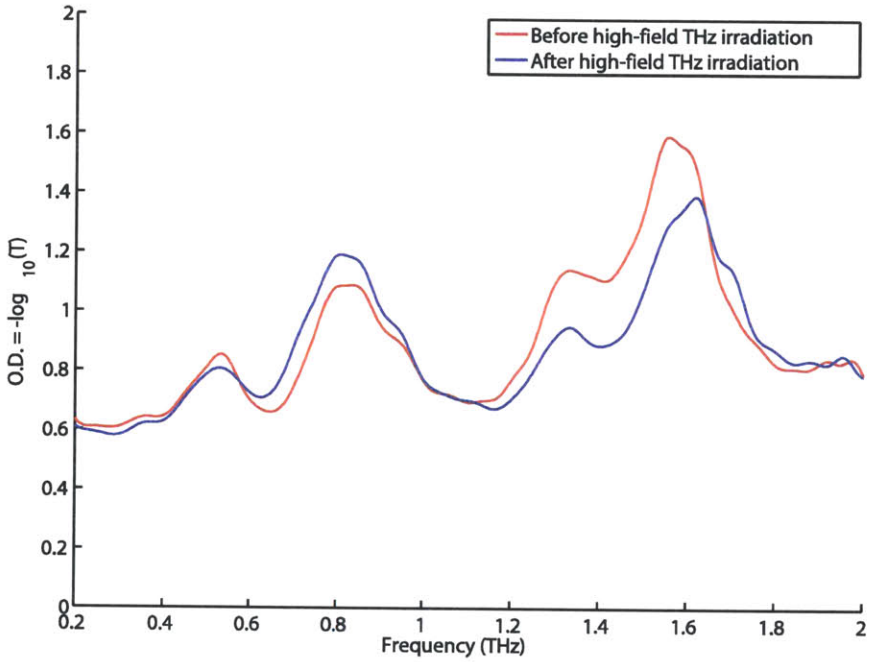

Figure 7.4. Transmission spectra taken before and after THz-induced damage to RDX-impregnated SRR array, showing decrease in RDX phonon absorptions at 0.6, 1.3, and 1.6 THz, and increase in LC resonance absorption at 0.8 THz after THz-induced damage. This is consistent with the removal of RDX from the capacitive gaps.

7.1.4

Analysis of RDX Removal

Examination of the THz-damaged RDX crystal remnants through both Raman and FTIR microscopy was performed in an attempt to detect and characterize possible decomposition products, in order to yield insight into the mechanism of the damage process. Raman microscopy of the capacitive gaps in which THz-induced damage occurred yielded no Raman signal, indicating that the RDX was cleanly removed. Furthermore, comparison of the remaining areas of THz-damaged RDX crystals to adjacent undamaged crystals in capacitive gaps that were not resonant with the incident THz pulse showed identical Raman and FTIR spectra, indicating that very little or no decomposition products

remained on the sample. When considered together, this evidence indicates that the RDX was either decomposed into gas phase species or possibly removed intact into the gas phase.

Based on the evidence pointing to a gas phase process, attempts to identify possible RDX decomposition products were undertaken using solid phase microextraction (SPME), which is a collection method designed for gas- and solution-phase analytes. In the SPME process, a small adsorbent fiber is used to collect analytes, which may then be analyzed via mass spectrometry or chromatography[6]. In this case, SPME collection was performed using an 85 μm polyacrylate fiber in accordance with previously published SPME sampling of RDX headspaces[7], and analysis of adsorbed analytes was accomplished through gas chromatography/mass spectrometry (GC/MS).

GC/MS analysis of SPME-collected species during ten hours of THz irradiation of an RDX-impregnated SRR array (referred to as the "decomposition run" hereafter) showed preliminary evidence of THz-generated gas phase species when compared to SPME-collected species from an identical sample over a similar time period with no THz irradiation present (referred to as the "control run"). Examination of the control run chromatograph (Fig 7.5) shows a large peak at 15.10 min. elution time, which can be assigned to RDX on the basis of its mass spectrum (not shown), as well as several peaks that elute at earlier times. Critically, very few significant peaks are observed to elute after the RDX peak. In contrast, the chromatograph obtained for analytes collected during the decomposition run shows a large number of peaks eluting after the RDX peak, which may be due to THz-driven RDX decomposition products. If so, this forms the first evidence of a THz-driven chemical reaction.

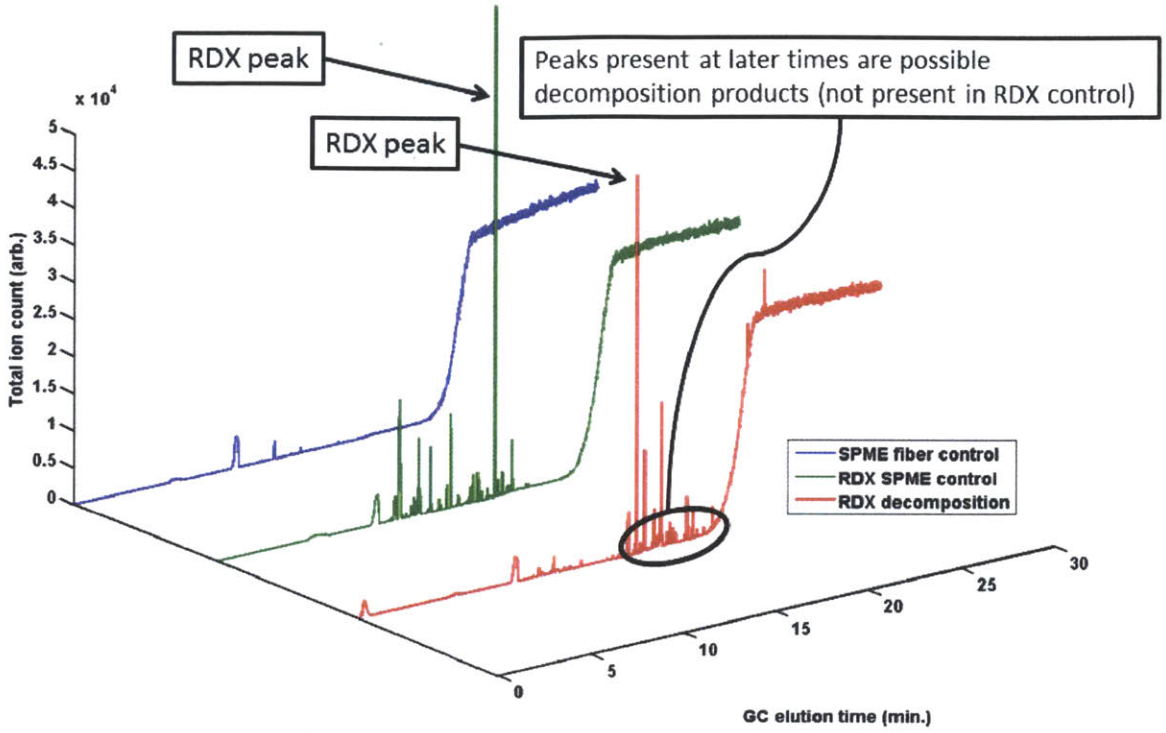

Figure 7.5. Results of SPME/GC/MS analysis of THz-driven RDX decomposition, showing presence of GC peaks that may correspond to RDX decomposition products.

Examination of the timescale of the THz-driven damage was accomplished through imaging of the RDX-impregnated SRR array during the THz irradiation period using an LED lightsource. Images obtained at 30 second intervals during the irradiation period reveal a slow, gradual disappearance of RDX crystals in the SRR capacitive gaps (Fig. 7.6). This was further confirmed through collection of the transmitted THz waveform during the collection period. Analysis of THz waveforms collected continually throughout the irradiation period shows a similar gradual change.

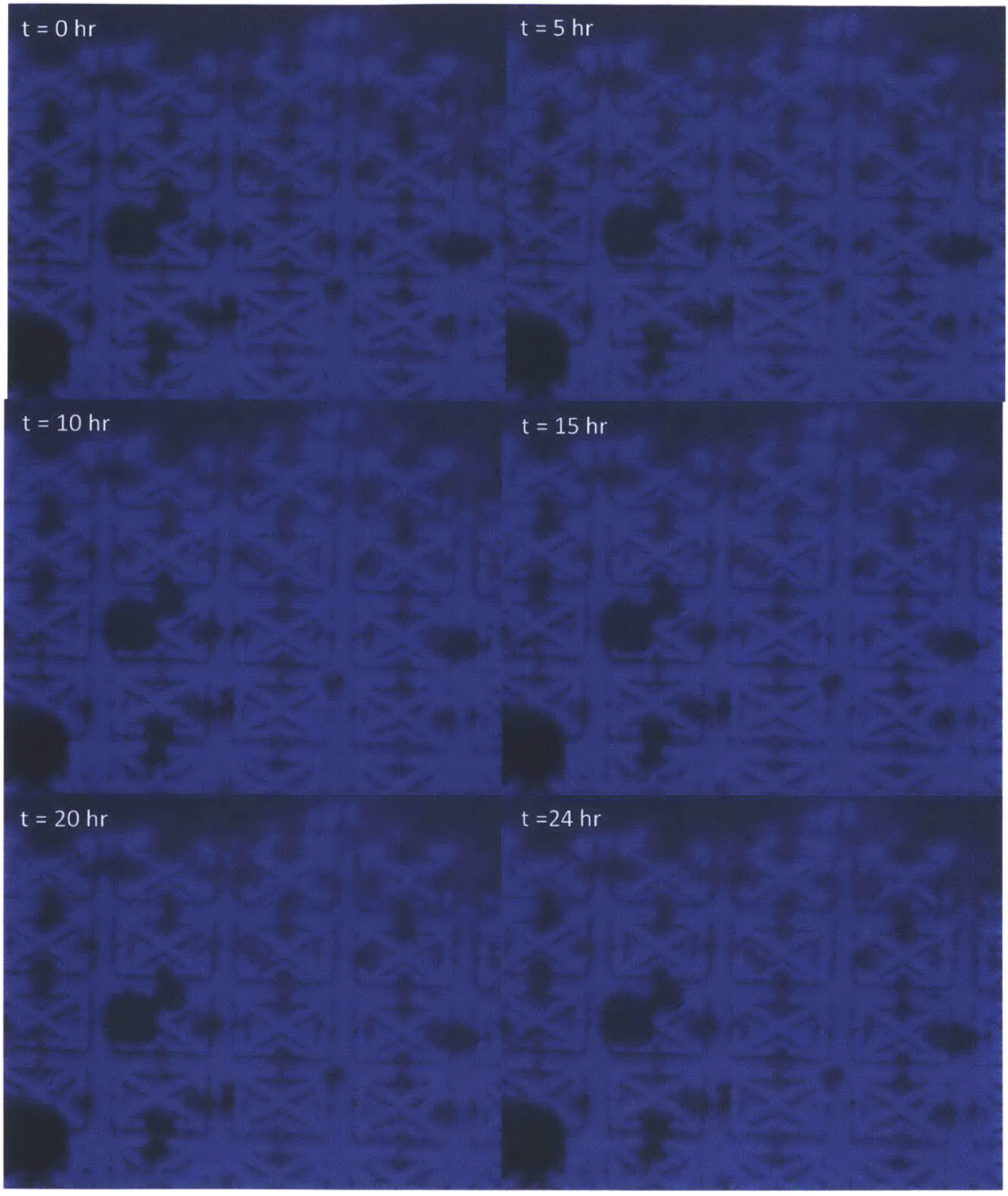

Figure 7.6. Images of RDX-impregnated SRR sample during THz irradiation, showing gradual disappearance of RDX crystals from SRR capacitive gaps as a function of THz irradiation time in hours.

Finally, replication of the experiment with crystalline acetanilide, which has no phonon absorptions within the bandwidth of the tilted-pulse-front based THz pulse used for irradiation, showed a nearly identical damage pattern (Fig. 7.7). This suggests that the decomposition observed in both RDX and acetanilide stems from a common cause. Furthermore, the lack of THz absorptions within the bandwidth of the THz source in the case of acetanilide implies that the decomposition is not due to a phonon-mediated process.

Figure 7.7. THz-induced damage pattern in acetanilide crystals on SRR arrays, showing identical damage pattern to the RDX damage in Fig. 7.3.

7.1.5

Discussion of RDX Removal Mechanism

Despite the lack of chemical evidence of decomposition products, the above analyses give several insights into the underlying removal mechanism:

- RDX is either removed intact into the gas phase or decomposed into gaseous products
- RDX is removed gradually over several hours of THz irradiation

- The effect is likely not a phonon-mediated process

Taken together, these factors point toward two possible removal mechanisms, namely that the RDX is removed thermally as a result of THz-driven RDX heating, or that it is removed as a result of electron acceleration in the RDX crystal under the enhanced THz fields. The results presented in Chapter 5, which show that significant electron emission from the gold SRR antennas is expected through the field emission process, lends support to the latter scenario. However, thermally driven decomposition cannot be ruled out, especially as it has been experimentally verified to be accompanied by RDX sublimation at atmospheric pressure[8]. As a result, further investigations into the temperature change experienced by the RDX crystals in the capacitive gaps are needed, along with additional experimental attempts at identifying the potential decomposition products seen via SPME analysis.

7.2

Probing THz-Driven Vibrations in RDX with Impulsive Stimulated Raman Scattering

As was described briefly in Section 3.4.4, sample constraints can make THz-pump/THz-probe measurements exceedingly difficult for certain materials if their absorption coefficients in the THz frequency range are sufficiently high compared to their THz indices. The high absorption requires an extremely thin sample in order to extract meaningful information from the THz probe pulse, which is potentially problematic if the sample is thin enough that etalon reflections of the THz probe pulse obscure the desired dynamics. In non-centrosymmetric media, the absence of an inversion center implies that Raman- and IR-active vibrational modes are not mutually exclusive. Therefore, a solution to this problem is to forgo THz probing and instead probe Raman-active modes using a visible wavelength, as many samples of interest that have a high THz absorption are relatively transparent in the visible

range. Even in centrosymmetric media, THz-induced changes in ISRS signals could occur through coupling among Raman-active and IR-active vibrational modes.

The broad bandwidth of femtosecond laser pulses precludes the use of spontaneous Raman probing, necessitating a coherent Raman probing method instead. The method used here is impulsive stimulated Raman scattering (ISRS), which was chosen on the basis of its relative simplicity of implementation when compared to other coherent Raman probes such as femtosecond stimulated Raman scattering. In ISRS, a pair of ultrafast pump pulses are overlapped and used to impulsively excite a collective vibrational mode at frequency ν_α within the sample, whose wavevector is given by

$$\mathbf{q} = \mathbf{k}_1 - \mathbf{k}_2 \tag{7.1}$$

where $\mathbf{k_1}$ and $\mathbf{k_2}$ are the wavevectors of the incident ultrashort pulses[9]. For impulsive excitation to occur, an oscillation period at the frequency ν_α must be sufficiently long in duration compared to the duration of the excitation pulse[9]. This gives the frequency limit for impulsive excitation as

$$\nu_\alpha < \frac{1}{\tau_L} \tag{7.2}$$

where τ_L is the excitation pulse duration. With a 100 fs laser pulse, as is typical for many ultrafast titanium:sapphire laser systems, this gives an upper limit of approximately 10 THz to the frequency of the impulsively excited vibration.

Probing of the impulsively excited vibration is typically accomplished with another time-delayed ultrashort pulse. When the probe pulse is overlapped with the impulsively excited vibrational mode, the intensity and frequency spectrum of the probe pulse oscillate at the frequency ν_α of the impulsively excited vibration[9]. Monitoring the intensity of a specific spectral component of the probe pulse as a

function of the pump/probe delay time yields a time-domain signal corresponding to the impulsively excited vibration. An example of the time- and frequency-domain signals, which were collected on neat CH_2I_2 liquid, appears in Fig 7.8.

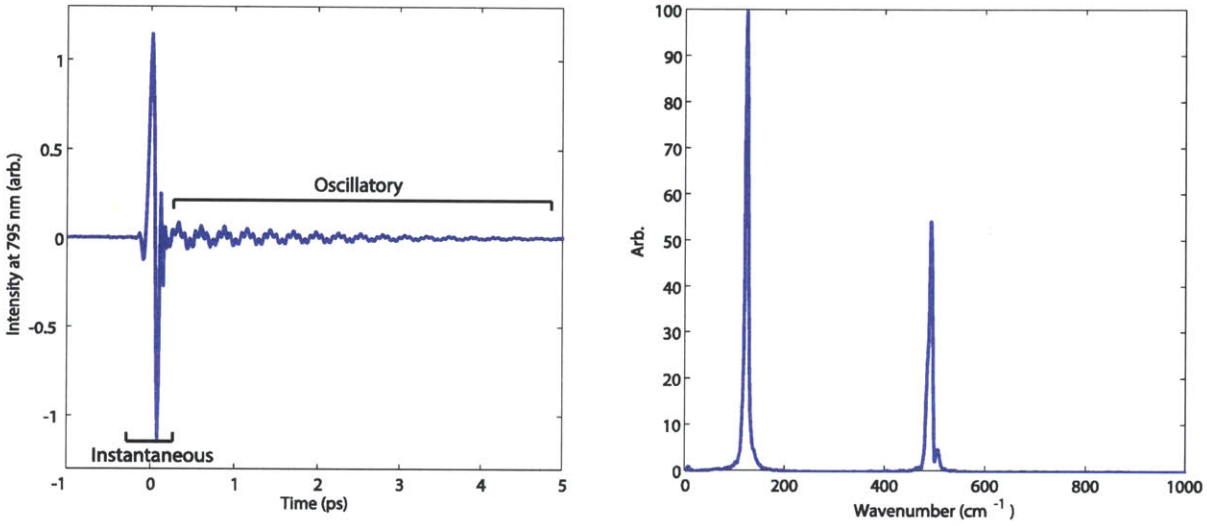

Figure 7.8. Time- (left) and frequency-domain (right) forward ISRS signals collected from CH_2I_2 liquid and detected at 795 nm using a titanium:sapphire ultrafast laser oscillator, which produced 46 fs pulses centered at 800 nm. The time-domain signal displays an instantaneous response, which corresponds to the nonresonant electronic response of the sample to the envelope of the excitation pulse, followed by an oscillatory "tail", which corresponds to the impulsively excited vibrational motions. The Fourier transform of the oscillatory tail produces the frequency spectrum at right. The oscillations at 122 and 490 cm^{-1} (3.67 and 14.7 THz, respectively) match literature values for the molecular vibrational frequencies.

For use as a probe of THz-driven vibrational dynamics, ISRS may be used in a simplified geometry known as "forward" ISRS[10–12]. In this geometry, a single ultrafast pulse interacts with the sample twice, as both $\mathbf{k_1}$ and $\mathbf{k_2}$. In this case, the impulsively excited vibrations have zero transverse wavevector component, but have a small forward wavevector component due to the red-shift of one of the interacting pump field components compared to the other (within the pulse spectral bandwidth). The coherent vibrations may be detected in the forward direction using a collinearly-propagating probe beam. This geometry was implemented in the collinear THz-pump/THz-probe spectrometer described in Chapter 3, as shown in Fig. 3.6. Detection of the frequency shift of the probe is accomplished using a

photodiode behind a 1 nm bandpass narrowband filter, for which the transmission wavelength has been chosen to correspond to a value near the half-maximum of the frequency spectrum of the pulse. This maximizes the amplitude of the change of the transmitted intensity as the probe frequency shifts alternately to the red and to the blue as a result of the coherent vibrations under way in the sample. The arrangement of the photodiode and narrowband filter was chosen to minimize the space required for detection.

RDX, discussed in the previous subsection, is one material for which the THz-pump/ISRS-probe technique is attractive due to sample limitations in the THz range. When oriented in the 210 plane, RDX exhibits an absorption at 0.8 THz that is extremely useful in tilted-pulse-front based THz-pump/THz-probe measurements owing to its very good overlap with the typical bandwidth obtained from a tilted-pulse-front source. However, the extremely high peak absorption coefficient associated with this mode (measured to be over 100 cm^{-1} even in isotropic powder form[13]) and relatively low THz refractive index (1.6 – 1.8[14]) cause the sorts of sample issues that make THz probing difficult.

ISRS spectra obtained for a single crystal of 210-cut RDX using the THz-pump/ISRS-probe spectrometer with the THz excitation pulse blocked appear in Fig. 7.9, and show spectral features at 20.8, 60.1, and 108 cm^{-1} (0.624, 1.80, and 3.24 THz, respectively), which show good agreement to published Raman spectra[15]. Comparison to published mode assignments[3,15] show that the modes correspond to lattice vibrations, with the highest frequency mode having some contribution from NO_2 rotations as well. ISRS spectra taken as a function of pump/probe delay (Fig. 7.10) show potential THz-driven amplitude changes, which may be suggestive of coupling between the THz pump pulse and the Raman-active modes probed by ISRS. Furthermore, the amplitudes of the 20.8 and 60.1 cm^{-1} modes decrease while the amplitude of the 108 cm^{-1} mode increases, which is in keeping with the upconversion theory of RDX decomposition. This is especially intriguing given the centrosymmetry of the RDX unit cell, which implies mutual exclusivity between the sets of Raman and IR-active vibrations. Unfortunately, the

low signal-to-noise ratio of the ISRS probe and its sensitivity to laser power fluctuations over the 12 to 24 hour time period necessary for scan collection means that repeated experiments with better signal-to-noise are necessary for conclusive data.

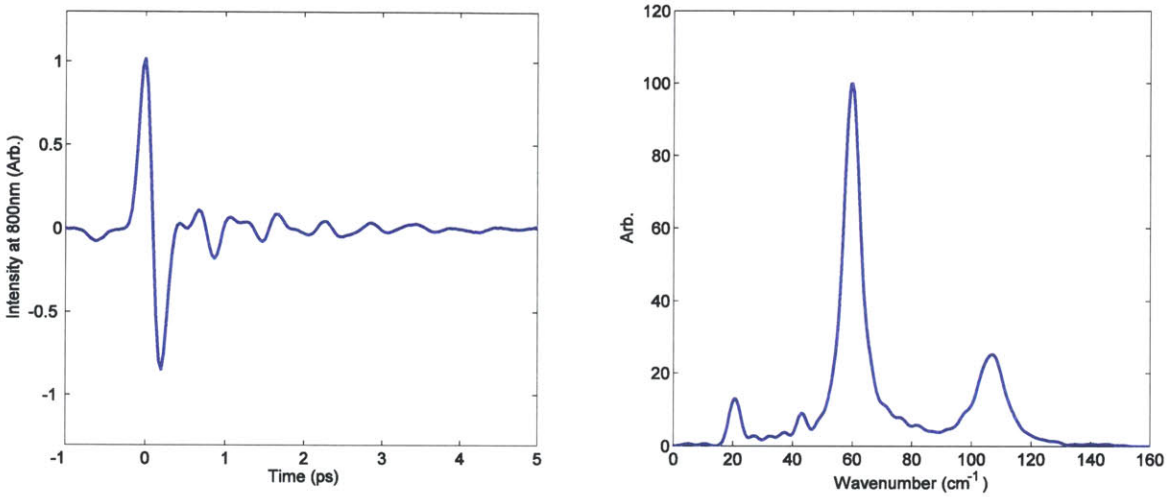

Figure 7.9. Time- (left) and frequency-domain (right) ISRS signals collected on single-crystal 210-cut RDX using the THz-pump/ISRS-probe spectrometer with the THz pump pulse blocked. In this case the coherent vibrations are excited solely by the ISRS excitation pulse.

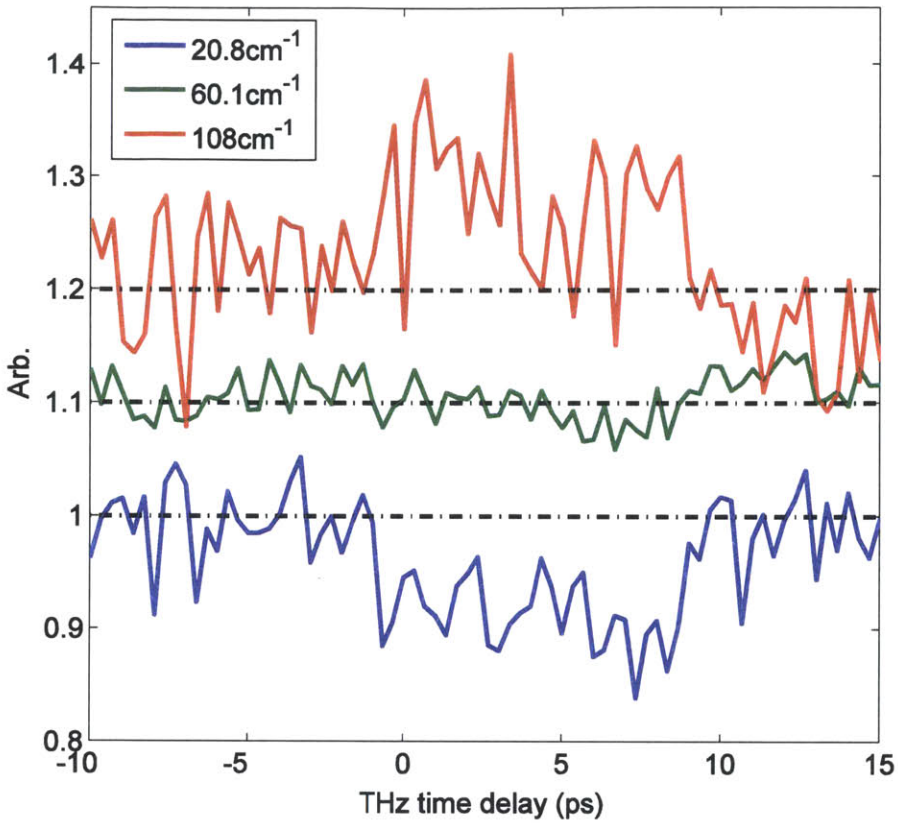

Figure 7.10. Amplitudes of 20.8, 60.1, and 108 cm^{-1} ISRS spectral features as a function of THz-pump/ISRS-probe delay, showing preliminary evidence of possible THz-driven amplitude modulations of the Raman modes probed by ISRS after the pump/probe overlap at t = 0, in which the amplitudes of the 20.8 and 60.1 cm^{-1} Raman-active modes decrease and the amplitude of the 108 cm^{-1} mode increases.

7.3

THz Quantum-Confined Stark Effect Measurements

In the quantum-confined Stark effect, the optical absorption spectrum of a quantum-confined system is modulated by an external electric field, leading to a shift of the absorption to lower frequencies[16]. This effect is well-studied in cadmium selenide (CdSe) quantum dots, which exhibit strong Stark effects due to their high polarizabilities[17]. Recently, we have demonstrated the quantum-confined Stark effect in CdSe quantum dots using a single-cycle THz pulse as the external electric field. A

saturated solution of CdSe quantum dots dissolved in toluene was introduced to the focus of the THz-pump/optical-probe spectrometer outlined in Section 3.4.2. Optical probing was carried out using a sapphire-based ultrafast white light source, part of which was resonant at and around the 611 nm absorption maximum of the CdSe quantum dots. The transmitted optical intensity at 625 nm was monitored as a function of pump/probe delay time, as it corresponds to the half-maximum of the low-frequency side of the 611 nm absorption peak and therefore is most sensitive to the expected Stark shift. Preliminary results (Fig. 7.11) show a transient modulation in the transmitted 625 nm intensity, which appears to follow the absolute value of the THz pump pulse, consistent with similar measurements[18]. Analysis of this result is ongoing, and further refinement of the experimental technique is necessary to yield a sufficient signal-to-noise ratio for quantitative measurements.

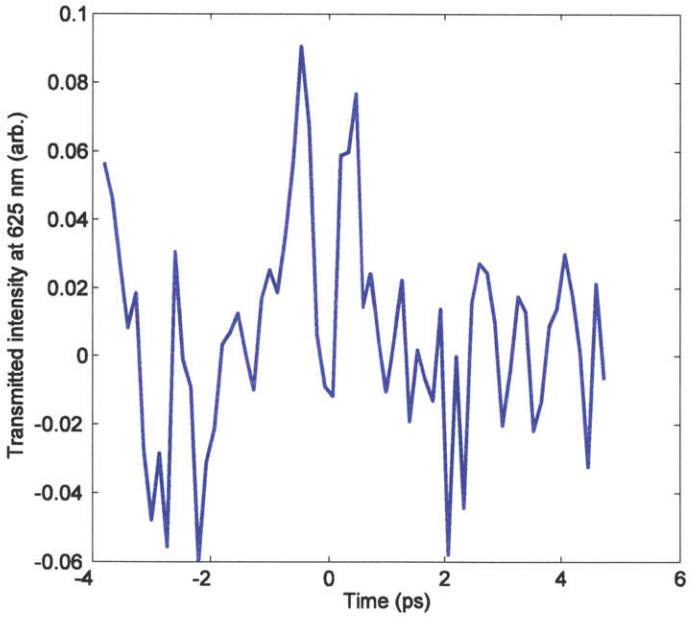

Figure 7.11. Preliminary THz-driven quantum-confined Stark effect in CdSe quantum dots. The feature centered at t = 0, which corresponds to the pump/probe overlap, is believed to follow the absolute value of the THz pump field.

7.4

Probing THz Interactions with Shocked Energetic Materials

As discussed in previous sections, the decomposition mechanism of RDX after the application of a mechanical shock is believed to be heavily dependent on THz-frequency doorway states. The shock-driven decomposition of RDX has also been the subject of time-resolved fluorescence investigations, in which the chemical species evolved during the RDX decomposition have been identified and monitored through their time-resolved fluorescence signatures following shock initiation through mechanical means[19]. We have recently begun investigations of the effects of high-field THz pulses on the shocked decomposition of RDX in an attempt to influence the decomposition process through interactions with the doorway states. This will be accomplished using a recently-developed laser-driven shock technique[20], around which a tilted-pulse-front based THz source can be implemented. Overlap of the THz pulses with the shocked sample is accomplished using the setup shown in Fig. 7.12.

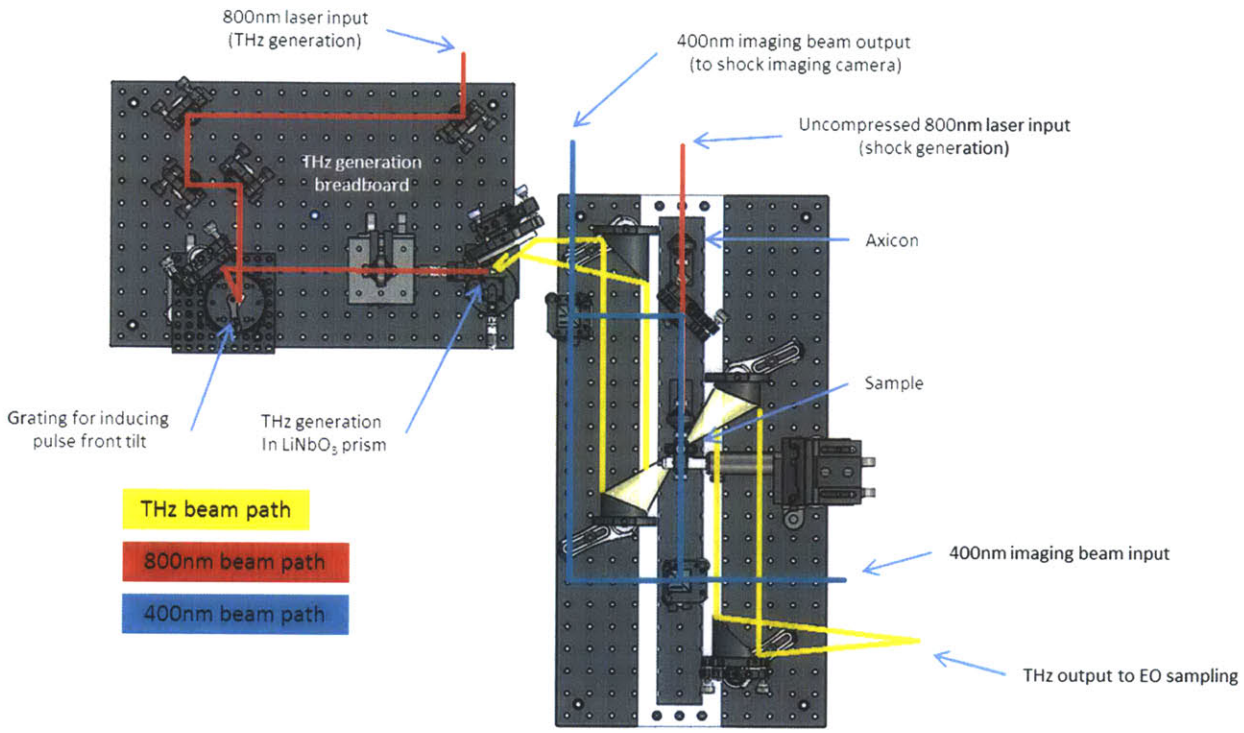

Figure 7.12. Spectrometer design incorporating laser-driven shock initiation and THz pulses. The shock initiation is accomplished using the 800 nm pulse, and is probed interferometrically using the 400 nm beam. Overlap of THz pulses (generated by a tilted-pulse-front source) is accomplished using an OAP configuration with two 90 degree and two 45 degree reflectors.

7.5

Conclusions

Nonlinear THz spectroscopy has promising applications in many problems in chemistry, physics, and materials science. Throughout this thesis, nonlinear THz responses have been demonstrated in a broad range of systems. In many cases, nonlinear responses were observed in systems previously lacking them, which was made possible by metamaterial enhancement of free-space fields. Furthermore, probing of THz-driven responses has been accomplished by a variety of methods previously used either sparingly or not at all in combination with THz pumping, including X-ray and Raman methods. Overall, therefore, the work presented in this thesis demonstrates the continued development of nonlinear THz spectroscopy away from its roots, in which it was painstakingly applied to carefully selected systems, towards its future as a commonplace technique, in which it can be applied to a broad range of systems and can be probed using an ever-increasing array of methods.

References

1. Dlott, D. D. & Fayer, M. D. Shocked molecular solids: Vibrational up pumping, defect hot spot formation, and the onset of chemistry. *J. Chem. Phys.* **92,** 3798 (1990).

2. Tokmakoff, A., Fayer, M. D. & Dlott, D. D. Chemical reaction initiation and hot-spot formation in shocked energetic molecular materials. *J. Phys. Chem.* **97,** 1901 (1993).

3. Boyd, S. G. & Boyd, K. J. A computational analysis of the interaction of lattice and intramolecular vibrational modes in crystalline alpha-RDX. *J. Chem. Phys.* **129,** 134502 (2008).

4. Barber, J. *et al.* Temperature-dependent far-infrared spectra of single crystals of high explosives using terahertz time-domain spectroscopy. *J. Phys. Chem. A* **109,** 3501 (2005).

5. Tao, H. *et al.* Performance enhancement of terahertz metamaterials on ultrathin substrates for sensing applications. *Appl. Phys. Lett.* **97,** 261909 (2010).

6. Vas, G. & Vékey, K. Solid-phase microextraction: a powerful sample preparation tool prior to mass spectrometric analysis. *J. Mass Spectrom.* **39,** 233 (2004).

7. Kirkbride, K. P., Klass, G. & Pigou, P. E. Application of solid-phase microextraction to the recovery of organic explosives. *J. Forensic Sci.* **43,** 76 (1998).

8. Oyumi, Y. & Brill, T. B. Thermal decomposition of energetic materials 3. A high-rate, in situ, FTIR study of the thermolysis of RDX and HMX with pressure and heating rate as variables. *Combust. Flame* **62,** 213 (1985).

9. Yan, Y.-X. & Nelson, K. A. Impulsive stimulated light scattering. I. General theory. *J. Chem. Phys.* **87,** 6240 (1987).

10. Yan, Y.-X., Gamble, E. B. & Nelson, K. A. Impulsive stimulated scattering: General importance in femtosecond laser pulse interactions with matter, and spectroscopic applications. *J. Chem. Phys.* **83,** 5391 (1985).

11. Ruhman, S., Joly, A. G. & Nelson, K. A. Time-resolved observations of coherent molecular vibrational motion and the general occurrence of impulsive stimulated scattering. *J. Chem. Phys.* **86,** 6563 (1987).

12. Ruhman, S., Joly, A. G. & Nelson, K. A. Coherent molecular vibrational motion observed in the time domain through impulsive stimulated Raman scattering. *IEEE J. Quantum Electron.* **24,** 460 (1988).

13. Chen, J., Chen, Y., Zhao, H., Bastiaans, G. J. & Zhang, X.-C. Absorption coefficients of selected explosives and related compounds in the range of 0.1-2.8 THz. *Opt. Express* **15,** 12060 (2007).

14. Hu, Y., Huang, P., Guo, L., Wang, X. & Zhang, C. Terahertz spectroscopic investigations of explosives. *Phys. Lett. A* **359,** 728 (2006).

15. Haycraft, J. J., Stevens, L. L. & Eckhardt, C. J. Single-crystal, polarized, Raman scattering study of the molecular and lattice vibrations for the energetic material cyclotrimethylene trinitramine. *J. Appl. Phys.* **100,** 053508 (2006).

16. Miller, D. A. B. *et al.* Band-edge electroabsorption in quatum well structures: the quantum confined Stark effect. *Phys. Rev. Lett.* **53,** 2173 (1984).

17. Empedocles, S. A. & Bawendi, M. G. Quantum-confined Stark effect in single CdSe nanocrystallite quantum dots. *Science* **278,** 2114 (1997).

18. Hoffmann, M. C., Monozon, B. S., Livshits, D., Rafailov, E. U. & Turchinovich, D. Terahertz electro-absorption effect enabling femtosecond all-optical switching in semiconductor quantum dots. *Appl. Phys. Lett.* **97,** 231108 (2010).

19. Patterson, J. E., Dreger, Z. A., Miao, M. & Gupta, Y. M. Shock wave induced decomposition of RDX: time-resolved spectroscopy. *J. Phys. Chem. A* **112,** 7374 (2008).

20. Pezeril, T. *et al.* Direct visualization of laser-driven focusing shock waves. *Phys. Rev. Lett.* **106,** 214503 (2011).